Nano Research

Open Access

Review Article

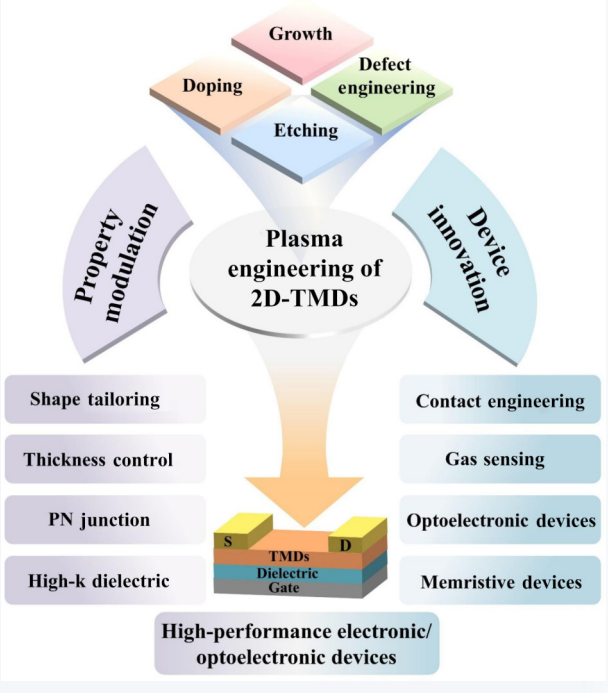
Plasma engineering of two-dimensional transition metal dichalcogenides: From material synthesis to functional device integration

Yuan Xie[1,2], Ai Zhang[1], Guangjun Wang[1], Shida Huo[2], Pingjuan Niu[1] ✉, and Enxiu Wu[2] ✉

[1] *School of Electronics and Information Engineering, Tiangong University, Tianjin 300387, China*
[2] *State Key Laboratory of Precision Measurement Technology and Instruments, School of Precision Instruments and Opto-electronics Engineering, Tianjin University, Tianjin 300072, China*

Cite this article: *Nano Research*, **2025**, *18*, 94907853. https://doi.org/10.26599/NR.2025.94907853

ABSTRACT: Two-dimensional transition metal dichalcogenides (TMDs) have shown great potential for application in the next generation of electronics and optoelectronics due to their atomically thin thickness, tunable band gap, and strong light-matter interaction. However, their practical application is still limited by challenges such as the constraints of high-temperature synthesis processes, compatibility issues of p-type/n-type doping strategies, and insufficient nanoscale patterning accuracy. Plasma treatment has become a key technology to break through these bottlenecks with its unique advantages such as low-temperature operation capability, generation of highly active reactive species and precise controllability of multiple parameters. This review comprehensively reviews the latest progress in plasma engineering of TMDs (MoS_2, WS_2, WSe_2, etc.) based on a systematic "fundamental process–property modulation–device innovation" framework. The key plasma technologies are highlighted: plasma-enhanced chemical vapor deposition (PECVD) for low-temperature growth, bidirectional doping achieved through active species regulation, atomic layer precision etching, and defect engineering. The regulation mechanism of plasma on the intrinsic properties of materials is systematically analyzed, including electronic structure modification, optical property optimization (such as photoluminescence enhancement) and structural feature evolution. It then reveals how plasma technology promotes device innovation: achieving customizable structures (p-n junctions, sub-10 nanometer channels), optimizing interface properties (reducing contact resistance, integrating high-k dielectrics), and significantly improving the performance of gas sensors, photodetectors and neuromorphic computing systems. Finally, this article looks forward to future research directions, emphasizing that plasma technology is a versatile and indispensable platform for promoting TMDs towards practical applications.



KEYWORDS: plasma engineering, two-dimensional (2D) transition metal dichalcogenides, doping and defect modulation, device integration

Received: June 19, 2025; **Revised:** July 25, 2025
Accepted: July 28, 2025

✉Address correspondence to Pingjuan Niu, niupingjuan@tiangong.edu.cn; Enxiu Wu, enxiuwu@tju.edu.cn

1 Introduction

Two-dimensional transition metal dichalcogenides (TMDs), such as MoS_2, WS_2, and WSe_2, have emerged as promising candidates in post-silicon electronics and optoelectronic devices due to their unique electronic structures, tunable bandgap properties, and

exceptional optoelectronic characteristics [1–4]. Compared to conventional bulk materials, TMDs exhibit distinct advantages, including atomic-scale thickness, high carrier mobility, and strong light-matter interactions, making them attractive for applications in transistors, photodetectors, gas sensors, and neuromorphic devices [5–8]. Nevertheless, the practical implementation of TMDs in high-performance devices faces critical challenges. Efficient and controllable synthesis of high-quality, large-area TMDs films is limited by slow growth rates or high temperatures (> 700 °C), hindering efficient and controllable production of high-quality, large-area films [9–11]. Additionally, the lack of stable, controllable, and complementary metal-oxide-semiconductor (CMOS)-compatible p-type/n-type doping strategies impedes precise regulation of carrier type and concentration [12–14]. Furthermore, the requirement for precise nanoscale patterning to fabricate complex device structures also remains another key bottleneck [15, 16].

Plasma treatment technology offers distinct advantages in addressing these challenges, especially its low-temperature operation, precise multi-parameter control, and generation of highly reactive species. These capabilities establish plasma as a comprehensive paradigm for the engineering of TMDs in an integrated process from material synthesis and performance tuning to functional device fabrication [17–19]. For instance, plasma-enhanced chemical vapor deposition (PECVD) leverages plasma-activated precursors to reduce reaction activation energies, enabling growth of TMDs at significantly lower temperatures (~ 150 °C) and providing a viable pathway for controllable synthesis of high-quality films [20, 21]. For property modulation, plasma demonstrates exceptional versatility. High-density reactive species (electrons, ions, radicals) generated in plasmas induce diverse controllable reactions with two-dimensional (2D) materials, including oxidation, reduction, and substitution [22–25]. Through precise adjustment of gas composition and power parameters, plasma achieves bidirectional doping within a single system [26]. Bidirectional doping refers to the controlled realization of both n-type and p-type doping in the same 2D material (e.g., MoS_2, WS_2) by tuning key parameters of plasma treatment, such as processing time and plasma power. A representative example shows that tuning the frequency of NH_3 plasma selectively induces either N-substitutional doping (p-type) or S-vacancy generation (n-type) in MoS_2, demonstrating the feasibility of *in situ* bidirectional doping in a unified plasma process [27].

In device fabrication, plasma etching serves as a critical enabler for precision patterning [28]. It provides atomic-scale accuracy in controlling TMDs dimensions and geometry. When integrated with electron-beam lithography, plasma etching facilitates the fabrication of sub-10-nm channels and complex device architectures (e.g., Hall bar devices, multi-terminal memristive crossbars [29]), meeting stringent requirements for advanced nanoelectronics.

Herein, this review systematically examines recent advances in plasma engineering of TMDs through a "fundamental processes–property modulation–device innovation" framework (Fig. 1). The review begins by detailing fundamental plasma treatment techniques adapted for TMDs, including plasma-assisted growth for synthesizing monolayer materials and vertical heterostructures, plasma doping strategies for polarity modulation via parameter control, plasma etching for atomic-layer-precision thinning, and plasma-enabled defect engineering (e.g., vacancy generation and passivation). It then explores how these methods modulate critical material properties, covering electronic structure modification, optical property tuning (e.g., photoluminescence (PL) enhancement), and structural evolution (characterized via morphology, lattice vibrations, and crystallinity). Subsequently, the review demonstrates device innovations enabled by plasma engineering, covering device structure customization (shape tailoring, thickness control, p-type doping, p-n junction formation), interface and contact optimization (surface cleaning, high-k dielectric integration, contact resistance reduction), and performance enhancement in applications such as gas sensors, optoelectronic devices, and neuromorphic computing. Finally, the review concludes with a summary and future perspectives, addressing challenges and opportunities in this rapidly developing field.

2 Plasma treatment techniques for TMDs

2.1 Plasma-assisted growth: From monolayers to core–shell structures

Plasma-assisted synthesis has emerged as a potent technique for the preparation of TMDs, offering unique advantages such as enhanced reactivity, reduced synthesis temperature, and direct growth of TMDs on flexible substrates [37–39]. This section explores the various plasma-assisted synthesis methods for TMDs, classifying the materials into single material, heterostructures, bulk materials, and core–shell structures. The role of plasma in facilitating these synthesis processes is also critically examined.

Single material. TMDs are widely used in field-effect transistors (FETs), photodetectors, and electrocatalysts due to their unique crystal structures and physical properties. PECVD and plasma-enhanced atomic layer deposition (PEALD) are commonly employed methods for synthesizing monolayer TMDs. Through these techniques, thin films of MoS_2, WS_2, and other TMDs with varying structures (monolayer, bilayer, and few-layer) [40, 41] and phases (1T and 2H) [39, 42] have been successfully fabricated on large scales [37, 43], including 4-inch wafers and 6-inch wafers.

In the synthesis process, precursor molecules are dissociated by high-energy electrons in the plasma, which leads to the formation of reactive radicals and ions. These reactive species subsequently interact with the substrate surface to form TMDs thin films. For instance, in PECVD-based WS_2 synthesis, S serves as the precursor, and plasma breaks down sulfur-containing gases like H_2S into sulfur atoms. These sulfur atoms then react with transition metal atoms, such as those from metal oxides, to form WS_2, as shown in Fig. 2(a). Plasma not only promotes the decomposition of precursors and the formation of TMDs but also lowers the synthesis temperature by enhancing the reactivity of the system.

Heterostructures. Another key application of plasma-assisted synthesis is the creation of heterostructures, which are composed of different TMDs or other two-dimensional materials. These heterostructures are highly desirable for combining the unique properties of each material. Plasma-assisted synthesis techniques enable the direct growth of heterostructures on a single substrate, facilitating the integration of different materials. The active species within plasma can penetrate the interface between different layers, promoting chemical bonding and ensuring a robust structure. Furthermore, plasma treatment offers precise control over the interlayer distance in these heterostructures, a crucial factor that influences their electrical and optical properties.

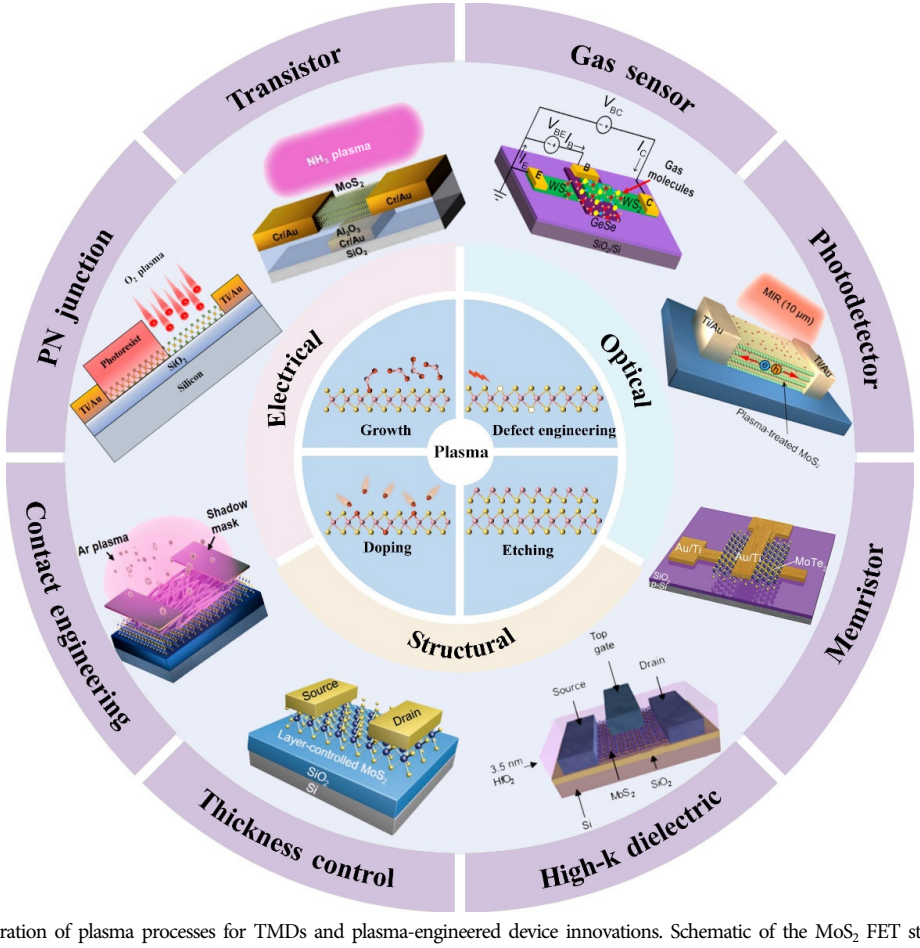


Figure 1 Schematic illustration of plasma processes for TMDs and plasma-engineered device innovations. Schematic of the MoS_2 FET structure with NH_3 plasma treatment. Reproduced with permission from Ref. [26], © American Chemical Society 2024. Schematic diagram of the MoS_2 horizontal homogeneous PN junction. Reproduced with permission from Ref. [30], © American Chemical Society 2022. Schematic of 2H-$MoTe_2$ FETs with t-Te NW contacts. Reproduced with permission from Ref. [31], © Elsevier B.V. 2021. A schematic image of layer-controlled MoS_2 device. Reproduced with permission from Ref. [32], © WILEY-VCH Verlag GmbH & Co. KGaA, Weinheim 2020. Integration of scaled PEALD HfO_2 as gate dielectric in top-gated MoS_2 FET. Reproduced with permission from Ref. [33], © American Chemical Society 2017. Schematic of the $MoTe_2$ device with the structure of Au/Ti/$MoTe_2$/Au/Ti. Reproduced with permission from Ref. [34], © The Royal Society of Chemistry 2022. Schematic of the photodetector structure based on plasma-treated MoS_2. Reproduced with permission from Ref. [35], © American Chemical Society 2023. Schematic of gas detection with the common-emitter configuration with different gas molecules. Reproduced with permission from Ref. [36], © American Chemical Society 2020.

For example, a single-step penetrative plasma sulfurization method, reported by Seok, uses PECVD to synthesize WS_2/MoS_2 vertical heterostructures [43], as depicted in Fig. 2(b). In this process, plasma accelerates the sulfurization by facilitating the movement of H_2S and ionized H_2S+ towards the Mo-W layers. The plasma sheath containing ionized gases and H_2S radicals significantly reduces the synthesis temperature, allowing for growth at temperatures lower than those required for traditional thermal CVD (650–920 °C). Additionally, the ionized H_2S+ species can penetrate various thicknesses of the Mo-W seed layers, forming heterostructures with varying thicknesses. This method presents a promising approach for the large-scale production of wafer-level 2D heterostructures. Trivedi et al. synthesised lateral heterostructures by a selective epitaxial atom replacement (SEAR) process using plasma at room temperature (RT) [44], as depicted in Fig. 2(c). In this process, inductively coupled hydrogen plasma (ICP) generates highly reactive hydrogen radicals that create selenium vacancies, while concurrently supplying low-energy sulfur radicals that selectively replace Se atoms, resulting in lateral WSSe and MoSSe heterojunctions. This low-temperature method not only enables atomic-level control but also avoids degradation or alloying typically associated with high-temperature techniques, offering a new route for the controlled fabrication of complex lateral TMDs heterostructures.

Core–shell structures. Furthermore, plasma-assisted synthesis methods are increasingly being explored for the fabrication of core–shell structures, which are composed of a core material coated with a shell of different materials. These structures have garnered significant attention, particularly for energy applications such as solar cells and photocatalytic hydrogen evolution [45, 46]. Plasma-assisted sulfurization is a promising technique for synthesizing core–shell TMDs nanostructure films. For instance, a plasma-assisted sulfurization method has been used to synthesize WO_3/WS_2 core–shell nanostructures, where tungsten oxide (WO_3) serves as the core material, and H_2S plasma is used as the sulfur source [47], as shown in Fig. 2(d). The plasma dissociates H_2S into sulfur and hydrogen radicals, which then react with the WO_3 core to form the WS_2 shell. The thickness of the shell can be precisely controlled by manipulating the active species in the plasma. Compared to bare WO_3 or WS_2 materials, the resulting core–shell

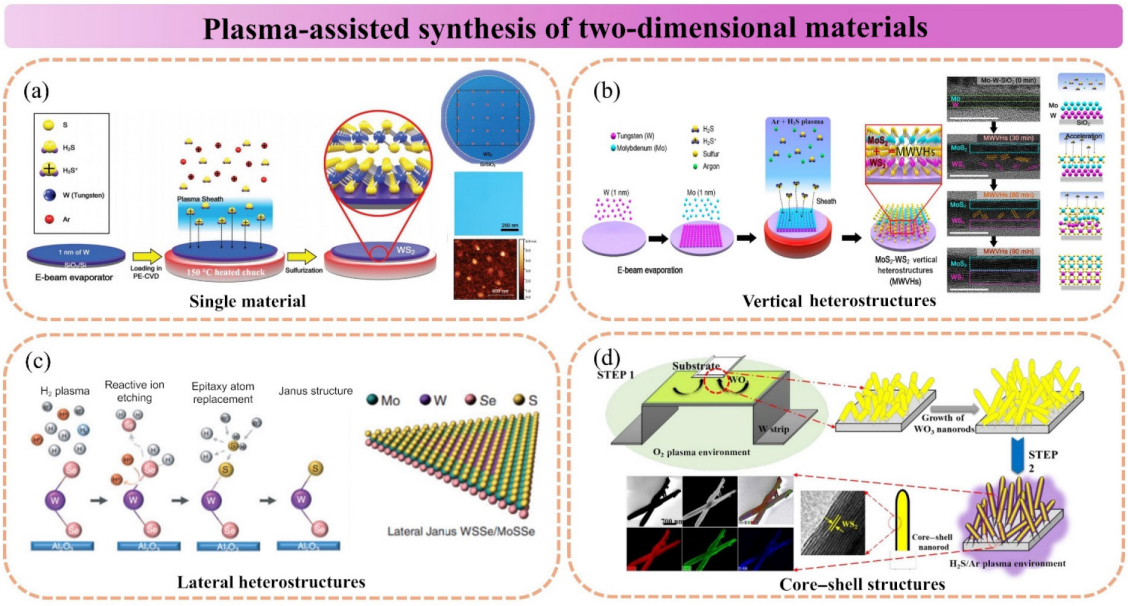


Figure 2 Plasma-assisted growth of TMDs. (a) Illustration of monolayer 1T-WS_2 synthesis sequence using PECVD at 150 °C. Reproduced with permission from Ref. [48], © WILEY-VCH Verlag GmbH & Co. KGaA, Weinheim 2020. (b) Schematic of the synthesis of MoS_2-WS_2 vertical heterostructures (MWVHs) via single-step penetrative sulfurization by PECVD. Reproduced with permission from Ref. [43], © American Chemical Society 2021. (c) Schematic synthesis of lateral Janus WSSe/MoSSe heterostructures by SEAR. Reproduced with permission from Ref. [44], © Wiley-VCH GmbH 2020. (d) The synthesis of WO_3/WS_2 core–shell nanorods (NRs) using plasma assisted sublimation followed by sulfurization process. Reproduced with permission from Ref. [47], © American Chemical Society 2019.

structure demonstrates significantly enhanced electrocatalytic performance in hydrogen evolution reactions (HER).

While chemical/physical vapor deposition (CVD/PVD) enables growth of high-quality TMDs, their inherent requirement for elevated temperatures (> 700 °C) imposes critical limitations, particularly detrimental to temperature-sensitive substrates like polyimide. PECVD fundamentally overcomes this constraint by utilizing energetic plasma species to activate precursor molecules, thereby significantly reducing reaction activation energies. This mechanism facilitates rapid, low-temperature growth while maintaining exceptional material quality and uniformity across wafer-scale dimensions. In the PECVD growth mechanism, radio frequency (RF) excitation is used to ionize an inert carrier gas (e.g., Ar), generating energetic ions (Ar^+) and reactive free radicals. These species collide with precursor gases (e.g., H_2S), promoting dissociation into active species such as S radicals. Under an applied electric field, these radicals directionally bombard pre-deposited transition metal films (e.g., Mo, W), inducing surface reactions that form TMDs compounds (e.g., MoS_2) directly on the substrate [49]. This plasma-assisted chemical reaction pathway allows synthesis at low temperatures (typically ≤ 300 °C), replacing traditional high-temperature pyrolysis (> 700 °C) and enabling integration with flexible or heat-sensitive substrates.

Several studies have synthesised individual WS_2 and MoS_2 films at the wafer level by PECVD using metals or metal oxides and H_2S gas as precursor materials. As shown in Fig. 3(a), Kim et al. prepared WS_2/graphene heterostructures of uniform mass and sufficient size (4 inches) by direct deposition of WS_2 on flexible polyimide substrates via PECVD [50] and used as flexible electrodes to enable highly selective, stable, and reproducible testing of dopamine and serotonin. Bala et al. achieved low-temperature growth of large-area molybdenum disulphide films on a common microscope glass substrate (area ≈ 27 cm^2) using plasma-enhanced chemical vapour deposition (Fig. 3(b)) [51]. On this basis, 7 × 7 arrays of top sector-controlled transparent thin film transistors (TFTs) were fabricated, which exhibited a uniform response in visible light with a maximum responsivity of 27 $A{\cdot}W^{-1}$, a high detectivity of 3.5 × 10^8 $cm{\cdot}\sqrt{Hz}{\cdot}W^{-1}$ and a sensitivity of 364. Seok et al. utilised PECVD by modulating the substrate temperature to generate a metallic 1T phase at 150 °C and a semiconducting 2H phase at 300 °C, prepared 1T/1T-MoS_2/WS_2 and 2H/2H-MoS_2/WS_2 vertical heterostructures for the first time on 4-inch SiO_2/Si wafers, as shown in Fig. 3(c) [52]. Among them, 1T/1T-MWH exhibits optimal hydrogen precipitation performance (overpotential 0.294 V, Tafel slope 99 $mV{\cdot}dec^{-1}$) due to the high intrinsic activity of the metallic 1T phase, the synergistic effect of the heterogeneous interfacial alloying structure, and the plasma-induced exposure of edge-active sites at the nanocrystalline boundary.

In addition, to address the challenge of preparing large-area, layer-count-controlled 2D films, Youn et al. achieved high-quality 2D MoS_2 films with large-area, high-uniformity, and layer-count-controllable 2D films on a 6-inch SiO_2/Si substrate by isolated plasma soft deposition (IPSD) coupled with a sulfide post-processing (Fig. 3(d)) [37]. The IPSD is able to effectively overcome the plasma damage and uniformity problems of conventional sputtering methods for the preparation of 2D materials. The respiration sensors fabricated from the simultaneously prepared three-layer MoS_2 films showed ultra-fast response (≈ 2 s) and high sensitivity.

2.2 Plasma doping: Parameter-controlled polarity modulation

P-type doping is essential for two-dimensional material-based devices, as CMOS technology fundamentally relies on the integration of p-type and n-type transistors to construct logic gates and integrated circuits [53–55]. However, most 2D semiconductors (e.g., MoS_2, WS_2, $MoSe_2$) exhibit intrinsic n-type conductivity,

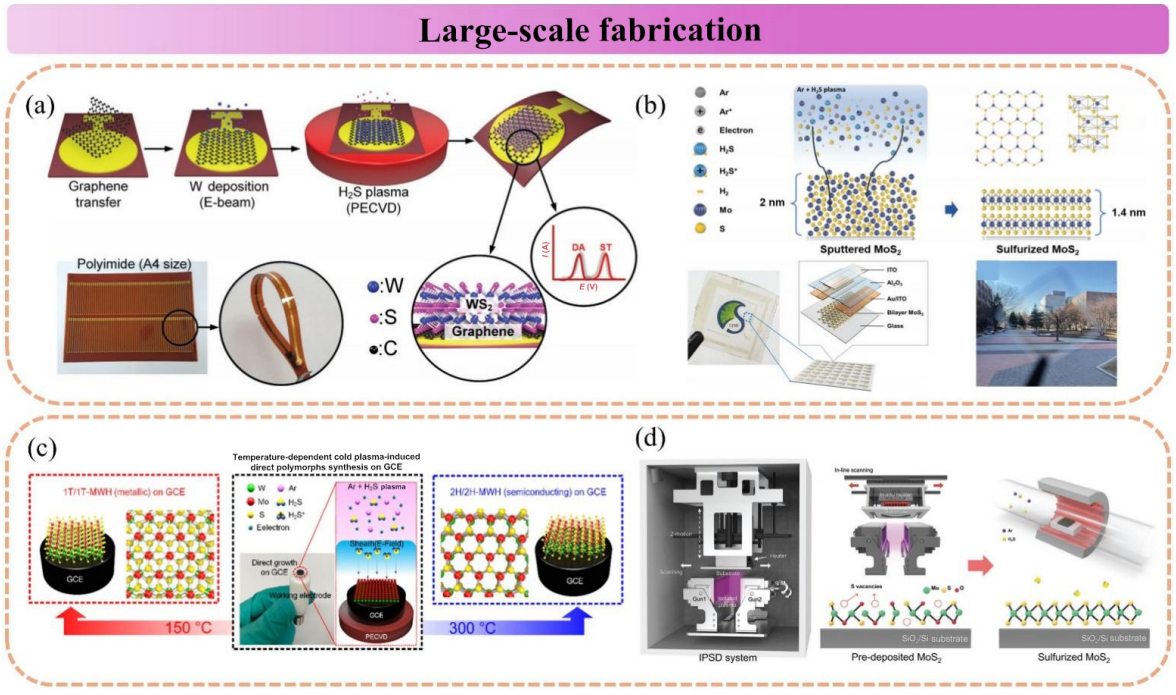


Figure 3 Large-scale fabrication. (a) Schematic of the fabrication process for the WS_2/graphene heterostructure. Reproduced with permission from Ref. [50], © Wiley-VCH GmbH 2021. (b) Growth and device architecture of transparent MoS_2 TFTs on glass. Reproduced with permission from Ref. [51], © Wiley-VCH GmbH 2022. (c) Schematic diagrams of 1T/1T-MoS_2/WS_2 and 2H/2H-MoS_2/WS_2 vertical heterostructures. Reproduced with permission from Ref. [52], © American Chemical Society 2023. (d) Schematic of the IPSD system and the two-step synthesis process and the crystal structure of the 2D MoS_2 layer on a SiO_2/Si substrate. Reproduced with permission from Ref. [37], © Wiley-VCH GmbH 2024.

primarily attributed to strong electron doping induced by interfacial charge impurities and contributions from inherent structural defects [56–58]. Furthermore, p-type conduction in 2D semiconductors is significantly constrained by Fermi-level pinning at metal/semiconductor interfaces, which imposes high Schottky barriers for efficient hole injection [59].

Recently, plasma doping has emerged as a rapidly advancing technique, distinguished by these advantages: high doping efficiency, process simplification, and excellent compatibility with established semiconductor manufacturing [60–62]. By precisely regulating gas composition, discharge parameters, and plasma modes, this approach can selectively activate multiple reaction mechanisms, including oxidation, reduction, and deposition, enabling precision in controlling carrier type and concentration in 2D materials. Critically, this plasma-based methodology circumvents dielectric breakdown limitations inherent to conventional approaches and thereby achieves degenerate doping levels, providing an innovative solution for optimizing the electrical performance of 2D material-based devices. Plasma treatment conditions for doping in TMDs are summarized in Table 1.

Traditional ion implantation is a technique that introduces impurity ions into semiconductor materials to alter their conductivity type [63]. For P-type doping, acceptor impurity ions (such as B, Al, and Ga) are typically implanted, which replace the original atoms in the semiconductor and create holes, thereby enhancing P-type conductivity. For N-type doping, donor impurity ions (such as P, N, and S) are implanted, which replace the original atoms and release free electrons, thereby enhancing N-type conductivity. These doping mechanisms also apply to two-dimensional materials, but particular attention must be given to the control of parameters to avoid damaging the lattice structure and surface morphology of the two-dimensional materials [64], which could lead to performance degradation. In the case of TMDs, exposure to oxygen-containing plasmas can lead to oxidation of the TMDs surface, forming high-work-function tungsten oxide (WO_x)/molybdenum oxide (MoO_x) layers or oxygen-containing chemical bonds [19, 55, 65, 66]. These structures facilitate hole injection, enabling P-type doping (Figs. 4(a) and 4(b)). For N-type doping, it is typically achieved by creating chalcogen (e.g., S or Se) vacancies that act as donor sites (Figs. 4(c) and 4(d)) [67–69].

In the early stages of research, plasma doping typically only achieved a single doping type, either P-type or N-type doping [75]. However, with further research, it was found that the doping effect of plasma is not fixed, but highly dependent on its control parameters, including gas composition, pressure, temperature, and exposure time. Based on this profound understanding, in 2021, Tan et al. made a breakthrough. By adjusting the radio frequency and exposure time of NH_3 plasma, they successfully revealed two doping mechanisms: one dominated by direct substitution of N atoms for original elements and the other by S vacancies (i.e., sulfur atom deficiencies) [27], as depicted in Fig. 4(e). This discovery not only significantly enriched the theoretical framework of plasma doping but also made it possible to achieve P-type and N-type bidirectional doping in two-dimensional materials such as MoS_2, thereby breaking the limitation of single-type doping. Subsequently, in 2024, Kang et al. further investigated the bidirectional doping effect of NH_3 plasma on MoS_2 and achieved precise control of doping types by accurately regulating the treatment time of NH_3 plasma [26]. Specifically, they successfully induced controllable N-type doping with sulfur vacancies (V_S) and P-type doping with nitrogen substitution in MoS_2, as depicted in Fig. 4(f). This achievement not only demonstrated the tremendous potential of NH_3 plasma in the doping of two-dimensional materials but also

Table 1 Summary of plasma treatment conditions for doping in TMDs

Doping type	Material	Plasma	Layer no.	Power (W)	Pressure	Temperature (°C)	Flow (sccm)	Time	Contacts	Refs.
n	WSe_2	H_2	1-6	5	140 mTorr	25	100	5 s	Ni	[68]
n	WSe_2	Ar	—	10	2×10^{-2} Torr	250	30	5–20 s	Pt/Ti	[69]
n	WSe_2	SF_6	20	80	20 mTorr	—	15	3 s	Nb	[70]
n	BP	BF_3	25	100	1×10^{-2} Torr	25	—	30 s	Ti/Au	[71]
n	WS_2	N_2	> 8	—	—	25	—	10 min	Ti/Au	[72]
n	MoS_2	CF_4	12–15	18	1×10^{-6} Torr	25	50	5 s	Ni/Au	[73]
n	MoS_2	N_2	6–9	180	15 Pa	25	—	2 h	—	[74]
n	MoS_2	O_2/Ar	15	10	1×10^{-7} Torr	—	30/30	10/30 s	Cr/Au	[67]
p	WSe_2	O_2/Ar	4	11	20 mTorr	25	100/20	2 min	Ag	[19]
p	WSe_2	O_2	8	50	30 mTorr	25	30	200 s	Pd	[76]
p	WSe_2	O_2	1–3	150	100 mTorr	150	60	5–60 s	Cr/Au	[77]
p	WSe_2	O_2	54	20	680 mTorr	—	50	60-480 s	Ti/Pt	[65]
p	MoS_2	O_2	6	10	90 mTorr	25	60	30 s	Ti/Au	[78]
p	MoS_2	O_2	1	50	100–200 mTorr	—	100	180 s	Cr/Au	[79]
p	MoS_2	Ar	3–6	48	—	25	10 and 50	10 s	Pd/Au	[80]
p	$MoSe_2$	O_2	1–6	50	550 mTorr	150	150	15 s	Pd/Au	[55]
p	PtS_2	O_2	9–10	30	39–43 Pa	550	—	10–60 s	Au	[81]
n and p	MoS_2	NH_3	4–5	10/20	10 Pa	25	10	60–120 s	Ni/Au	[27]
n and p	MoS_2	NH_3	3	10	0.4 Torr	150	30	0–50 s	Cr/Au	[26]

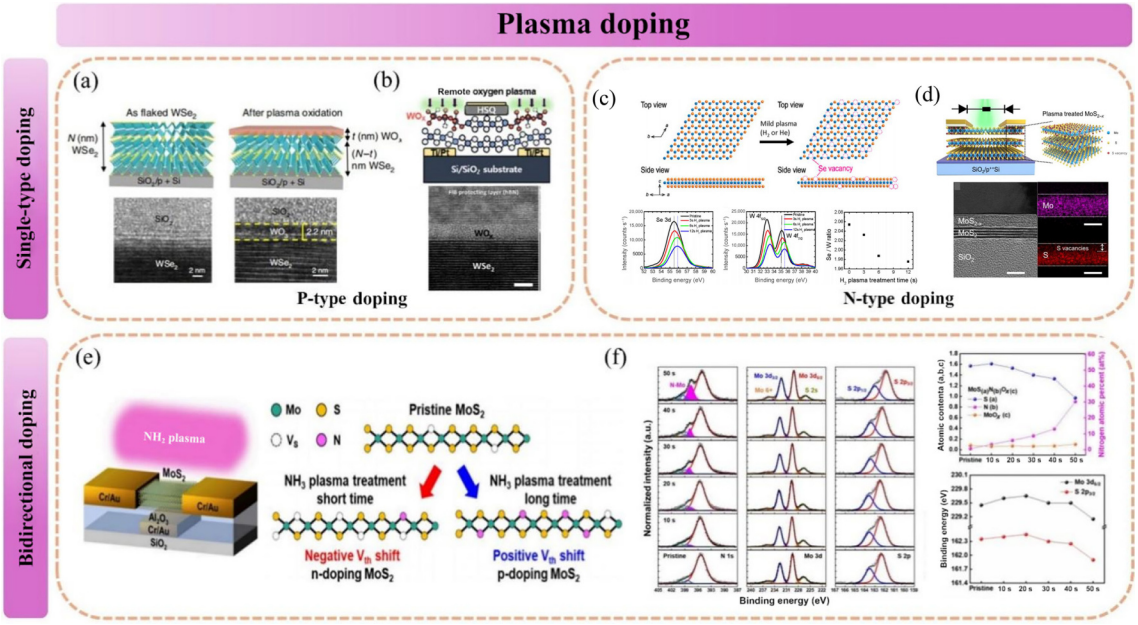


Figure 4 Plasma doping for TMDs. (a) Schematic of surface plasma oxidation and the corresponding cross-sectional transmission electron microscope (TEM) images of oxidized WSe_2. Reproduced with permission from Ref. [19], © Sivan, M. et al. 2019. (b) Schematic and TEM image of WSe_2 after plasma oxidation. Reproduced with permission from Ref. [65], © American Chemical Society 2023. (c) N-type doping of the WSe_2 flake after the H_2 plasma treatment. Reproduced with permission from Ref. [68], © American Chemical Society 2016. (d) N-type doping of MoS_2 through creating S vacancies using plasma. Reproduced with permission from Ref. [67], © Li, T. X. et al. 2023. (e) Schematic of bidirectional doping of NH_3 plasma treatment for the MoS_2 FET. (f) Nitrogen doping of MoS_2 with increasing NH_3 plasma treatment duration. Reproduced with permission from Ref. [26], © American Chemical Society 2024.

provided new perspectives and approaches for understanding and optimizing doping mechanisms in 2D materials.

From early single-type doping to current bidirectional doping, plasma doping technology has made significant progress, provided more flexible and diverse means for modifying the performance of two-dimensional materials.

2.3 Plasma etching: Atomic-level thinning

Plasma etching, an advanced material processing technique, has demonstrated significant potential in the preparation and fabrication of 2D materials. This technique utilizes the interactions between ions, electrons, and excited neutral particles with the

material surface in achieving atomic-level high-precision material thinning [31, 82, 83]. The subsequent part will elaborate on these three key aspects: the generation mechanism of plasma source, the etching mechanism, and the etching directionality.

In terms of plasma source generation mechanisms, commonly used etching technologies include ICP etching [84–86], reactive ion etching (RIE) [87–89], and PECVD [90, 91]. ICP etching generates high-temperature plasma through high-frequency inductive currents, ionizing and heating the gases to produce a stable plasma state (Fig. 5(a)). This technique is characterized by high etching rates, selectivity, and anisotropy, rendering it especially effective for the fabrication of 2D material structures with high aspect ratios. RIE, a widely employed dry etching technique, effectively removes material by selectively etching the material surface, enabling precise material removal. As illustrated in Fig. 5(b), during the etching process, gases are introduced into the reaction chamber and subjected to a radiofrequency electric field, which ionizes and excites the gases, forming a plasma. PECVD, a vacuum-based process, utilizes plasma energy to induce deposition reactions without requiring high substrate temperatures. As shown in Fig. 5(c), a high-voltage electric field is applied in the reaction chamber, exciting the reactant gases into a plasma consisting of highly reactive excited molecules, atoms, ions, and radicals.

Etching can be classified into physical etching, chemical etching, or a combination of physical and chemical processes. Physical etching involves the bombardment of two-dimensional materials with ions possessing high kinetic energy (such as Ar^+), causing the detachment of surface atoms without any chemical reactions occurring. In contrast, chemical etching is based on the chemical reactions between active particles in the plasma (common plasmas include SF_6, CF_4, O_2 etc.) and the two-dimensional material, generating volatile substances that are subsequently removed from the material surface, thereby completing the etching process. Lin et al. proposed an innovative plasma-based atomic layer etching (ALET) technique for precise layer-by-layer removal of MoS_2 [92]. This technique achieves accurate control over the number of MoS_2 layers through two cyclic physical processes. As illustrated in Fig. 5(d), first, Cl radicals adsorb onto the surface, weakening the Mo–S bonds; then, an Ar^+ ion beam bombards the MoS_2, breaking the weakened Mo–S bonds and causing physical desorption of the top layer. Complete etching of a monolayer MoS_2 can only be achieved when these two steps are carried out sequentially. Raman spectroscopy, X-ray photoelectron spectroscopy (XPS), and atomic force microscopy (AFM) confirm that each ALET cycle successfully removes one MoS_2 layer, achieving precise control over the number of layers without causing damage or leaving etching residues on the

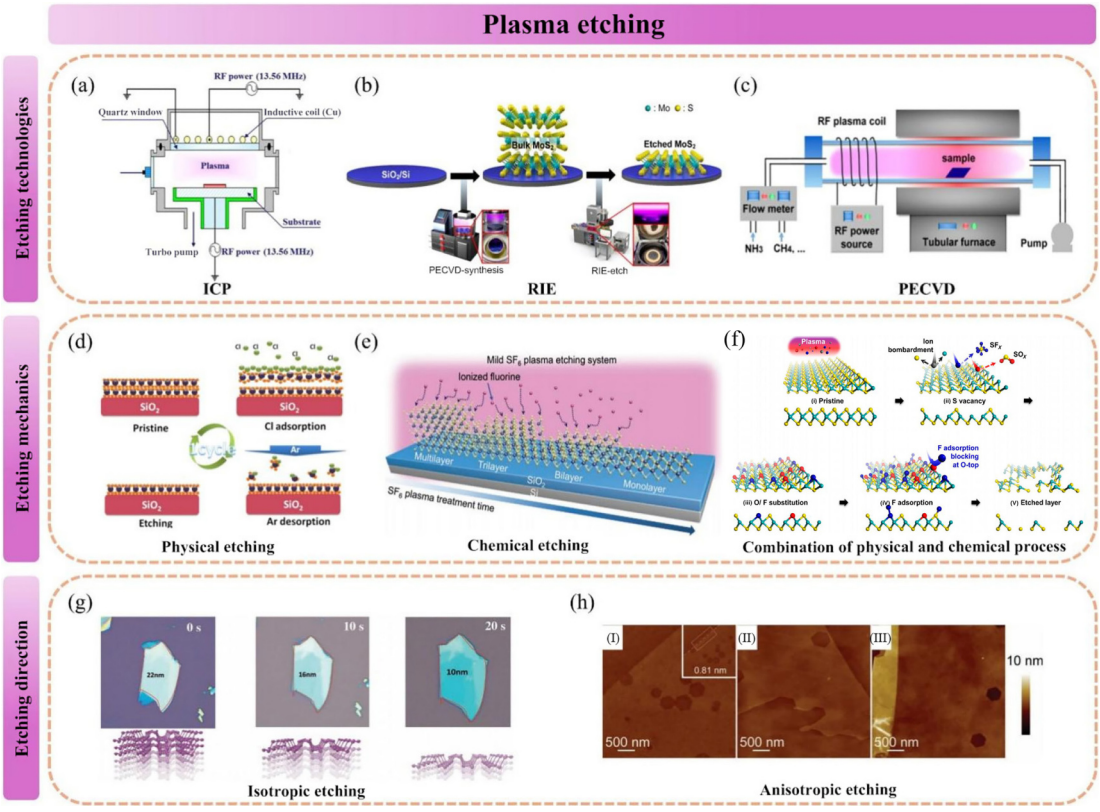


Figure 5 Plasma etching for TMDs. (a) Schematic illustrations of the RIE system. Reproduced with permission from Ref. [85], © Elsevier Ltd. 2012. (b) Schematic diagram of ICP system. Reproduced with permission from Ref. [88], © American Chemical Society 2023. (c) Schematic illustrations of the PECVD system. Reproduced with permission from Ref. [90] © American Chemical Society 2015. (d) Schematic drawing of MoS_2 ALET cycle for the lay-by-layer physical etching. Reproduced with permission from Ref. [92], © American Chemical Society 2015. (e) A schematic illustration of layer-by-layer chemical etching of multilayer MoS_2 film. Ionized fluorine is only chemically reacted without directly physical damage to MoS_2 film. Reproduced with permission from Ref. [32], © WILEY-VCH Verlag GmbH & Co. KGaA, Weinheim 2020. (f) Schematics of combination of physical and chemical process for MoS_2 etching using $Ar+CF_4+O_2$ plasma. Reproduced with permission from Ref. [88], © American Chemical Society 2023. (g) Optical images of the as-exfoliated BP flake, after 10 s CHF_3/O_2 plasma treatment and after 20 s CHF_3/O_2 plasma treatment, respectively. Reproduced with permission from Ref. [87], © WILEY-VCH Verlag GmbH & Co. KGaA, Weinheim 2018. (h) Hydrogen plasma etched single-layer (I), two-layer (II) and multi-layer (III) graphene, regular hexagonal holes are clearly formed at the defects. Reproduced with permission from Ref. [84], © WILEY-VCH Verlag GmbH & Co. KGaA, Weinheim 2010.

exposed surface. Chee et al. developed a mild sulfur hexafluoride (SF_6) plasma treatment for layer-by-layer etching of MoS_2 films [32]. This low-damage, layer-by-layer etching is attributed to the mild plasma etching system, which induces chemical reactions between ionized fluorine and MoS_2 without causing physical damage to the material. As shown in Fig. 5(e), by increasing the plasma treatment time, they successfully reduced the number of layers from three to a monolayer while maintaining the overall quality of the film. Kim et al. used mixed Ar+CF_4+O_2 plasma to achieve ultra-high precision and purity etching of MoS_2 at the wafer level. The mixed Ar+CF_4+O_2 plasma simultaneously induces physical and chemical reactions, as shown in Fig. 5(f). These reactions include Ar^+ ions physically bombarding the substrate, indiscriminately displacing substrate atoms; followed by F/O radicals, which decompose the Mo–S bonds, producing volatile products such as SF_x and SO_x and leaving sulfur vacancies; and Ar^+ ions removing substituted and adsorbed impurities. Therefore, the Ar+CF_4+O_2 mixed plasma can etch MoS_2 layers with atomic precision while suppressing chemical contamination.

For two-dimensional materials such as graphene and TMDs, isotropic etching refers to the process in which the etching rate is independent of the material's lattice direction or structure, and the etching proceeds at the same rate in all directions [93]. The realization of isotropic etching relies on specific physical and chemical processes. During the etching process, the plasma reacts with the material surface to form soluble or volatile compounds, which are subsequently removed or vaporized, resulting in material removal [94–96]. Since the etching agent reacts with the wafer surface in the same manner across all directions, the etching rate remains consistent in all directions. As shown in Fig. 5(g), with increasing plasma exposure time, optical microscope images clearly indicate a reduction in the thickness of black phosphorus (BP) across the entire sheet. Currently reported plasma-based processes for layer-by-layer thinning and patterning of two-dimensional materials are all isotropic etching processes [97–100]. Anisotropic etching refers to the phenomenon where the etching rates differ in different directions during the etching process. This difference is typically due to microstructural variations on or within the material surface, such as lattice orientation and defect distribution [101–104]. Yang et al. successfully achieved controllable anisotropic etching of graphene for the first time using a self-made remote inductively coupled plasma system [84]. Typical AFM images of monolayer, bilayer, and multilayer graphene on SiO_2 substrates after etching are shown in Fig. 5(h). The etching process is attributed to the hydrogenation and volatilization of carbon atoms. On the graphene basal plane, hydrogen radicals (H-radicals) attack carbon atoms at the edges and surface defects by forming C–H covalent bonds (hydrogenation) and breaking C–C bonds (volatilization), leading to the formation of hexagonal pits with jagged edges on graphene. The anisotropy of the etching arises from the fact that C–C bond breakage is directly influenced by the local bonding configuration.

2.4 Defect engineering: Vacancy creation and passivation

Plasma treatment, through the excitation of electrons and ions, bombards the surface of two-dimensional materials, creating localized high-energy regions that can induce defects or introduce functional groups. Figure 6(a) schematically illustrates a categorization of defects. These defects, including point defects (vacancies, substitutional atoms, interstitial atoms), line defects (dislocations), and plane defects (interface defects, stacking faults), play a crucial role in modulating the electronic structure, enhancing catalytic activity, and improving photoelectric properties of the 2D materials [79, 105–108]. This section explores the influence of plasma treatment on defect formation in two-dimensional materials and how these defects affect material performance.

Vacancies are among the most common types of defects in 2D materials. When plasma interacts with 2D materials, it primarily generates point defects such as sulfur vacancies and selenium vacancies. For instance, in MoS_2, various defects can be observed, including single V_S, double sulfur vacancies (V_{S2}), a vacancy involving one molybdenum and three sulfur atoms (V_{MoS3}), a vacancy involving one molybdenum and six sulfur atoms (V_{MoS6}), and complex defects such as two sulfur atoms occupying molybdenum positions (S_{2Mo}) and V_{S2} occupied by molybdenum [109]. Figure 6(b) depicts various potential defects in 2D MoS_2 that might be produced by plasma treatment. These defects not only exist in the topmost layer but can also penetrate several layers below the surface through plasma treatment. Jo et al. [110] demonstrated that plasma-induced selenium vacancies could penetrate up to 7 nm into $PtSe_2$ thin films, with the Se/Pt atomic ratio increasing linearly with depth.

Moreover, by precisely controlling the plasma process parameters (e.g., treatment duration, power, gas type), defects can be intentionally introduced, allowing for precise control over defect types. However, this requires a thorough understanding of the underlying thermodynamic and kinetic processes. Liu et al. [111] formed three defect types in WS_2 by varying the exposure time to oxygen plasma: single sulfur vacancies (V_S), oxygen substitution for single sulfur (O_S), and oxygen substitution for double sulfur (O_{2S}). Lee et al. [112] found that, in the early stages of plasma treatment, only the top-layer sulfur atoms were removed, while the vacancy and molybdenum atomic layers remained intact. As processing continued, hexagonal nanocracks formed along the zigzag edges due to strain relaxation induced by the defects. Furthermore, by optimizing plasma treatment parameters, defect repair can be achieved, thereby enhancing material performance. Li et al. [113] utilized O_2 plasma and determined an optimal power range that effectively repaired structural defects in MoS_2, reducing scattering centers and improving the electrical performance of MoS_2 FETs. The transfer characteristic curves after plasma treatment with different powers are shown in Fig. 6(c).

Plasma treatment enables the modulation of defect types and concentrations in 2D materials, significantly improving properties such as photoluminescence, catalysis, and hydrogen evolution. For example, Fu et al. [22] employed argon plasma to treat monolayer WS_2, significantly modifying defect types, particularly increasing the density of V_S and tungsten-based defects (including tungsten vacancies (V_W), tungsten-substituted sulfur anti-site defects (W_S), and tungsten stacking defects (W_2)), as illustrated in Fig. 6(d). These defects served as luminescent centers, leading to a more than tenfold increase in photoluminescence quantum yield (PL QY) and full width at half maximum (FWHM). Compared to untreated samples, the PL QY and electroluminescence external quantum efficiency (EL EQE) of plasma-treated monolayer WS_2 increased by 20 and 25 times, respectively, as shown in Figs. 6(e) and 6(f).

However, plasma parameters have a significant impact on performance [114, 115]. Zhang et al. [25] reported that plasma treatment increased sulfur vacancies, enhancing the adsorption of N_2 and lowering the energy barriers, thereby facilitating the

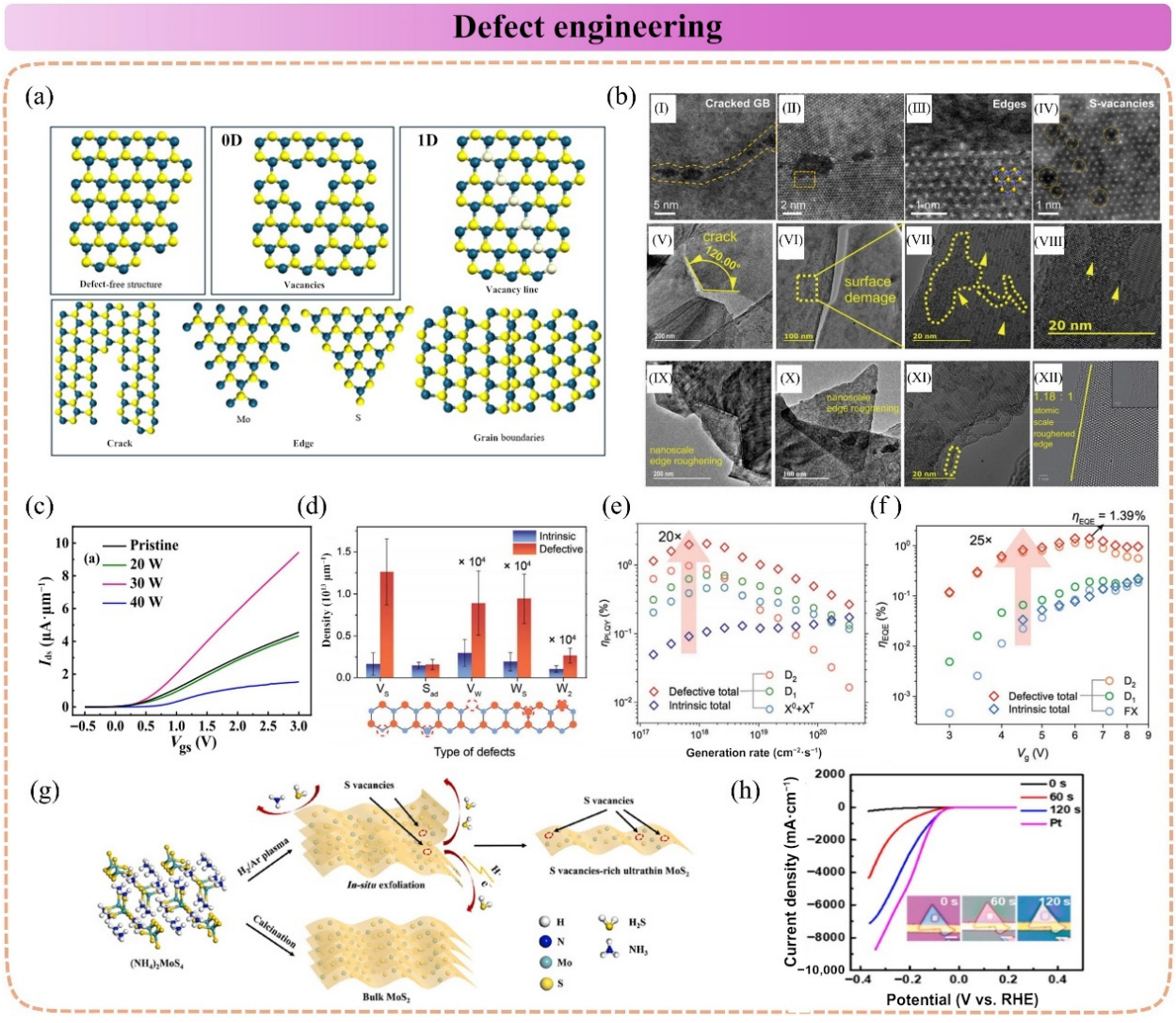


Figure 6 Defect engineering of TMDs. (a) Schematic views of different defects in 2D TMDs. (b) Various possible defects in plasma-treated TMDs layers.(I–IV Cracked grain boundary, edge sites, and S-vacancies. Reproduced with permission from Ref. [118], © American Chemical Society 2019. (V)–(VIII) Micro cracks and basal surface damages at different magnifications. (IX)–(XII) Roughened edges at nanoscale and atomic scale. Reproduced with permission from Ref. [119], © Elsevier Ltd 2019. (c) Transfer characteristics of MoS_2 in linear scale and with V_{ds} = 0.2 V. Reproduced with permission from Ref. [113], © IEEE 2021. (d) Defect density statistics of intrinsic (blue) and defective (red) monolayer WS_2 derived from five large area HAADF-STEM images in five individual samples. (e) PL QY of the intrinsic and defective monolayer WS_2 supported by h-BN in ambient conditions. (f) EL EQEs η_{EQE} of the vdWLED based on defective and intrinsic monolayer WS_2 as a function of V_g, in which η_{EQE} of the defective sample reaches a maximum of ≈ 1.39%. Reproduced with permission from Ref. [22], © Wiley-VCH GmbH 2024. (g) Brief mechanism diagram of precursor being reduced to MoS_2. Reproduced with permission from Ref. [25], © Elsevier Ltd. 2023. (h) HER polarization curves for the basal plane of ~ 20L $PtSe_2$ flake treated with Ar plasma at 15 W for varied durations and a Pt thin film measured with the electrochemical microcell setup. Reproduced with permission from Ref. [116], © American Chemical Society 2021.

nitrogen reduction reaction (NRR). The mechanism for the decomposition of the precursor by plasma is illustrated in Fig. 6(g). However, Ping et al. [116] found that increasing plasma power to 15 W introduced more Pt^0 to the $PtSe_2$ surface, prolonged treatment time, reduced the material conductivity, thus affecting hydrogen evolution performance, as shown in Fig. 6(h). The mechanisms of plasma treatment on 2D materials extend beyond the formation of defects such as vacancies, also encompassing synergistic effects of surface reconstruction, compositional transformation, or local phase changes. Park et al. [117] successfully introduced surface corrugation and heterogeneous nanodomains on WS_2 through plasma treatment, which also promoted the formation of oxides and sulfur vacancies. These combined effects enhanced the HER performance of WS_2, demonstrating the great potential of plasma technology in the modification of two-dimensional materials.

3 Tunable material properties via plasma engineering

3.1 Modulation of electronic properties

The wide application of plasma treatment in TMDs is not only reflected in the precise control of its doping and defects, but more importantly, it can ultimately achieve deep regulation of the electronic structure of the material, especially in the two core aspects of work function change and band structure reconstruction. These changes directly affect the Fermi level position, carrier concentration, conductivity type and inter-band migration

mechanism, and become the fundamental path to achieve device performance optimization.

One of the most straightforward manifestations of plasma-induced electronic modulation is the change in work function, closely associated with the position of the Fermi level. Kim et al. demonstrated that ICP treatment with chlorine radicals could reduce the work function of MoS_2 from 4.6 eV to below 4.3 eV [120], as measured by Kelvin probe force microscopy (KPFM) shown in Fig. 7(a). This shift reflects an upward movement of the Fermi level towards the conduction band minimum (CBM) due to electron injection from Cl dopants, resulting in enhanced n-type conductivity. Similar Fermi level shifts have been reported through NH_3 plasma treatment of MoS_2, enabling n^+-type doping, and O_2 plasma treatment of WSe_2, inducing p^+-type behavior via the formation of WO_x surface species and acceptor-like states near the valence band maximum (VBM) [121]. These observations suggest that plasma-assisted work function tuning offers a reliable route for carrier type and density engineering.

Plasma treatment also induces profound modifications to the band structure of 2D materials, beyond simple carrier injection [122]. In many cases, localized defects or substitutional atoms introduced by plasma exposure create new electronic states, narrow the bandgap, or even drive semiconductor-to-metal transitions. For instance, Kim et al. showed that plasma-induced Se vacancies (V_{Se}) in WSe_2 introduced defect states near the CBM, which evolved into a continuous defect band as the vacancy concentration increased [69]. This transformation shifted the material from intrinsic ambipolar behavior to n-type dominance. Similarly, Liu et al. found that nitrogen substitution in MoS_2 reduced the bandgap from 1.61 to 1.56 eV and introduced shallow acceptor states, facilitating p-type conduction [123]. The results of density functional theory (DFT) calculations for pristine and nitrogen doped monolayer MoS_2 are shown in Fig. 7(b). In $PtSe_2$, increasing Se vacancy concentration via Ar plasma narrowed the bandgap and induced mid-gap states, leading to a gradual transition toward metallic behavior [124]. More strikingly, plasma treatments can trigger electronic phase transitions. He et al. reported that Te vacancies induced by Ar plasma in $MoTe_2$ reduced the energy barrier for the semiconductor-to-metal transition between the 2H and 1T′ phases [34]. DFT calculations revealed that a vacancy concentration above 4% stabilized the metallic 1T′ phase, and lowered the local transition barrier to 0.15 eV, as illustrated in Figs. 7(c) and 7(d). This demonstrates the unique capability of plasma techniques to drive reversible structural and electronic phase changes, which are challenging to achieve via thermal or chemical means.

The modulation of trap states is also critical for tailoring the charge recombination dynamics and long-term stability of 2D materials. Liu et al. investigated how various oxygen-related defects introduced by O_2 plasma affect the electronic properties of monolayer WS_2 [111]. DFT simulations indicated that V_S and double oxygen substitution (O_{2S}) introduced deep-level traps within the bandgap, which can serve as non-radiative recombination centers. In contrast, single oxygen substitution (O_S) did not create additional in-gap states and preserved a band structure similar to that of pristine WS_2. The energy band structure diagrams of pristine and different defect types of WS_2 monolayers are shown in Fig. 7(e). This suggests that under appropriate conditions, plasma treatment can passivate detrimental defects, effectively "cleaning" the band structure and suppressing undesired carrier recombination pathways.

3.2 Tuning optical properties: Photoluminescence and beyond

Plasma treatment significantly modifies the optical properties of TMDs, including shifts in absorption spectra, enhancement or suppression of PL, and adjustment of optical bandgaps [125, 126].

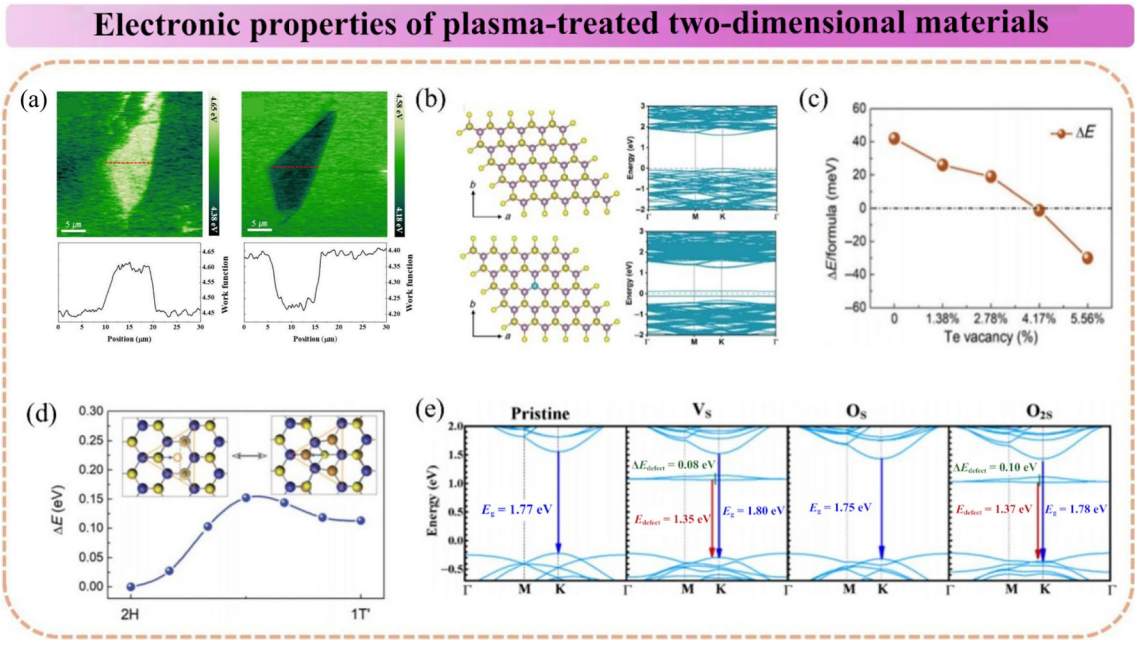


Figure 7 Modulation of electronic properties of TMDs. (a) Work function modulation of MoS_2 via Cl-based plasma treatment. Reproduced with permission from Ref. [120], © The Royal Society of Chemistry 2019. (b) Band structure evolution of MoS_2 under nitrogen doping. Reproduced with permission from Ref. [123], © Liu, X. Y. et al. 2024. (c) Stability of 1T' phase in $MoTe_2$ under increasing Te vacancy concentration. (d) Energy distribution of the phase transition in a localised region with Te vacancies. Reproduced with permission from Ref. [34], © The Royal Society of Chemistry 2022. (e) Electronic effects of oxygen-related defects in WS_2. Reproduced with permission from Ref. [111], © American Chemical Society 2022.

These changes are primarily attributed to plasma-induced defects, such as vacancies, substitutional impurities, or adsorbates [127, 128]. These defects act as centers for light absorption or emission, thereby influencing the optical responses of TMDs. They may alter the intensity of existing emission peaks or even result in the appearance of new emission peaks [129, 130]. For instance, Dhall et al. observed that oxygen plasma treatment induced a transition from an indirect bandgap to a direct bandgap, weakened interlayer coupling, and imparted highly circularly polarized photoluminescence properties in multilayer MoS_2 [131, 132]. Specifically, plasma treatment partially filled or intercalated into the interlayer gaps of MoS_2, increasing the interlayer distance and reducing van der Waals (vdW) coupling (Fig. 8(a)). After plasma treatment, the PL intensity of multilayer MoS_2 increased by 16 times, and the spectral linewidth significantly narrowed by approximately 46%. The PL peak shifted from 1.81–1.83 to 1.86 eV, confirming the transition to a direct bandgap (Figs. 8(b) and 8(c)). Under circularly polarized light excitation, the plasma-treated MoS_2 demonstrated a circular polarization degree as high as 80%, indicating a high spin polarization of optically excited carriers (Fig. 8(d)).

Moreover, the energy and exposure time of plasma are crucial factors affecting the optical properties of TMDs. Liu et al. successfully induced three different types of defects—V_S, oxygen substitutions (O_{1S} and O_{2S})—by controlling the plasma exposure time [111]. As the plasma exposure time increased, the carrier lifetime exhibited a trend of first decreasing, then increasing, and finally decreasing again. This variation was related to an increase in the probability of non-radiative recombination caused by defects. More importantly, plasma treatment may further influence the light absorption and luminescent processes of TMDs by altering their band structures (e.g., inducing layer decoupling or introducing new energy levels) and the dynamics of electron-hole pairs (e.g., generation, recombination, and migration) [133, 134]. As shown in Fig. 8(e), sulfur vacancies captured excitons, providing an additional non-radiative relaxation channel, causing the exciton population to decrease significantly faster in defective samples than in pristine samples and leading to reductions in exciton lifetime and diffusion coefficient (Figs. 8(f) and 8(g)) [105]. The exciton diffusion length of defective samples decreased sharply from 349.44 to 107.40 nm, a reduction of more than three times (Fig. 8(h)).

3.3 Structural characterization: Morphology, phase, and crystallinity

Plasma treatment significantly alters the structural characteristics of 2D TMDs, and these effects can be thoroughly investigated using various characterization techniques, including optical microscopy (OM), AFM, Raman spectroscopy, transmission electron microscopy (TEM), and XPS [135]. These tools enable the evaluation of changes in surface morphology, lattice structure, crystallinity, and defect states, all of which directly impact the electronic and optoelectronic performance of TMD-based devices [112, 136, 137]. Plasma etching or exposure often results in notable surface morphological changes [70, 138]. For example, TEM imaging can reveal differences in roughness, flake thickness, and topographic uniformity before and after plasma treatment (Fig. 9(a)). The extent and nature of these morphological changes depend strongly on the plasma parameters, such as power, duration, and gas composition. Low-power plasma typically induces mild surface oxidation or roughening, while high-power plasma may lead to more aggressive material removal and structural disordering due to physical bombardment [98, 139]. Importantly, different TMDs exhibit varying degrees of resistance to plasma-induced damage. For instance, under oxygen plasma treatment, WSe_2 nanosheets demonstrate superior stability compared to MoS_2 (Fig. 9(b)). This is attributed to the formation of a protective WO_3 surface layer, which has a higher melting point

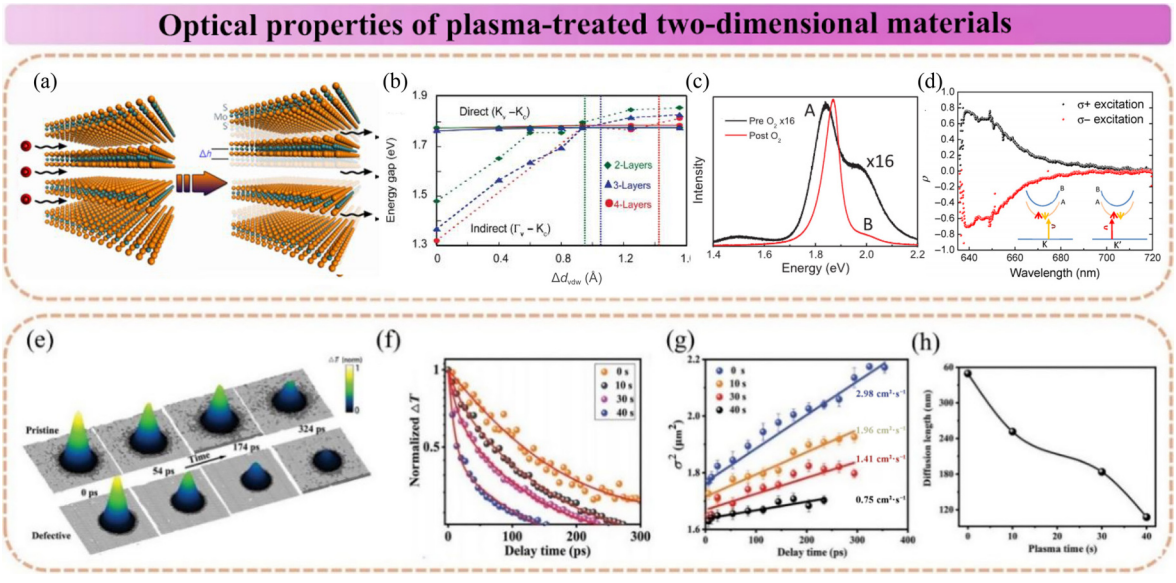


Figure 8 Tuning optical properties of TMDs. (a) Atom structure diagram of few-layer MoS_2 after remote oxygen plasma. (b) Direct gap (solid) and indirect gap (dotted) energy transitions for 2L, 3L, and 4L MoS_2 for a range of increases in the vdW gap. (c) PL spectra before and after oxygen plasma treatment. Reproduced with permission from Ref. [132], © WILEY-VCH Verlag GmbH & Co. KGaA, Weinheim 2015. (d) The degree of polarization ρ of MoS_2 flakes (3-4 layers) after oxygen plasma treatment collected at 30 K. Reproduced with permission from Ref. [131], © American Chemical Society 2016. (e) Surface plots of 2D TAM images of pristine and defective few-layer WS_2 at different delay times. (f) Transient absorption traces with different plasma treatment times for few-layer WS_2. (g) The time evolution of the variances of Gaussian profiles for the different plasma treatment times. (h) Exciton diffusion length of few-layer WS_2 with different plasma treatment times. Reproduced with permission from Ref. [105], © WILEY-VCH Verlag GmbH & Co. KGaA, Weinheim 2019.

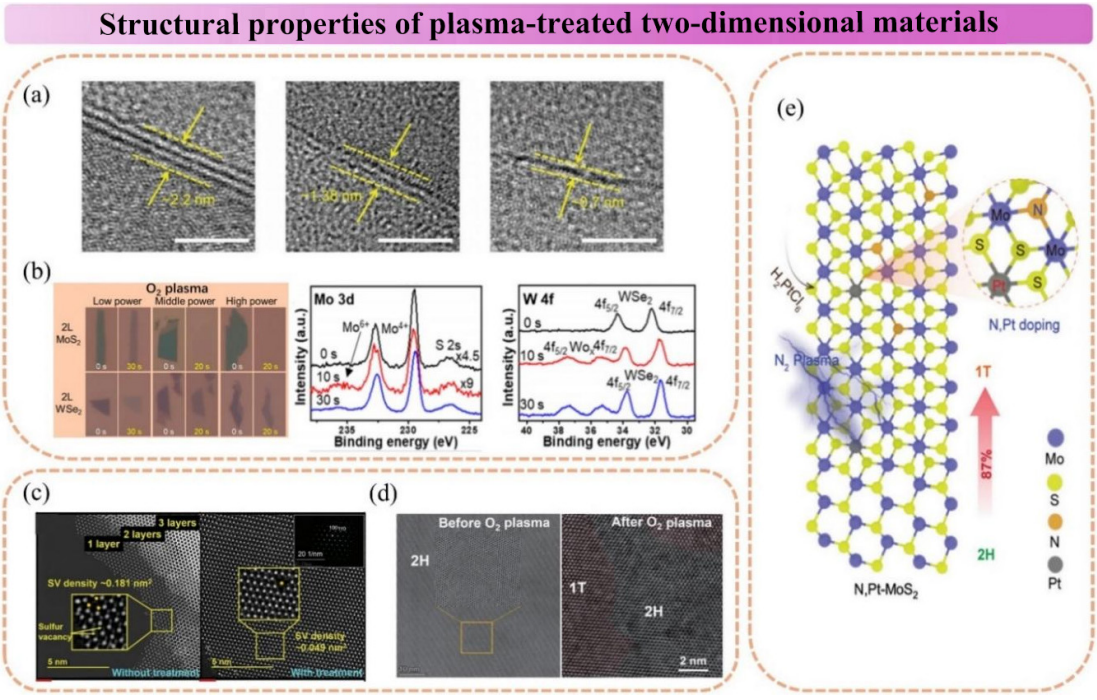


Figure 9 Structural characterization of plasma-treated TMDs. (a) TEM images of folded MoS_2 layers with 30, 40, 50 s plasma treatment time. Reproduced with permission from Ref. [32], © WILEY-VCH Verlag GmbH & Co. KGaA, Weinheim 2020. (b) Oxidation and etching behaviors of MoS_2 and WSe_2 treated by oxygen plasma with different excitation powers; XPS spectra of MoS_2 and WSe_2 treated by low power oxygen plasma for 0, 10, and 30 s. Reproduced with permission from Ref. [140], © American Chemical Society 2020. (c) The atomic structures of WS_2 before and after nitrogen plasma treatment obtained through STEM. Reproduced with permission from Ref. [72], © WILEY-VCH Verlag GmbH & Co. KGaA, Weinheim 2019. (d) HR-TEM images of WSe_2 before and after O_2 plasma treatment. Reproduced with permission from Ref. [14], © Tsinghua University Press 2023. (e) Structural illustration of N,Pt-MoS_2 nanosheets. Reproduced with permission from Ref. [61], © The Royal Society of Chemistry 2022.

and enhanced resistance to reactive species, thereby mitigating structural degradation and preserving the underlying lattice [140].

Beyond surface morphology, plasma treatment also influences the internal lattice structure [141, 142]. In some cases, plasma exposure facilitates defect passivation or rearrangement. Oxygen plasma has been reported to heal sulfur vacancies in MoS_2, thereby improving electron mobility and restoring structural integrity. Similarly, nitrogen plasma treatment can introduce N atoms into WS_2, effectively reducing sulfur vacancy concentration and enhancing the overall crystal quality and carrier transport properties (Fig. 9(c)) [72].

Extended plasma exposure or higher energy input, however, may generate excessive vacancies and lead to lattice distortion. These defects can trigger phase transitions within the TMDs. For example, plasma-induced sulfur vacancies in MoS_2 can promote a transition from the semiconducting 2H phase to the metallic 1T phase, altering the material's conductivity type and enabling new functionalities [60, 143]. Likewise, in WSe_2, oxygen ions may replace Se atoms, leading to local bond rearrangement and initiating a 2H-to-1T phase transition (Fig. 9(d)) [14]. Furthermore, the incorporation of transition metal dopants such as Pt into MoS_2 can significantly enhance the formation of the 1T phase, with conversion efficiencies reported up to 87% (Fig. 9(e)) [142].

4 Plasma-engineered device innovations

4.1 Device structure customization and realization

As 2D materials transition from fundamental research to practical nanoelectronic applications, the ability to precisely engineer their device-level structure and doping profile becomes increasingly critical [144]. In particular, the physical dimensions (e.g., geometry, thickness, and edge morphology) and electronic characteristics (e.g., conductivity type and junction architecture) of 2D materials must be tailored to meet the performance and integration requirements of modern logic and optoelectronic devices. Plasma-based processing technologies have emerged as highly versatile and scalable tools to address these challenges. Through controllable etching and oxidation reactions, plasma techniques enable high-resolution shaping and layer-by-layer thickness adjustment of 2D materials, offering critical advantages for short-channel transistor scaling and thickness-sensitive device design. Furthermore, plasma doping provides a robust pathway for achieving p-type conductivity and constructing functional p-n junctions, overcoming a key limitation of TMDs in complementary circuit applications. The following part detail recent advances in plasma-enabled structural engineering of 2D devices.

4.1.1 Shape tailoring and thickness control

Plasma etching technology offers a powerful and flexible tool for tailoring the geometry, edge morphology, and thickness of TMDs, making it particularly valuable for the fabrication of devices with stringent structural requirements. When integrated with lithographic techniques, plasma etching enables customized shaping of 2D materials with high spatial resolution [54, 145–147], as shown in Figs. 10(a)–10(d). This combination allows precise control over both lateral and vertical dimensions, providing critical support for short-channel device engineering. Notably, hydrogen plasma has been employed to etch graphene/BN heterostructures,

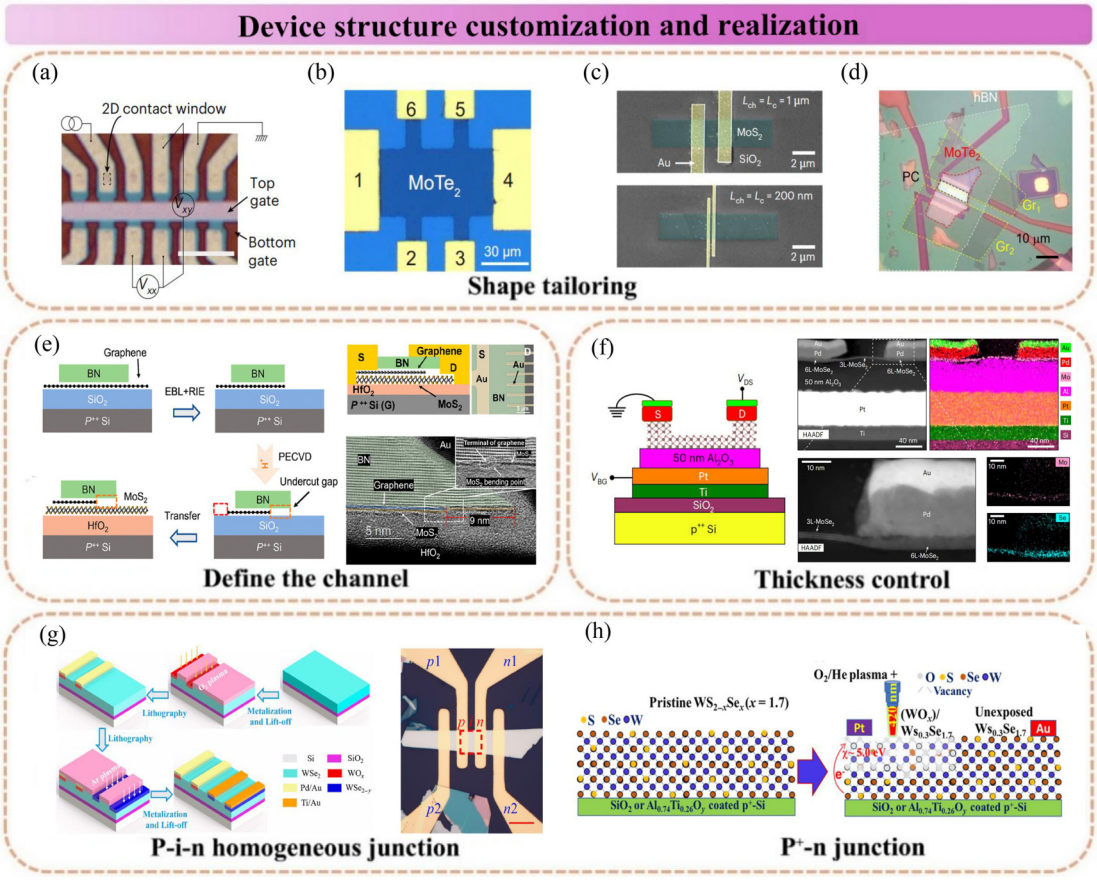


Figure 10 Plasma-enabled structure engineering of 2D materials for advanced nanoelectronic device applications. (a) Optical image of a typical dual-gated bilayer MoS_2 device. Reproduced with permission from Ref. [145], © Zhao, S. W. et al. 2024. (b) Optical micrograph of a typical 2H-$MoTe_2$ Hall device. Reproduced with permission from Ref. [54], © Pan, Y. et al. 2024. (c) Top-down, false-colour, scanning electron microscope images of a long device with $L_{ch} = L_c = 1$ μm and a short device with $L_{ch} = L_c = 200$ nm. Reproduced with permission from Ref. [147], © Jaikissoon, M. et al. 2024. (d) Optical micrograph of the $MoTe_2$/pentacene heterostructure device, consisting of the pentacene/$MoTe_2$/hBN/Gr on SiO_2 substrate. Reproduced with permission from Ref. [146], © Jang, Y. J. et al. 2023. (e) TEM image of hydrogen plasma-etched graphene/BN heterostructures, forming undercut nanogaps for ultra-short-channel MoS_2 FETs with a minimum channel length of 9 nm, exhibiting high current density, low DIBL, and excellent switching performance. Reproduced with permission from Ref. [148], © American Chemical Society 2023. (f) Layer-by-layer thinning of $MoSe_2$ enabled by plasma oxidation and selective MoO_3 removal, yielding significant improvement in on/off ratio by five orders of magnitude compared to unthinned devices. Reproduced with permission from Ref. [55], © Das, M. et al. 2024. (g) Self-aligned plasma doping of WSe_2 to form a homojunction p-i-n diode with ideal rectifying behavior and enhanced photodetection under 450 nm illumination. Reproduced with permission from Ref. [150], © American Chemical Society 2021. (h) Selective oxidation of $WS_{0.3}Se_{1.7}$ using O_2/He plasma to create a high-quality p^+-n junction with improved current–voltage rectification behavior. Reproduced with permission from Ref. [151], © American Chemical Society 2023.

producing undercut nanogaps with controlled geometries [148]. By tuning the etching conditions (such as temperature, pressure, and radio frequency power), researchers achieved accurate modulation of nanogap size, enabling deterministic definition of MoS_2 FETs as shown in Fig. 10(e). Using this method, they successfully prepared MoS_2 FETs with channel length of 9 nm, and these devices demonstrated excellent performance, including a high on-state current density of 734/433 μA·μm^{-1} at V_{DS} = 2/1 V, a record-low drain-induced barrier lowering (DIBL) of 50 mV·V^{-1}, a superior on/off ratio of 3 × 10^7, and a low subthreshold swing of 100 mV·dec^{-1}.

Furthermore, the oxidation effect of plasma facilitates the layer-by-layer thinning of 2D materials, enabling precise thickness control, which is crucial for the preparation of high-performance FETs. As shown in Fig. 10(f), by oxidizing $MoSe_2$, a passivated and substoichiometric MoO_3 layer is formed on the surface of the top material, which can protect the underlying material from further oxidation or corrosion [55]. The formed MoO_3 layer can be selectively dissolved in deionized water. By repeating this process, materials in the 2D channel region (i.e., the region between the source and drain) are removed layer by layer, while the material beneath the contacts remains unaffected. Compared to unthinned devices, the switch ratio of thinned $MoSe_2$ is improved by five orders of magnitude.

4.1.2 *P-type doping and pn junction formation*

While most TMDs inherently exhibit n-type or ambipolar conductivity, the lack of stable p-type doping remains a major bottleneck for implementing p-type FETs, thus constraining their integration into complementary logic circuits [149]. Among various doping strategies, plasma doping emerges as a highly promising approach, owing to its industrial compatibility, post-fabrication applicability, and process-level controllability. It not only enables stable p-type doping across a variety of 2D materials, but also facilitates the construction of high-quality p-n junctions via spatially selective doping or vertical heterostructure stacking, offering broad potential in photoelectronic devices and integrated circuit applications.

For instance, Zhang et al. utilized a self-aligned surface plasma treatment to fabricate a WSe_2 homojunction p-i-n diode [150], as shown in Fig. 10(g). The diode exhibited ideal rectification behavior with a current on/off ratio as high as 1.2×10^6 and an ideality factor of 1.14. In photovoltaic mode, the diode demonstrated excellent photodetection performance under 450 nm illumination, including an open-circuit voltage of 340 mV, a responsivity of 0.1 $A \cdot W^{-1}$, and a specific detectivity of 2.2×10^{13} Jones. In another study, Kuddus et al. employed O_2/He plasma irradiation to selectively oxidize WSe_2 surfaces [151]. The oxidation was initiated at sites such as edges, vacancies, and dangling bonds, leading to the formation of a high-quality p^+-n junction between $WS_{0.3}Se_{1.7}$ and $(WO_x)/WS_{0.3}Se_{1.7}$, which significantly enhanced the rectification behavior of the current–voltage characteristics, as shown in Fig. 10(h). Additionally, Wang et al. demonstrated the fabrication of a MoS_2 CMOS inverter via region-selective oxygen plasma doping using a metal mask [30]. The inverter, operating at V_{dd} = 5 V conditions, exhibited a peak voltage gain of 7.48 and a maximum static power consumption of only 37.7 nW. The plasma-enabled doping led to improved V_{in}–V_{out} matching, demonstrating the viability of plasma doping for logic-level circuit implementation.

4.2 Interface and contact optimization

The performance and reliability of 2D material-based devices are intimately governed by the quality of their interfaces including those with dielectric layers, metal electrodes, and supporting substrates. Given the atomic-scale thickness of 2D materials, even minute interfacial impurities, lattice mismatches, or weak bonding interactions can significantly deteriorate electrical performance, introduce trap states, or hinder efficient carrier injection. Therefore, achieving precise interfacial engineering and contact optimization is essential to unlock the full potential of 2D semiconductors for next-generation nanoelectronics.

In this context, plasma treatment technology has become an indispensable tool that enables atomic-scale surface chemistry and interface state regulation. On one hand, plasma-assisted cleaning protocols can effectively remove polymeric and organic residues introduced during exfoliation and transfer, thus improving material quality and promoting strong coupling with adjacent layers. On the other hand, plasma-induced surface activation or mild oxidation can significantly enhance adhesion and nucleation uniformity, offering critical advantages for the integration of high-k gate dielectrics and heterogeneous structures. The following subsections explore recent advances in the optimization of interface and contact of devices through plasma treatment.

4.2.1 *Surface cleaning*

During the fabrication of 2D material devices, it is often necessary to transfer them from the growth substrate or bulk material to the desired target substrate. However, existing transfer methods may introduce contaminants, particularly polymer residues, which adversely affect the quality and performance of 2D materials. Plasma treatment is effective in removing contaminants such as oxides from the substrate or polydimethylsiloxane (PDMS) surface. Rokni et al. found that oxygen plasma treatment can completely remove water and hydrocarbon molecules, leaving a contamination-free silicon dioxide surface. Jain et al. pre-cleaned the PDMS surface with ultraviolet-ozone before exfoliation [152], significantly reducing organic residues on the transferred MoS_2 flakes (Fig. 11(a)) [153]. Xia et al. reported oxygen plasma can remove the residual molecules within a short irradiation time (Figs. 11(b) and 11(c)) [154]. Furthermore, plasma treatment can enhance adhesion between 2D materials and other materials, such as metal electrodes, by improving their interfacial quality. For instance, Kwon et al. used oxygen plasma to completely remove contaminants from the gold surface and enhance adhesion before transferring MoS_2 to the metal electrode [155]. Plasma can also directly clean the surface of 2D materials, removing residual polymers within a short period (a few minutes). Marinov et al. found that compared to the acetone soaking method, hydrogen plasma is more efficient and thorough in removing poly(methyl methacrylate) (PMMA) residues from WS_2 surfaces [95]. By controlling the substrate temperature during the cleaning process, plasma-induced damage to the WS_2 lattice can be reduced.

4.2.2 *High-k dielectric integration*

Ultra-thin high-k gate dielectrics play a crucial role in suppressing gate leakage current, enhancing device performance, and driving the development of 2D integrated circuits, which is key to the success of 2D FETs in advanced technologies. However, the lack of chemical reaction bonds on the surface of TMDs limits the ability to use standard atomic layer deposition (ALD) processes for uniform nucleation and growth of high-k dielectrics. Plasma pretreatment-assisted atomic layer deposition (PPA-ALD) first employs plasma treatment on the surface of TMDs by intentionally creating defects and generating reactive radicals, thereby generating more nucleation sites and providing better chemical bonding ability for the deposition of high-k dielectrics. As shown in Fig. 11(d), Lee et al. used BCl_3 plasma to generate BCl radicals, which adsorbed onto the MoS_2 surface and promoted chemical reactions with aluminum precursors, improving the coverage and conformality of the Al_2O_3 film on MoS_2 surface and successfully fabricating a top-gate FET with good electrical characteristics (using an ultra-thin ALD-Al_2O_3 gate dielectric ~ 5 nm thick) [156]. Additionally, modifying the ALD process by introducing plasma during ALD, known as PEALD (Fig. 11(e)), can also change the surface properties of TMDs and ultimately promote nucleation [33]. PEALD introduces plasma during one of the pulsing steps to assist in precursor cracking. Compared to thermal ALD processes where reactions are purely driven by thermal energy, PEALD offers advantages such as lower growth temperatures, higher-quality films, and shorter deposition times.

4.2.3 *Contact resistance optimization*

High resistance at the interface between metal electrodes and 2D materials poses a critical challenge for the application of 2D materials in next-generation electronic devices. Phase engineering, which involves modulating the phase transition from semiconductor to metal in 2D semiconductors, is considered an effective approach to mitigate the high contact resistance issue at the metal/2D semiconductor interface [134]. Zhu et al. employed Ar ion bombardment with a certain kinetic energy on 2H-phase MoS_2, effectively triggering lateral sliding of the top S layer and forming 1T-phase nanostructures [157]. Using lithography, they selectively induced the 1T phase transition within the metal contact area, resulting in MoS_2 transistor devices with lower contact resistance. Oyedele et al. generated selenium vacancies in few-layer $PdSe_2$ crystals using Ar plasma, triggering a phase transition from layered $PdSe_2$ to non-layered $Pd_{17}Se_{15}$, and forming an atomically sharp $Pd_{17}Se_{15}/PdSe_2$ interface with the original $PdSe_2$ [158]. These

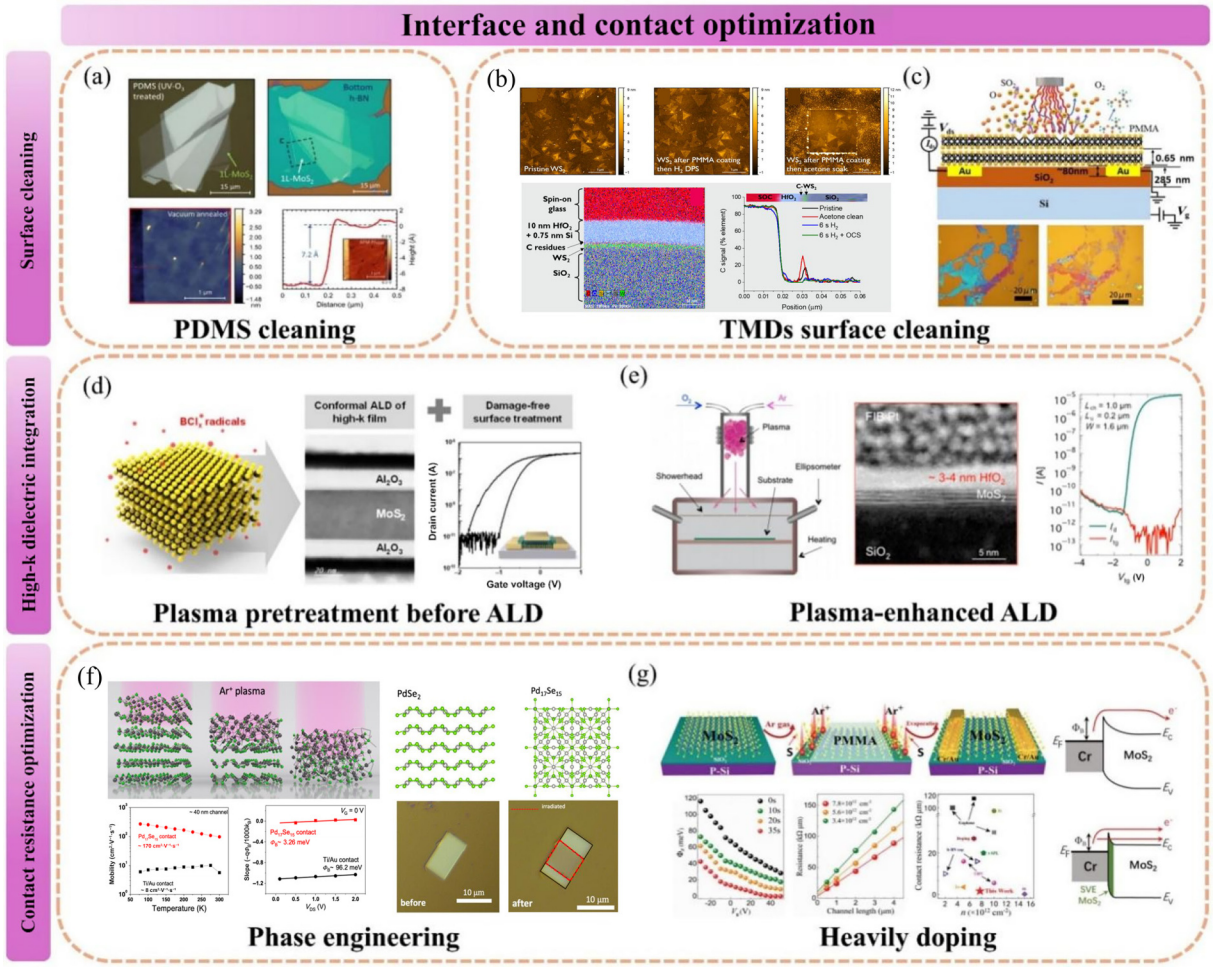


Figure 11 Plasma-enabled interface and contact engineering for 2D devices. (a) AFM images of UV-ozone pre-treatment and PDMS exfoliation, reducing polymer residue on MoS_2 surfaces for improved cleanliness. Reproduced with permission from Ref. [152], © IOP Publishing Ltd. 2018. (b) Optical and AFM images showing surface cleaning effects of O_2 plasma on transferred MoS_2, revealing effective removal of molecular residues within seconds. Reproduced with permission from Ref. [95], Marinov, D. et al. 2021. (c) Schematic diagram of H_2 plasma and SnS_2 sample respectively before and after the H_2 plasma treatment. Reproduced with permission from Ref. [154], © IOP Publishing Ltd. 2021. (d) BCl_3 plasma pretreatment generating BCl radicals that promote uniform nucleation and ALD growth of Al_2O_3 on MoS_2, leading to a high-performance top-gate FET with a 5 nm gate dielectric. Reproduced with permission from Ref. [156], © American Chemical Society 2023. (e) Concept of PEALD where plasma assists precursor activation and enhances film quality at lower temperatures. Reproduced with permission from Ref. [33], © American Chemical Society 2017. (f) Schematic and cross-section of $PdSe_2$ device with Ar plasma-induced selenium vacancy formation, leading to a low-barrier $Pd_{17}Se_{15}/PdSe_2$ contact and enhanced mobility. Reproduced with permission from Ref. [158], © American Chemical Society 2019. (g) Mild Ar plasma-induced sulfur vacancy formation in monolayer MoS_2 enabling n-type doping and ultralow contact resistance (~ 1.7 kΩ·μm), resulting in improved ohmic contact. Reproduced with permission from Ref. [159], © Wiley-VCH GmbH 2023.

$Pd_{17}Se_{15}$ contact points exhibited a low contact resistance of 0.75 kΩ·μm and a Schottky barrier height of 3.3 meV, leading to a nearly 20-fold increase in carrier mobility in $PdSe_2$ transistors compared to traditional Ti/Au contacts (Fig. 11(f)). Additionally, heavily doping of semiconductor contacts with plasma to reduce the Schottky barrier width at the metal/semiconductor interface, thereby enhancing carrier transport efficiency at the interface, is also an effective strategy for improving contact resistance. As shown in Fig. 11(g), Xiao et al. achieved ohmic contact between metal and monolayer MoS_2 by introducing a large number of n-doped sulfur vacancies and surface dangling bonds in the contact area through precisely controlled mild Ar plasma etching, resulting in a contact resistance as low as 1.7 kΩ·μm for monolayer MoS_2 FETs [159].

4.3 Boosting device performance through plasma treatment

Beyond structural customization and interfacial optimization, plasma technology plays an increasingly pivotal role in directly enhancing the performance of 2D materials and their corresponding device applications [160]. By enabling precise control over surface chemistry, phase composition, doping concentration, and defect states, plasma offers unprecedented opportunities to modulate the electronic, optical, and neuromorphic properties of 2D semiconductors which are critical for sensing, photodetection, and memory systems. To provide a comprehensive overview of how plasma treatment has been leveraged to enhance the performance of TMDs, Table 2 summarizes representative studies across various application domains. Plasma treatment provides an efficient platform for post-synthetic engineering of 2D materials due to its high reactivity and compatibility with low-temperature processes. It can controllably generate or repair vacancies, adjust interfacial band alignment, and even achieve phase transitions between semiconductor and metallic phases, thereby effectively enhancing device performance. In

Table 2 Summary of plasma-engineered TMDs for device performance optimization

TMDs	Plasma	Function	Processing parameter	Device	Performance	Refs.
MoS_2	N_2	Doping	Power: 20 W Time: 30 s Flow: 300 mL·min^{-1}	FET	rectification ratio: 3.1 × 10^{-3} reverse current: 10 pA Hole mobility: 4.6 cm^2·V^{-1}·s^{-1}	[24]
MoS_2	O_2	Doping	Pressure: 5 Pa Power: 5 W Time: 10–20 s Flow: 60 sccm	CMOS inverter	Mobility: 40 cm^2·V^{-1}·s^{-1} (n) 120 cm^2·V^{-1}·s^{-1} (p) Peak voltage gain: 7.48 (V_{dd} = 5 V) Power consumption: 37.7 nW NM low: 0.45 V_{dd} NM high: 0.32 V_{dd}	[30]
WSe_2	O_2	Doping	Pressure: 30 mTorr Power: 50 W Time: 200 s Flow: 50 sccm	Seamless p$^+$-p junction diode	I_{on}/I_{off} ratio: 10^9 Hole mobility: 108 cm^2·V^{-1}·s^{-1} Contact resistance: 4 kΩ·μm Saturation current: −280 μA·μm^{-1}	[163]
WS_2	NH_3	Doping	Temperature: 120–210 °C Time: 30–120 min Flow: 80 sccm	Photodetector	Photoresponsivity: 2.97 A·W^{-1} Specific detectivity: > 10^{10} Jones (at λ = 532 nm) EQE: 699% I_{on}/I_{off} ratio: > 10^8	[164]
WSe_2	O_2	Doping	Time: 30–60 s	FET	I_{on}/I_{off} ratio: > 10^5 Field-effect mobility: 2.2 cm^2·V^{-1}·s^{-1}	[165]
MoS_2 WeS_2	SF_6	Etching	Pressure: 180 mTorr Temperature: 35 °C Flow: 50 sccm	n-p-n selector	Nonlinearity: ~ 230 Current density: 2 × 10^3 A·cm^{-2}	[166]
MoS_2	Ar	Etching	Pressure: 0.5 Pa Power: 30 W Temperature: 250 °C Time: 30 s Flow: 10 sccm	FET	I_{on}/I_{off} ratio: 10^9–10^{11} Field-effect mobility: 1200 cm^2·V^{-1}·s^{-1}	[86]
MoS_2	SF_6	Etching	Pressure: 1 Torr Power: 10 W Frequency: 50 kHz Time: 30–50 s Flow: 10 sccm	FET	I_{on}/I_{off} ratio: 1.3 × 10^7 (triple layer), 7.1 × 10^6 (double layer), 3.2 × 10^6 (monolayer) Field-effect mobility: 16.2 cm^2·V^{-1}·s^{-1} (triple layer), 8.84 cm^2·V^{-1}·s^{-1} (double layer), 2.87 cm^2·V^{-1}·s^{-1} (monolayer)	[32]
MoS_2	$H_2/O_2/SF_6$	Etching	Pressure: 1 Torr Power: 200 W Time: 30 s/15 s/15 s Flow: 200 sccm/200 sccm/50 sccm	Photodetector	Photoresponsivity: 1.39 A·W^{-1} Response time: 0.45 s	[168]
SnS_2	H_2/O_2	Etching doping	Pressure: 1 Torr Power: 7.2 W Frequency: 13.56 MHz Time: 3–60 s Flow: 5 sccm	TFTs	Mobility: 2.5 cm^2·V^{-1}·s^{-1} Response time: 20 ms	[154]
$MoTe_2$	Ar	Etching	Pressure: 2.66 Pa Power: 90 W (E)/120 W (H) Ar Flow: 10 sccm	FET	I_{on}/I_{off} ratio: 6 × 10^2 Field-effect mobility: 543.9 cm^2·V^{-1}·s^{-1} Contact resistance: 12.3 kΩ·μm SBH: 13.2 meV	[31]
WSe_2	UV-O_3	Etching	Time: 30 min	FET	I_{on}/I_{off} ratio: 10^5 Hole mobility: 515 cm^2·V^{-1}·s^{-1}	[169]
WSe_2	O_2	Defect doping	Pressure: 100 mTorr Power: 150 W Temperature: 150 °C Time: 5–60 s Flow: 60 sccm	p-n junction	Rectification ratio: 330 (V_{GS} = −20 V)	[77]
$MoTe_2$	Ar	Defect	Power: 50 W Time: 120 s	Memristor	Switching stability: > 200 cycles Retention characteristics: > 10^5 s Gesture recognition accuracy: > 70% at 50% background noise	[170]
$PtSe_2$	Ar	Defect	Power: 5–15 W Time: 15 s	FET	Field-effect mobility: 515 cm^2·V^{-1}·s^{-1} Overpotential: ~11 mV at 10 mA·cm^{-2} Tafel slope: ~ 48 mV·dec^{-1} Exchange current density: ~ 447 μA·cm^{-2}	[116]
WS_2	Ar	Defect	Pressure: 10 Pa Time: 3 min Flow: 40 sccm	LED	FWHM: 490 meV EQE: 1.39%	[22]
$MoTe_2$	Ar	Defect	Power: 20 W Temperature: 150 °C Time: 150 s Flow: 50 sccm	Memristor	SET: 5 ns RESET: 10 ns Cycling endurance: > 10^5 Retention characteristic: > 10^5 s	[34]

(Continued)

TMDs	Plasma	Function	Processing parameter	Device	Performance	Refs.
WS_2	Ar/O_2	Defect	Pressure: 1 Pa RF/ICP power: 4/20 W/2/10 W/1/5 W Temperature: 20 °C Time: 10 s Flow: 3 sccm	Photodetector	I_{on}/I_{off} ratio: ~ 6.5×10^5 Photocurrent: 0.41 μA τ_r: 270 μs τ_f: 99 μs	[106]
MoS_2	Ar	Defect	Power: 45 W Time: 10–35 s Flow: 40 sccm	FET	I_{on}/I_{off} ratio: 4×10^9 Field-effect mobility: 153 $cm^2 \cdot V^{-1} \cdot s^{-1}$ Saturation current: 342 $\mu A \cdot \mu m^{-1}$ Contact resistance: 1.7 kΩ·μm	[159]
MoS_2 WS_2	H_2S/Ar	Synthesis	Pressure: 100 mTorr Power: 550 W Temperature: 300 °C Time: 90 min Flow: 10/40 sccm	Diodes	Average current: 0.375 μA	[43]
$MoTe_2$	O_2	Synthesis doping	Pressure: 2 mTorr Power: 10 W Time: 5 min Flow: 10 sccm	OLED	EQE: 17.9% L_{max}: 2844 $cd \cdot m^{-2}$ CE_{max}: 41.1 $cd \cdot A^{-1}$	[39]
MoS_2 WS_2	H_2S	Synthesis	Pressure: 100 Torr Temperature: < 200 °C Time: 90 min	Photodiode	Responsivity: 37 $mA \cdot W^{-1}$ (MoS_2/Si)/60 $mA \cdot W^{-1}$ (WS_2/Si)	[40]
MoS_2 WS_2	H_2	Synthesis	Pressure: 1×10^{-2} Torr Power: 23 W Temperature: 200–600 °C Time: 50 min Flow: 200 sccm	FET	I_{on}/I_{off} ratio: 10^4 (200 °C) Field-effect mobility: 0.87 $cm^2 \cdot V^{-1} \cdot s^{-1}$ (200 °C)	[38]
1T-MoS_2	H_2S/Ar	Synthesis	Pressure: 100 mTorr Power: 550 W Temperature: 150 °C Time: 1.5 h Flow: 10/10 sccm	HER catalyst	Overpotential: 0.29 mV at 5 $mA \cdot cm^{-2}$ Tafel slope: 78 $mV \cdot dec^{-1}$	[42]

addition, plasma-assisted processes are scalable and compatible with CMOS, making them particularly attractive for the development of high-performance, low-power, and miniaturized 2D electronics.

Despite the advantages of plasma treatment, long-term stability remains a significant concern for practical applications. Reported instability effects include temporal degradation of doping effects (e.g., reduction in p-type character) and irreversible decline in optoelectronic performance due to lattice damage. These issues primarily stem from energetic ion bombardment and the formation of sulfur vacancies caused by reactive species such as oxygen radicals. Effective mitigation strategies include using low-damage plasma sources (e.g., remote plasma, low-power ICP), introducing chemical passivation layers (e.g., AlO_x) [161], and employing *in situ* high-k dielectric encapsulation. Additionally, substitutional doping with stronger chemical bonding (e.g., W–N bonds) offers greater thermal and environmental stability compared to surface adsorption methods [162]. This section focuses on the crucial role of plasma treatment in enhancing the performance of various devices.

4.3.1 *Gas sensing applications: Enhanced sensitivity and selectivity*

TMDs have emerged as promising candidates for gas sensors due to their unique physicochemical properties [171–175], including abundant active sites, low energy consumption, and the ability to operate at RT [176–178]. However, the intrinsic gas sensing performance of TMDs is limited by several factors, such as weak adsorption capabilities, low carrier concentration and mobility, and uneven distribution of surface active sites, which restrict their sensitivity, response time, and recovery time. Plasma treatment, as an effective surface modification and engineering technique, has been demonstrated to significantly enhance the gas sensing performance of TMDs.

One of the primary mechanisms by which plasma treatment improves gas sensing is through the introduction of defects on the material surface [179]. These defects create shallow electron traps that act as active adsorption sites, thereby enhancing the gas adsorption capacity of TMDs [180]. For example, Kumar et al. [181] investigated the effect of N_2 plasma treatment duration on the NO_2 gas sensing properties of SnS_2 nanosheets. The principle structure diagram of treating SnS_2 nanosheets with N_2 plasma is shown in Fig. 12(a). As shown in Fig. 12(b), their findings revealed significant changes in response, response time, and recovery time with increasing plasma exposure duration. At an operating temperature of 120 °C, SnS_2 treated with plasma for 12 min exhibited a remarkable NO_2 response of 246.30% and a low detection limit of 110 ppb, with response and recovery times of 27 and 183 s, respectively. This enhancement was attributed to the generation of S vacancies, which increased the number of gas adsorption sites. However, beyond 12 min of plasma treatment, the response decreased due to the occupation of a large number of S vacancies by nitrogen atoms (Fig. 12(c)).

Plasma treatment can also optimize the gas sensing performance of TMDs by adjusting the ratio of the 1T and 2H phases of TMDs. The electrical properties of the 1T and 2H phases of TMDs exhibit significant differences. The 2H phase is a semiconductor that can effectively interact with gas molecules, but it has poor conductivity and low electrical conductivity. Conversely, the 1T phase is metallic

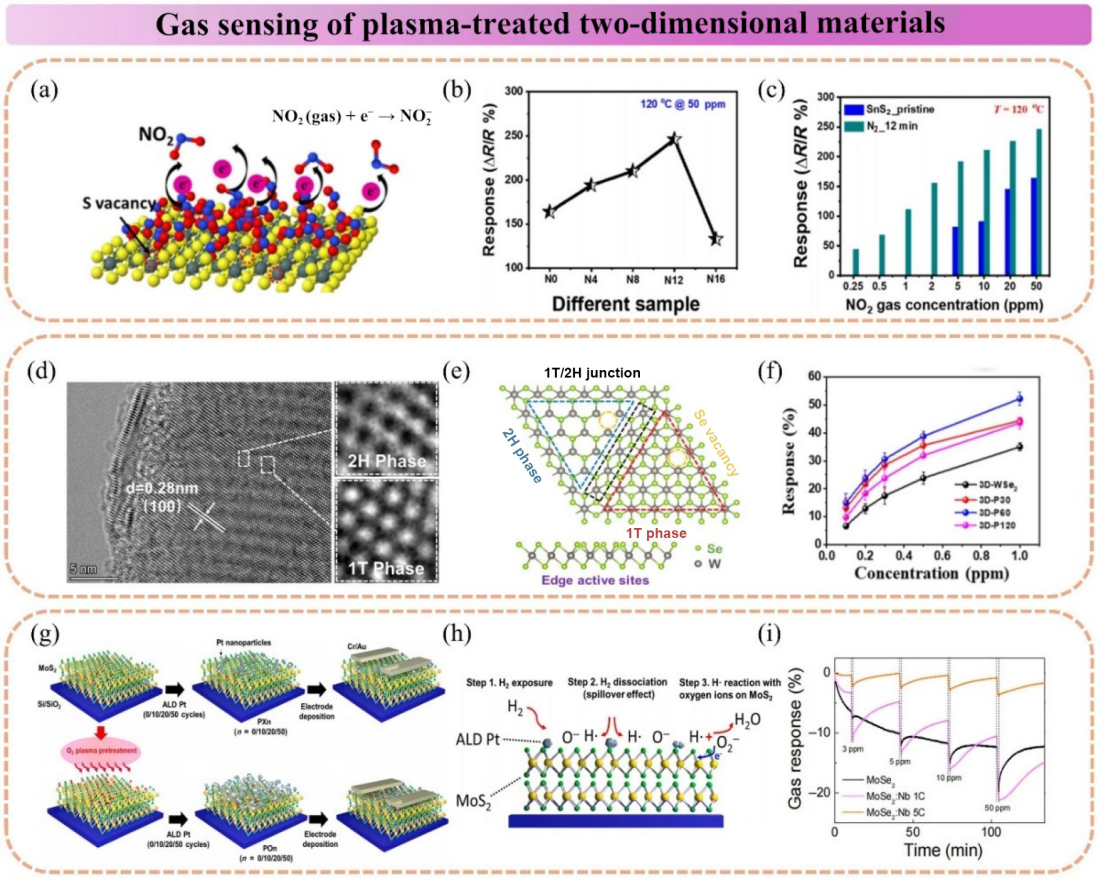


Figure 12 Plasma-enhanced gas sensing performance of 2D TMDs. (a) Schematic of N_2 plasma treatment on SnS_2 nanosheets for NO_2 sensing enhancement. (b) Response variation of SnS_2 to NO_2 under different plasma exposure durations; optimal performance at 12 min. (c) Response–concentration plot of pristine and N12 samples. Reproduced with permission from Ref. [181], © American Chemical Society 2023. (d) HRTEM image showing phase transition from 2H to 1T in WSe_2 nanosheets induced by Ar/H_2 microwave plasma. (e) Atomic model of the resulting 1T/2H mixed-phase WSe_2 structure with Se vacancies. (f) Gas sensing performance of 3D-WSe_2 nanosheets before and after plasma treatment toward 1 ppm NO_2. Reproduced with permission from Ref. [183], © Elsevier B.V. 2023. (g) Fabrication process of ALD-deposited Pt on MoS_2 surface pretreated by oxygen plasma. (h) Schematic of H_2 sensing mechanism for ALD-Pt/MoS_2 heterostructure with enhanced Pt distribution. Reproduced with permission from Ref. [185], © Elsevier B.V. 2021. (i) Comparison of NO_2 sensing responses in Nb-doped $MoSe_2$ prepared by PEALD with varying doping cycles. Reproduced with permission from Ref. [186], © American Chemical Society 2017.

with excellent conductivity but weak adsorption capacity for gas molecules [177, 182]. High-energy particles in the plasma can engage in substitution reactions with the atoms in TMDs, locally altering bond lengths and electron cloud distributions, thereby disrupting the original crystal structure and inducing a phase transition from 2H to 1T. This phase transition not only significantly enhances the electrical conductivity of the material but also improves its responses to gas molecules. Duan et al. [183] successfully constructed a 1T/2H hybrid phase structure and introduced selenium vacancies in a three-dimensional (3D) WSe_2 nanosheet array through self-made microwave plasma (mainly consisting of Ar ions and H_2 ions), significantly enhancing the gas sensing performance of the 3D WSe_2 nanosheet array. As shown in Fig. 12(d), the high-resolution transmission electron microscopy (HRTEM) images indicated a partial transition of WSe_2 from the 2H phase to the 1T phase, the molecular model of WSe_2 after plasma treatment is shown in Fig. 12(e), forming a material with a finger-like 1T/2H multiphase structure. The plasma-treated samples exhibited a response value of 52.24% to 1 ppm NO_2, with a response time of 49.8 s and a recovery time of 14.9 min (Fig. 12(f)), all of which significantly outperformed the untreated original 3D-WSe_2 films.

Furthermore, plasma treatment enhances gas sensing performance by introducing/activating surface functional groups (e.g., hydroxyl, carboxyl, amino groups). These functional groups not only enhance the surface chemical activity of TMDs but also optimize the distribution and stability of nanoparticles, thereby increasing their adsorption and reactivity towards gas molecules [184]. Lee et al. [185] induced the uniform distribution of Pt nanoparticles on the MoS_2 surface through oxygen plasma pretreatment and significantly enhanced hydrogen gas sensor performance by optimizing the number of ALD cycles. Figure 12(g) shows the process diagram for the plasma treatment of MoS_2. The oxygen plasma pretreatment increased the initial nucleation sites on the MoS_2 surface, promoting a more uniform nucleation and growth of Pt nanoparticles, thus enlarging the surface coverage area. The H_2 sensing mechanism of the ALD-Pt modified MoS_2 sensor is shown in Fig. 12(h). Experimental results indicated that the sample subjected to 10 ALD cycles (PO10) exhibited excellent H_2 sensing performance, with a sensitivity exceeding 400 to 1000 ppm H_2 and a good linear response to different H_2 concentrations.

Additionally, PEALD technology allows for precise control of doping concentrations, ensuring that dopant atoms are uniformly distributed. By utilizing PEALD to deposit Nb_2O_5, the doping

concentration of Nb in $MoSe_2$ can be accurately adjusted, and different doping concentrations can be achieved by varying the number of deposition cycles [186]. As shown in Fig. 12(i), the device with low-concentration Nb doping ($MoSe_2$:Nb 1C) has the highest gas sensing response. The response can reach 8% under 3 ppm of NO_2, while the gas sensing response of the device with high-concentration doping ($MoSe_2$:Nb 5C) decreases instead. Appropriate Nb doping can significantly enhance gas sensitivity and improve device stability. However, excessive Nb doping may reduce gas sensitivity due to the increased metallic regions.

4.3.2 Optoelectronic devices optimization: From dark current suppression to spectral broadening

In the field of optoelectronic devices, plasma treatment technology enables precise regulation of surface chemical states, defect distribution, doping characteristics, and interfacial band structures in 2D TMDs. This technique demonstrates unique advantages in dark current suppression, response time optimization, sensitivity enhancement, and spectral range extension, providing crucial technical pathways for developing high-performance 2D TMDs photoelectric devices. Its applications show broad prospects in optical communications, infrared imaging, and spectral detection. This part systematically summarizes the key performance improvements from four aspects: dark current, response time, photoresponsivity, and spectral range.

Dark current suppression. Dark current serves as a critical parameter affecting device signal-to-noise ratio and sensitivity [187]. Plasma treatment effectively suppresses dark current through mechanisms including surface defect state modulation and energy band structure engineering. For instance, O_2 plasma treatment of BP forms a stable P_xO_y protective layer while introducing acceptor trap states near the conduction band [188]. These defect states effectively capture free electrons, reducing carrier concentration and decreasing dark current in BP field-effect transistors by three orders of magnitude. Band structure modification represents another suppression mechanism [75]. Shin et al. demonstrated that O_2 plasma-induced WO_x layer on WSe_2 facilitates p-type doping [76]. This shifts the Fermi level toward the valence band, enhancing built-in potential at the WSe_2/WO_x heterojunction and promoting photogenerated carrier separation. Concurrently, the WO_x layer acts as a hole-blocking layer, restricting hole transport at the interface and suppressing dark current to pA levels. Similarly, Yue et al. constructed a lateral p-n homojunction in WSe_2 through selective O_2 plasma treatment [189]. As shown in Fig. 13(a), this structure reduces interface defects and carrier recombination, achieving an ideal factor (n) of 1.4 (Fig. 13(b)) and near-zero dark current under reverse bias (Fig. 13(c)).

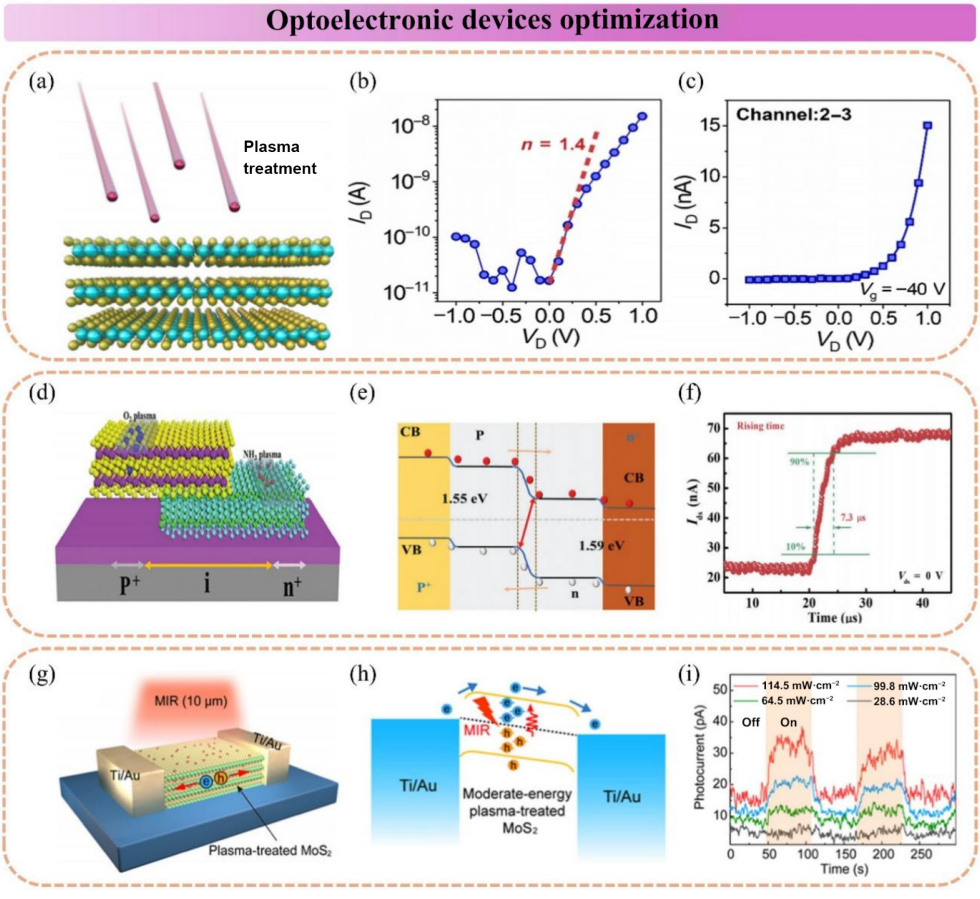


Figure 13 Optoelectronic performance enhancement in plasma-treated 2D devices. (a) Device structure of lateral WSe_2 homojunction photodetector with selective O_2 plasma treatment. (b) Extracted ideality factor indicating reduced interface recombination (n = 1.4). (c) Dark current suppression under reverse bias, approaching zero. Reproduced with permission from Ref. [189], © The Royal Society of Chemistry 2023. (d) Device schematic of WSe_2/MoS_2 vertical p-i-n heterojunction formed by NH_3/O_2 plasma doping. (e) Band diagram of p-i-n vertical heterojunction. (f) Temporal photoresponse profile showing rapid response time of 7.3 μs. Reproduced with permission from Ref. [121], © Wiley-VCH GmbH 2025. (g) Schematic of MoS_2 with mid-gap states introduced by medium-energy O_2 plasma treatment. (h) Spectral responsivity extended to mid-infrared range (~ 10 μm). (i) Stable photocurrent under 10 μm illumination, confirming long-wavelength detection capability. Reproduced with permission from Ref. [35], © American Chemical Society 2023.

Response time optimization. Response speed critically determines device dynamic performance [190]. Plasma treatment enables localized doping through patterned masks (e.g., BN or photoresist) to construct p-n or p-i-n junctions. The enhanced built-in electric field in these junctions accelerates carrier separation and directional transport, thereby reducing response time [71, 191]. Li et al. achieved n-type doping in WSe_2 via SF_6 plasma-induced Se vacancy defects, forming a homojunction with intrinsic WSe_2 [70]. The resultant built-in field enabled rapid carrier separation, yielding a 10 μs response time. The p-i-n configuration further expands depletion width and reduces junction capacitance, minimizing carrier transport time constant. Wu et al. fabricated a WSe_2/MoS_2 vertical p-i-n heterojunction detector using NH_3/O_2 plasma selective doping [121]. As illustrated in Figs. 13(d) and 13(e), the plasma-treated regions formed doped contacts while maintaining an intrinsic interlayer. This structure achieved a 7.3 μs response time (Fig. 13(f)).

Photoresponsivity enhancement. Photoresponsivity quantifies photoelectric conversion efficiency [192]. Plasma treatment induces semiconductor-to-metallic phase transitions in TMDs, significantly reducing Schottky barrier height and improving carrier injection efficiency. Zhang et al. demonstrated O_2 plasma-induced metallic phase transformation in $PdSe_2$ [193]. The metallic contacts lowered injection barriers, increasing responsivity from 15.7 to 34.4 $A{\cdot}W^{-1}$. Defect engineering via plasma treatment (e.g., chalcogen vacancy creation) prolongs carrier lifetime through trap-state-mediated photogating effects. Quan et al. achieved 28 $A{\cdot}W^{-1}$ responsivity in SnS_2 by O_2 plasma-generated electron traps that modulate channel conductivity [192]. Li et al. introduced sulfur vacancies in MoS_2 via H_2 plasma treatment [161]. These vacancies acted as hole traps, suppressing recombination and achieving 567 $A{\cdot}W^{-1}$ responsivity with Al_2O_3/HfO_2 passivation. Ar-O_2 plasma treatment creates TMD/TMO heterojunctions that enhance photon absorption and carrier separation, boosting photocurrent by 150 orders [194].

Spectral range extension. Spectral range determines device wavelength applicability [195]. Plasma treatment introduces mid-gap states, atomic-scale oxidation layers, and doping to reduce effective bandgap. Wu et al. employed medium-energy (70–130 eV) O_2 plasma treatment to create in-gap states in MoS_2 [35]. As shown in Figs. 13(g) and 13(h), this extended detection to mid-infrared (10 μm), with stable photoresponse at 10 μm (Fig. 13(i)). Huang et al. achieved near-infrared (980 nm) response in $MoSe_2$ through O_2 plasma-induced Se substitution and bandgap reduction (PL redshift from 810.5 to 837.8 nm) [196]. Liu et al. demonstrated nitrogen plasma-induced p-doping in MoS_2, introducing impurity states that reduced bandgap from 1.6 to 1.56 eV and extended response to short-wave infrared (1550 nm) [123].

4.3.3 Plasma-treated 2D materials for memristive devices: Memory and neuromorphic computing

TMDs have emerged as ideal materials for constructing high-performance memristors due to their atomic-scale thickness, ultrahigh specific surface area, tunable phase transition characteristics, and compatibility with CMOS processes [197–199]. However, the intrinsic limitations of pristine TMDs, including high phase transition energy barriers, low defect densities, and inherent electrical constraints, often result in inadequate memristive properties for practical applications [200, 201]. Plasma treatment technology has demonstrated critical potential for optimizing memristor performance (e.g., switching ratio, endurance, and synaptic plasticity) through precise regulation of defect distribution, phase transitions, and interfacial characteristics in TMDs.

Plasma-induced defect engineering for phase transition modulation. Plasma treatment enables dynamic phase transition control by introducing defects (e.g., Te/S vacancies) that modify band structures and interatomic interactions [167]. Chen et al. [170] successfully engineered Te vacancy defects in $MoTe_2$ films using Ar plasma [34]. The device structure is illustrated in Fig. 14(a). Under electric fields, the directional migration of Te vacancies significantly reduced the energy barrier (ΔE) between 2H and 1T' phases, triggering reversible 2H to 1T' phase transitions. This defect-mediated mechanism allowed effective emulation of biological synaptic behaviors, including long-term potentiation (LTP) and depression (LTD). As shown in Fig. 14(b), a three-layer convolutional neural network (CNN) architecture was constructed for gesture recognition testing. The corresponding artificial neural network demonstrated remarkable noise immunity, achieving > 70% gesture recognition accuracy under 50% noise interference after 50 training cycles, with accuracy reaching 98.56% at 5% noise (Fig. 14(c)). Moreover, increased Te vacancy density reduced phase transition energy, enabling ultrafast switching speeds (SET ~ 5 ns, RESET ~ 10 ns). In addition, controlled Ar/O_2 plasma treatment selectively sputters sulfur atoms in MoS_2, creating V_S to enhance conductivity. Figure 14(d) shows a visual representation of the Ar plasma treatment. Low-power plasma enables precise vacancy concentration tuning, while excessive power induces material degradation [202]. Optimized MoS_2 memristors exhibited a switching ratio of 10^4 and improved endurance. In artificial neural network (ANN) simulations shown in Fig. 14(e) using MNIST datasets, the system achieved 97% recognition accuracy (Fig. 14(f)). Oxygen plasma irradiation further constructed $MoS_{2-x}O_x$ gradient resistive layers, achieving superior conductance modulation (window: 1.56 μs) and 90% accuracy in Neurosim simulations.

Plasma-assisted deposition and heterostructure engineering. PECVD with oxygen plasma activation enables large-area MoS_2 growth on flexible substrates, circumventing mechanical transfer-induced defects (cracks, wrinkles, residues) [203]. The low-temperature vulcanization process forms MoS_2 nanocrystals, which interconnect to create a polycrystalline boundary structure. Due to the presence of numerous defects and vacancies, the energy state of grain boundaries differs from that within the grains, making them low-energy transport pathways for charged particles. The continuous accumulation of charged particles along grain boundary channels can lead to the formation of conductive filaments [204, 205]. The resulting devices demonstrated exceptional performance: switching ratio (10^5), low off-state current (10^{-9} A), and stable cycling (> 350 cycles).

Plasma-etched core–shell heterostructures. Inductively coupled plasma reactive ion etching (ICP-RIE) with SF_6/Ar plasma produced MoO_2-MoS_2 core–shell heterostructures [206]. As shown in Fig. 14(g), the MoO_2 core serves dual functions as conductive pathway and bottom electrode, while the partially exposed MoS_2 shell optimizes interfacial properties. These memristors achieved record performance: switching ratio (10^7) and ultralow operating power (50 pW/operation) demonstrating exceptional low-power potential (Figs. 14(h) and 14(i)).

4.3.4 Plasma treatment for improvement of electrical transport properties

Plasma treatment can significantly alter the electronic structure and

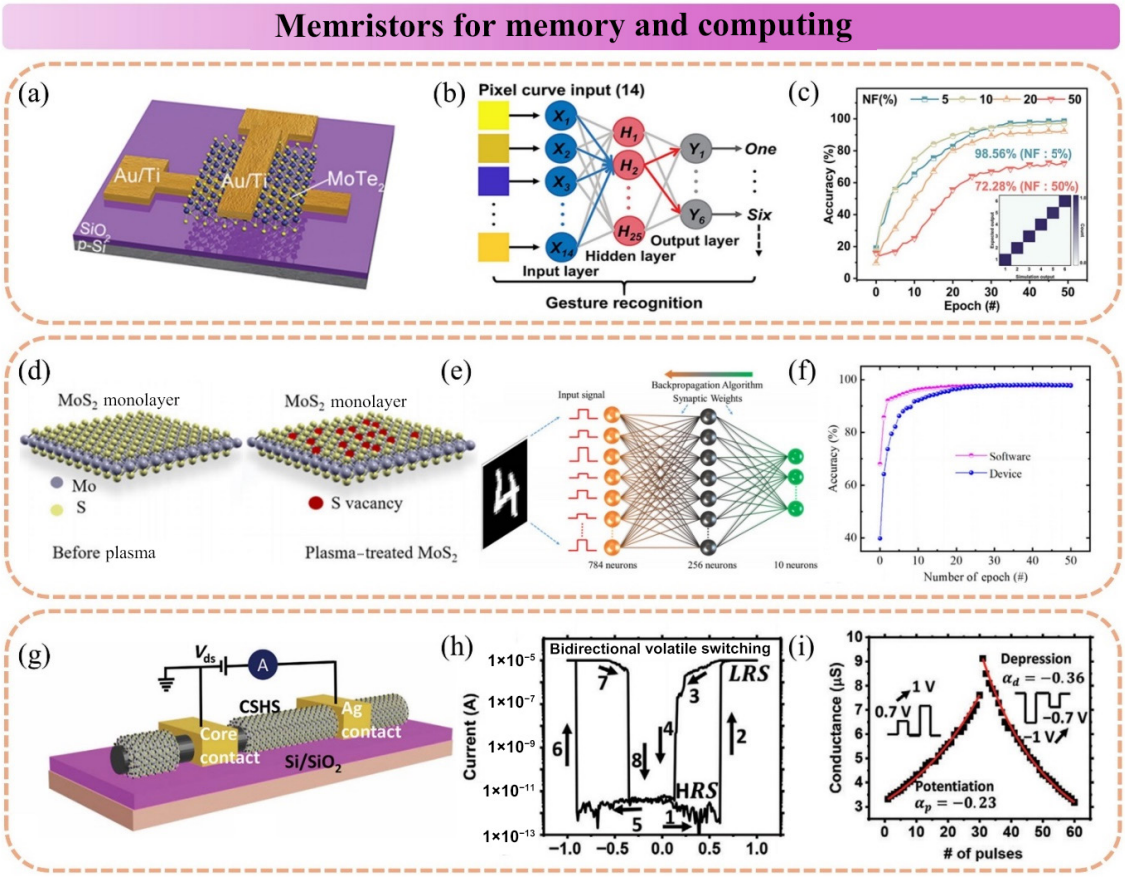


Figure 14 Plasma-engineered 2D memristive devices for neuromorphic computing. (a) Device schematic of $MoTe_2$-based memristor with Ar plasma-induced Te vacancies enabling 2H to 1T′ phase switching. Reproduced with permission from Ref. [34], © The Royal Society of Chemistry 2022. (b) CNN-based gesture recognition setup for artificial synapse evaluation. (c) Recognition accuracy under varying noise levels, reaching 98.56% at 5% noise after training. Reproduced with permission from Ref. [170], © IEEE 2023. (d) Illustration of Ar plasma treatment on MoS_2 generating sulfur vacancies. (e) Simulation of MNIST dataset using optimized MoS_2 memristors showing 97% accuracy. (f) Endurance and switching ratio improvements via plasma-tuned vacancy concentration. Reproduced with permission from Ref. [207], © Rajput, M. et al. 2024. (g) Cross-sectional schematic of MoO_2/MoS_2 core shell heterostructure prepared by SF_6/Ar ICP-RIE. (h) Electrical performance: switching ratio of 10^7 and ultralow power consumption (50 pW/operation). (i) Cycle endurance and conductance modulation behavior of the core-shell memristive system. Reproduced with permission from Ref. [206], © Wiley-VCH GmbH 2023.

properties of TMDs, including but not limited to conductivity, charge carrier density, charge carrier mobility, subthreshold swing, threshold voltage, work function, and bandgap [30, 208]. Through doping, defect engineering, etching, and other methods, plasma induces various physical or chemical reactions on TMDs, such as ion implantation, atomic substitution, atomic defect formation, atomic adsorption, oxidation, and reduction, thereby regulating the electrical properties of these materials [209, 210].

Under the influence of reactive plasma (e.g., oxygen), TMDs are prone to oxidation, forming WO_x/MoO_x with high work function or oxygen-containing chemical bonds, leading to p-type doping [211, 212]. This oxidation reaction, in turn, modifies the charge carrier density, mobility, subthreshold swing, and threshold voltage of the TMDs. Additionally, plasma treatment enables the uniform formation of an oxide layer on the TMDs surface. By precisely controlling parameters such as flow rate, pressure, power, and treatment time, the oxidation rate can be finely tuned to achieve the desired oxide layer thickness and quality [213]. As a result, the electrical properties of TMDs change significantly with varying oxygen plasma treatment times. As shown in Fig. 15(a), the hole current increases dramatically as the oxygen plasma treatment time increases from 60 to 480 s, with the current density of the device treated for 480 s being five orders of magnitude higher than that of the untreated device. Additionally, the output characteristics of the prepared devices transition to ohmic characteristics after oxidation. The drastic change in current on/off ratio, exceeding 10^6, and the linear increase in on-state current at different oxidation times indicate an increase in carrier concentration through oxidation. Furthermore, the field-effect mobility increases with longer oxidation times, reaching a peak of 200 $cm^2 \cdot V^{-1} \cdot s^{-1}$, primarily due to the increase in transconductance.

Oxygen and nitrogen plasma treatment could repair the intrinsic sulfur vacancy defects in TMDs [214, 215], suppressing electron capture, which results in band structure change [72] and even a transition of the carrier transport mechanism from hopping conduction to band conduction, leading to a metal-insulator transition (MIT). Lee et al. used oxygen plasma treatment with Al_2O_3 as a barrier layer to repair V_S in MoS_2 and protect the channel from damage [79]. As shown in Fig. 15(b), MIT occurred at an electron concentration of 5.7×10^{12} cm^{-2}, indicating an improvement in channel quality. Due to the reduction of V_S as local states after oxygen plasma treatment, the activation energy (E_a) decreased at all gate voltages (V_G). Jiang et al. effectively repaired the intrinsic sulfur vacancies through nitrogen plasma to enhance the

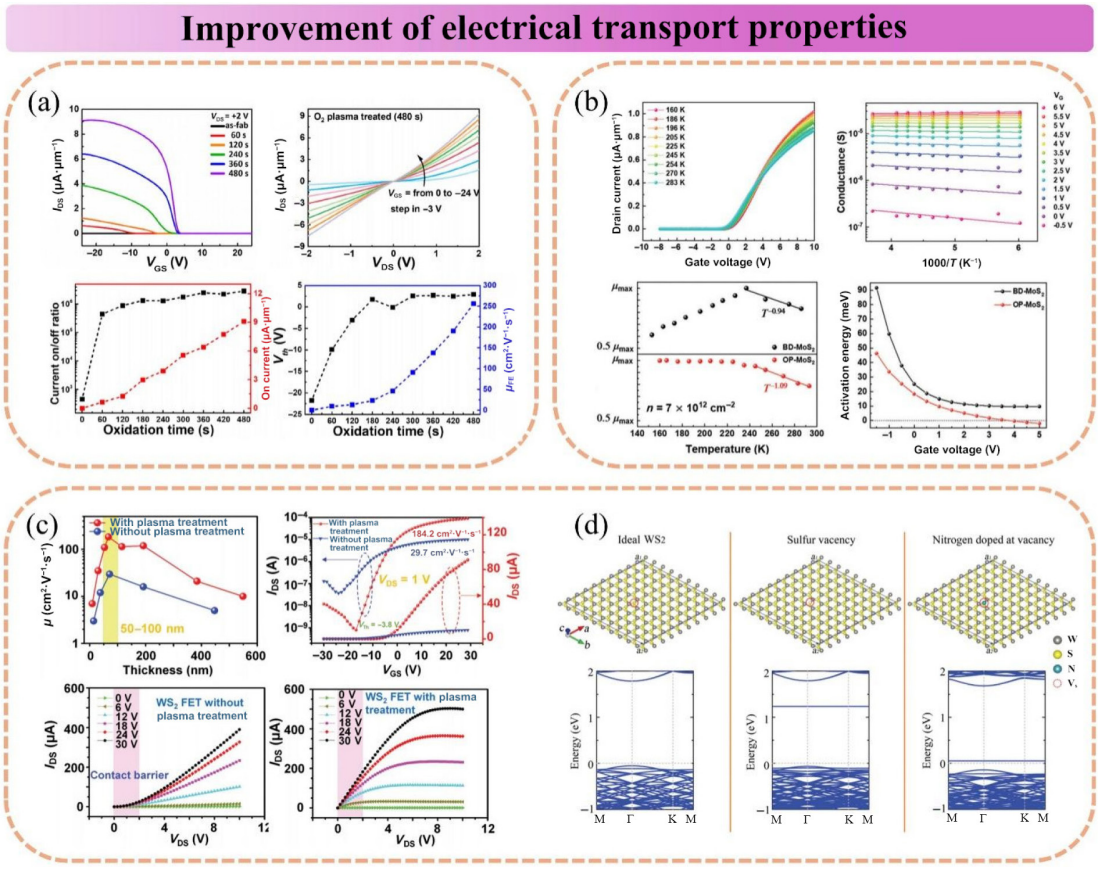


Figure 15 Improvement of electrical transport properties of TMDs. (a) Electrical characteristics of WSe_2 FET with different oxygen plasma treatment time. Reproduced with permission from Ref. [213], © American Chemical Society 2023. (b) Temperature-dependent electrical characterizations of MoS_2 FET after oxygen plasma. Reproduced with permission from Ref. [79], © Wiley-VCH GmbH 2023. (c) The thickness-dependent field-effect mobilities transfer characteristics and corresponding output characteristics of WS_2 FETs with or without nitrogen plasma doping treatment. (d) Schematic illustrations of WS_2 band structures after nitrogen plasma treatment. Reproduced with permission from Ref. [72], © WILEY-VCH Verlag GmbH & Co. KGaA, Weinheim 2019.

performance of WS_2 FET. As demonstrated in Fig. 15(c), the WS_2 device achieves an electron mobility of up to 184.2 $cm^2 \cdot V^{-1} \cdot s^{-1}$ with a threshold voltage as low as 3.8 V. DFT calculations (as shown in Fig. 15(d)) show that nitrogen plasma doping and defect repair reduce the effective mass of electrons, providing an effective way to improve the carrier mobility of WS_2.

5 Conclusion and outlook

TMDs have emerged as a class of highly promising materials for next-generation electronics and optoelectronics, owing to their exceptional electronic, optical, and structural properties. However, translating these advantages into practical, high-performance devices requires overcoming significant challenges in material synthesis, property modulation, and device integration. In this review, we have systematically summarized the role of plasma-based technologies across the entire TMDs engineering workflow from scalable, low-temperature synthesis and precise doping strategies to high-resolution patterning and functional device fabrication. Through diverse modalities such as plasma-assisted growth, etching, doping, and defect engineering, plasma treatment offers a versatile and controllable platform to tailor the structure, composition, and performance of TMDs and has become a critical technology for the practical implementation of 2D materials.

As the field of two-dimensional TMDs matures, plasma-based technologies are expected to play an increasingly central role in enabling scalable, tunable, and multifunctional device integration. Despite the remarkable progress in proof-of-concept demonstrations, significant challenges remain in standardization, spatial control, intelligent reconfigurability, and heterostructure integration. To unlock the full potential of plasma-enabled 2D systems, we outline four synergistic and forward-looking directions, as shown in Fig. 16.

5.1 Standardized and scalable plasma platforms: Toward reproducible manufacturing

Current plasma treatment of TMDs suffers from a lack of standardization, with wide variability in plasma parameters, material responses, and characterization protocols. To transition from laboratory-scale demonstrations to industrial-scale production, it is imperative to establish reproducible processing frameworks that quantitatively correlate plasma inputs (e.g., power, frequency, gas chemistry) with outputs (e.g., doping profiles, defect densities, etching kinetics). Developing benchmark datasets, shared protocols, and cross-laboratory calibration standards will be crucial for ensuring compatibility with CMOS process flows and device reliability. Concurrently, remote plasma sources that spatially decouple the excitation and reaction zones, offering high-density, low-energy neutral species, represent a promising route for substrate-compatible, low-temperature synthesis, minimizing ion-induced damage and enabling wafer-scale growth.

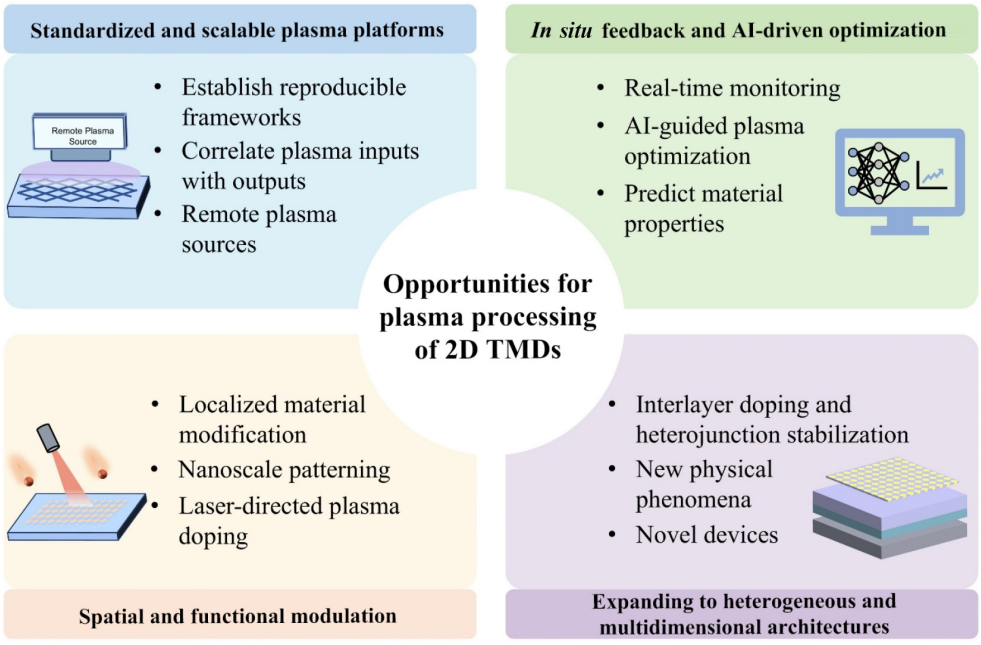


Figure 16 The future development trends.

5.2 *In situ* feedback and artificial intelligence (AI)-driven optimization: Enhancing precision and predictability

Process optimization requires real-time, non-destructive monitoring systems to guide growth dynamics and plasma-material interactions. Optical diagnostics such as laser reflectance interferometry, Raman spectroscopy, and spectroscopic ellipsometry can provide dynamic feedback on film thickness, crystallinity, and interface evolution. Complementary gas-phase analysis via optical emission spectroscopy (OES) and quadrupole mass spectrometry (QMS) enables monitoring of plasma species, precursor dissociation, and reaction byproducts. To navigate the high-dimensional plasma parameter space, AI and machine learning (ML) approaches, particularly neural networks and regression models, offer transformative capabilities. By learning from experimental or simulated datasets, these models can predict material properties from process parameters and enable inverse design workflows for target-driven process discovery. To implement AI-driven plasma optimization, deep neural networks such as 3D-CNNs can be trained to quantitatively map plasma parameters (e.g., power, pressure, gas composition) to material properties (e.g., carrier mobility, contact resistance). The use of Bayesian optimization enables convergence to optimal process parameters within 10–15 experimental iterations, significantly accelerating development. Integration with *in situ* metrology (e.g., optical emission spectroscopy) supports real-time data collection and feedback control for precision tuning of plasma conditions. Integration of AI-guided plasma optimization with post-treatment methods such as thermal annealing and passivation may further stabilize electronic and optical properties under real-world conditions.

5.3 Spatial and functional modulation: Enabling fine-tuned material control

Beyond global modulation, precise control over spatially resolved doping and defect engineering is vital for high-integration-density applications. With the continuous improvement of device miniaturization and functional integration, the potential of plasma treatment in achieving localized material modification has become increasingly prominent. Compared with the traditional full-area regulation method, the spatially selective modulation technology based on plasma can achieve submicron or even nanometer-level precise shaping of doping behavior, defect distribution and electronic structure in two-dimensional material systems. Developing techniques such as laser-directed plasma doping, electric field-assisted localization, and hybrid optical, plasma lithography will allow for deterministic patterning of electrical and optical functionalities across 2D architectures. These methods are expected to pave the way for the controlled fabrication of in-plane p-n junctions, spatial heterogeneity in carrier types, and multi-level logic units within a single crystal domain.

5.4 Expanding to heterogeneous and multidimensional architectures: Extending functional horizons

The unique layered structure of two-dimensional materials makes them naturally suitable for constructing heterogeneous and multi-dimensional composite systems. Based on the increasingly mature processing technology of single-layer and few-layer materials, the application of plasma technology is gradually expanding to more complex structural dimensions. With increasing maturity in monolayer and few-layer processing, the application of plasma techniques to more complex systems such as vertically stacked heterostructures, hybrid organic–inorganic interfaces, and multi-functional 2D composites will become increasingly important. Plasma processes tailored for interfacial modulation, interlayer doping, and heterojunction stabilization can unlock new physical phenomena, including excitonic coupling, charge tunneling, and interfacial ferroelectricity. These capabilities are expected to support novel devices such as mixed-dimensional transistors, broadband photodetectors, and artificial synapses.

The future development of plasma-enabled TMDs depends on the coordinated breakthroughs in standardized processes,

intelligent control, spatial programmability, and multi-dimensional integration. Through the deep integration of the above technical routes, plasma engineering will promote the evolution of TMDs from single-function devices to adaptive, highly integrated, multi-physical field coupled intelligent systems, providing disruptive solutions for post-Moore electronics, efficient photoelectric conversion, and neuromorphic computing, and ultimately achieving a leap from "material modification" to "system integration".

Data availability

All data needed to support the conclusions in the paper are presented in the manuscript. Additional data related to this paper may be requested from the corresponding author upon request.

Acknowledgements

This work is supported by the National Science Foundation of China (Nos. 62304151, 62204170, and 62474124), the Natural Science Foundation of Tianjin (No. 24JCQNJC00520), the China Postdoctoral Science Foundation (No. 2023M742585), the Open Project of State Key Laboratory of Transducer Technology (No. SKT2208), the open research of Songshan Lake Materials Laboratory (No. 2023SLABFK07), and the State Key Laboratory of Fluid Power and Mechatronic Systems (No. GZKF-202327).

Declaration of competing interest

All the contributing authors report no conflict of interests in this work.

Author contribution statement

Y. X.: Writing manuscript, revising manuscript. A. Z.: Revising manuscript. G. J. W.: Revising manuscript. S. D. H.: Revising manuscript. P. J. N.: Project administration, funding acquisition. E. X. W.: Project administration, funding acquisition. All the authors have approved the final manuscript.

Use of AI statement

None.

References

[1] Moon, D.; Lee, W.; Lim, C.; Kim, J.; Kim, J.; Jung, Y.; Choi, H. Y.; Choi, W. S.; Kim, H.; Baek, J. H. et al. Hypotaxy of wafer-scale single-crystal transition metal dichalcogenides. *Nature* **2025**, *638*, 957–964.

[2] Kumar, R.; Shringi, A. K.; Wood, H. J.; Asuo, I. M.; Oturak, S.; Sanchez, D. E.; Sharma, T. S. K.; Chaurasiya, R.; Mishra, A.; Choi, W. M. et al. Substitutional doping of 2D transition metal dichalcogenides for device applications: Current status, challenges and prospects. *Mater. Sci. Eng.: R: Rep.* **2025**, *163*, 100946.

[3] Wu, R. X.; Zhang, H. M.; Ma, H. F.; Zhao, B.; Li, W.; Chen, Y.; Liu, J. T.; Liang, J. Y.; Qin, Q. Y.; Qi, W. X. et al. Synthesis, modulation, and application of two-dimensional TMD heterostructures. *Chem. Rev.* **2024**, *124*, 10112–10191.

[4] Li, W. W.; Kong, L. Y.; Xu, M. Z.; Gao, J. W.; Luo, L.; Li, Y. Z.; Wang, K. X.; Zhou, Y. L.; Li, L.; Wei, Y. et al. Microsecond-scale transient thermal sensing enabled by flexible Mo_{1-x} W_xS_2 alloys. *Research* **2024**, *7*, 0452.

[5] Xiong, Y. H.; Xu, D.; Zou, Y. S.; Xu, L. L.; Yan, Y. J.; Wu, J. H.; Qian, C.; Song, X. F.; Qu, K. R.; Zhao, T. et al. Vapour-liquid-solid-solid growth of two-dimensional non-layered β-Bi_2O_3 crystals with high hole mobility. *Nat. Mater.* **2025**, *24*, 688–697.

[6] Liu, X.; Deng, C. Y.; Wei, H.; Fang, M. K.; Yan, B.; Zhu, T.; Luo, S. F.; Peng, G.; Cai, W. W.; Long, M. S. et al. High-sensitive uncooled mid-wave infrared photodetector based on $PtSe_2$/$MoTe_2$ heterojunction with fast speed. *Adv. Funct. Mater.*, in press, https://doi.org/10.1002/adfm.202423102.

[7] Jang, J.; Hong, J. P.; Kim, S. J.; Ahn, J.; Yu, B. S.; Han, J.; Lee, K.; Ha, A.; Yoon, E.; Kim, W. et al. Conductive-bridge interlayer contacts for two-dimensional optoelectronic devices. *Nat. Electron.* **2025**, *8*, 298–308.

[8] Kim, C.; Kim, M.; Kim, S.; Kang, M. J.; Choi, M. S.; Kim, H. U. Plasma and gas-based semiconductor technologies for 2D materials with computational simulation & electronic applications. *Adv. Electron. Mater.* **2024**, *10*, 2300835.

[9] Choi, S. H.; Yun, S. J.; Won, Y. S.; Oh, C. S.; Kim, S. M.; Kim, K. K.; Lee, Y. H. Large-scale synthesis of graphene and other 2D materials towards industrialization. *Nat. Commun.* **2022**, *13*, 1484.

[10] Xu, M. Z.; Ji, H. J.; Zhang, M. W.; Zheng, L.; Li, W. W.; Luo, L.; Chen, M. D.; Liu, Z.; Gan, X. T.; Wang, X. W. et al. CVD synthesis of twisted bilayer WS_2 with tunable second harmonic generation. *Adv. Mater.* **2024**, *36*, 2313638.

[11] Xu, M. Z.; Ji, H. J.; Zheng, L.; Li, W. W.; Wang, J.; Wang, H. X.; Luo, L.; Lu, Q. B.; Gan, X. T.; Liu, Z. et al. Reconfiguring nucleation for CVD growth of twisted bilayer MoS_2 with a wide range of twist angles. *Nat. Commun.* **2024**, *15*, 562.

[12] Kozhakhmetov, A.; Stolz, S.; Tan, A. M. Z.; Pendurthi, R.; Bachu, S.; Turker, F.; Alem, N.; Kachian, J.; Das, S.; Hennig, R. G. et al. Controllable p-type doping of 2D WSe_2 via vanadium substitution. *Adv. Funct. Mater.* **2021**, *31*, 2105252.

[13] Lan, H. Y.; Lin, C. P.; Liu, L. N.; Cai, J.; Sun, Z.; Wu, P.; Tan, Y. Q.; Yang, S. H.; Hou, T. H.; Appenzeller, J. et al. Uncovering the doping mechanism of nitric oxide in high-performance P-type WSe_2 transistors. *Nat. Commun.* **2025**, *16*, 4160.

[14] Cheng, Z. F.; He, S. D.; Zhang, S. M.; Duan, S. J.; Wang, M.; Liu, Z. Y.; Zhang, R.; Qiang, W. Y.; Zhang, X. D.; Xia, M. G. Regulating the conductance of tungsten diselenide by oxygen plasma and improving its electrical stability by encapsulation. *Nano Res.* **2024**, *17*, 3253–3260.

[15] Zhang, Y.; Chen, P. A.; Lu, Z. Y.; Liu, Y.; Wei, H.; Xia, J. N.; Ding, J. Q.; Gong, Z. Q.; Peng, C. Y.; Shi, W. P. et al. Template-assisted dry transfer doping of two-dimensional semiconductors. *Nano Lett.* **2025**, *25*, 3265–3272.

[16] Dutta, R.; Bala, A.; Sen, A.; Spinazze, M. R.; Park, H.; Choi, W.; Yoon, Y.; Kim, S. Optical enhancement of indirect bandgap 2D transition metal dichalcogenides for multi-functional optoelectronic sensors. *Adv. Mater.* **2023**, *35*, 2303272.

[17] Sovizi, S.; Angizi, S.; Ahmad Alem, S. A.; Goodarzi, R.; Taji Boyuk, M. R. R.; Ghanbari, H.; Szoszkiewicz, R.; Simchi, A.; Kruse, P. Plasma processing and treatment of 2D transition metal dichalcogenides: Tuning properties and defect engineering. *Chem. Rev.* **2023**, *123*, 13869–13951.

[18] Feng, X. L.; Tao, H.; Yang, S. J.; Liu, C.; Wei, C. H.; Wang, Y. K.; Zhao, H. Y.; Yao, S. H.; Cheng, Z. X. Recent advances of plasma technology applications in 2D materials and electronics. *Adv. Mater. Technol.*, in press, https://doi.org/10.1002/admt.202402207.

[19] Sivan, M.; Li, Y. D.; Veluri, H.; Zhao, Y. S.; Tang, B. S.; Wang, X. H.; Zamburg, E.; Leong, J. F.; Niu, J. X.; Chand, U. et al. All WSe_2 1T1R resistive RAM cell for future monolithic 3D embedded memory integration. *Nat. Commun.* **2019**, *10*, 5201.

[20] Wu, Z. H.; Lyu, Y. X.; Zhang, Y.; Ding, R.; Zheng, B. N.; Yang, Z. B.; Lau, S. P.; Chen, X. H.; Hao, J. H. Large-scale growth of few-layer two-dimensional black phosphorus. *Nat. Mater.* **2021**, *20*, 1203–1209.

[21] Jiang, H. J.; Li, L.; Wu, Y.; Duan, R. H.; Yi, K. Y.; Wu, L. S.; Zhu,

C.; Luo, L.; Xu, M. Z.; Zheng, L. et al. Vapor deposition of bilayer 3R MoS_2 with room-temperature ferroelectricity. *Adv. Mater.* **2024**, *36*, 2400670.

[22] Fu, Q.; Wang, S. X.; Zhou, B. J.; Xia, W. Q.; Liu, X. Y.; Han, X.; Duan, Z. X.; Liu, T. Q.; Sun, X. D.; Yuan, X. Y. et al. Defect-mediated efficient and tunable emission in van der waals integrated light sources at room temperature. *Adv. Funct. Mater.* **2025**, *35*, 2414062.

[23] Loh, L.; Zhang, Z. P.; Bosman, M.; Eda, G. Substitutional doping in 2D transition metal dichalcogenides. *Nano Res.* **2021**, *14*, 1668–1681.

[24] Shan, Y. F.; Yin, Z. W.; Zhu, J. Q.; Li, X.; Dou, W.; Wang, Y.; Liu, C. X.; Deng, H. Y.; Dai, N. Few-layered MoS_2 based vertical van der Waals p–n homojunction by highly-efficient N_2 plasma implantation. *Adv. Electron. Mater.* **2022**, *8*, 2200299.

[25] Zhang, J. Y.; Zheng, J. X.; Wang, Z. Plasma-assisted synthesis of 2D MoS_2 nanosheets with tunable sulfur defects for highly efficient nitrogen reduction reaction. *Chem. Eng. Sci.* **2023**, *280*, 119076.

[26] Kang, M. G.; Hong, W.; Lee, I.; Park, S.; Park, C.; Bae, S.; Lim, H.; Choi, S. Y. Tunable doping strategy for few-layer MoS_2 field-effect transistors via NH_3 plasma treatment. *ACS Appl. Mater. Interfaces* **2024**, *16*, 43849–43859.

[27] Tan, P.; Ding, K. X.; Zhang, X. M.; Ni, Z. H.; Ostrikov, K.; Gu, X. F.; Nan, H. Y.; Xiao, S. Q. Bidirectional doping of two-dimensional thin-layer transition metal dichalcogenides using soft ammonia plasma. *Nanoscale* **2021**, *13*, 15278–15284.

[28] Li, M. H.; Li, L.; Fan, Y. X.; Jiao, F.; Geng, D. C.; Hu, W. P. From top to down-recent advances in etching of 2D materials. *Adv. Mater. Interfaces* **2022**, *9*, 2201334.

[29] Zhu, K. C.; Pazos, S.; Aguirre, F.; Shen, Y. Q.; Yuan, Y.; Zheng, W. W.; Alharbi, O.; Villena, M. A.; Fang, B.; Li, X. Y. et al. Hybrid 2D-CMOS microchips for memristive applications. *Nature* **2023**, *618*, 57–62.

[30] Wang, S. B.; Zeng, X. B.; Zhou, Y. F.; Lu, J. J.; Hu, Y. S.; Wang, W. Z.; Wang, J. H.; Xiao, Y. H.; Wang, X. Y.; Chen, D. et al. High-performance MoS_2 complementary inverter prepared by oxygen plasma doping. *ACS Appl. Electron. Mater.* **2022**, *4*, 955–963.

[31] Choi, D.; Kim, D.; Jo, Y.; Kim, J. H.; Yoon, E.; Lee, H. C.; Kim, T. Directly grown Te nanowire electrodes and soft plasma etching for high-performance $MoTe_2$ field-effect transistors. *Appl. Surf. Sci.* **2021**, *565*, 150521.

[32] Chee, S. S.; Ham, M. H. Low-damaged layer-by-layer etching of large-area molybdenum disulfide films via mild plasma treatment. *Adv. Mater. Interfaces* **2020**, *7*, 2000762.

[33] Price, K. M.; Schauble, K. E.; McGuire, F. A.; Farmer, D. B.; Franklin, A. D. Uniform growth of sub-5-nanometer high-κ dielectrics on MoS_2 using plasma-enhanced atomic layer deposition. *ACS Appl. Mater. Interfaces* **2017**, *9*, 23072–23080.

[34] He, H. K.; Jiang, Y. B.; Yu, J.; Yang, Z. Y.; Li, C. F.; Wang, T. Z.; Dong, D. Q.; Zhuge, F. W.; Xu, M.; Hu, Z. Y. et al. Ultrafast and stable phase transition realized in $MoTe_2$-based memristive devices. *Mater. Horiz.* **2022**, *9*, 1036–1044.

[35] Wu, J. H.; Li, S. S.; Wang, X. M.; Huang, Y.; Huang, Y. F.; Chen, H. J.; Chen, J.; She, J. C.; Deng, S. Z. Plasma treatment for achieving oxygen substitution in layered MoS_2 and the room-temperature mid-infrared (10 μm) photoresponse. *ACS Appl. Mater. Interfaces* **2023**, *15*, 58556–58565.

[36] Afzal, A. M.; Iqbal, M. Z.; Dastgeer, G.; Nazir, G.; Mumtaz, S.; Usman, M.; Eom, J. WS_2/GeSe/WS_2 bipolar transistor-based chemical sensor with fast response and recovery times. *ACS Appl. Mater. Interfaces* **2020**, *12*, 39524–39532.

[37] Youn, H. Y.; Choi, T. Y.; Shim, J.; Park, S. Y.; Kwon, M. K.; Kim, S.; Kim, H. K. Soft sputtering of large-area 2D MoS_2 layers using isolated plasma soft deposition for humidity sensors. *Adv. Mater.* **2025**, *37*, 2414800.

[38] Sino, P. A. L.; Lin, T. C.; Wani, S.; Lee, L.; Chen, C. T.; Liu, M. J.; Kuo, Y. Z.; Rehman, B.; Tuyen Le, K.; Wu, J. M. et al. Controllable structure-engineered janus and alloy polymorphic monolayer transition metal dichalcogenides by plasma-assisted selenization process toward high-yield and wafer-scale production. *Mater. Today* **2023**, *69*, 97–106.

[39] Yao, C. J.; Ren, W. Q.; Raju, T. D.; Lee, H. J.; Khot, A. C.; Nirmal, K. A.; Kim, T. G. High-performance blue TADF OLED using two-step heat plasma-treated $MoTe_2$ as a hole-injection layer. *J. Mater. Sci. Technol.* **2024**, *198*, 200–207.

[40] Kim, Y.; Kwon, S.; Seo, E. J.; Nam, J. H.; Jang, H. Y.; Kwon, S. H.; Kwon, J. D.; Kim, D. W.; Cho, B. Facile fabrication of a two-dimensional TMD/Si heterojunction photodiode by atmospheric-pressure plasma-enhanced chemical vapor deposition. *ACS Appl. Mater. Interfaces* **2018**, *10*, 36136–36143.

[41] Seok, H.; Shin, D.; Kim, H. U.; Kim, T. Flexible sensor platform: Nano-grain of 2D heterostructure by cold-plasma. In *Proceedings 2022 IEEE International Symposium on Medical Measurements and Applications*, Messina, Italy, 2022, pp 1–6.

[42] Kim, H. U.; Kim, M.; Seok, H.; Park, K. Y.; Moon, J. Y.; Park, J.; An, B. S.; Jung, H. J.; Dravid, V. P.; Whang, D. et al. Realization of wafer-scale 1T-MoS_2 film for efficient hydrogen evolution reaction. *ChemSusChem* **2021**, *14*, 1344–1350.

[43] Seok, H.; Megra, Y. T.; Kanade, C. K.; Cho, J.; Kanade, V. K.; Kim, M.; Lee, I.; Yoo, P. J.; Kim, H. U.; Suk, J. W. et al. Low-temperature synthesis of wafer-scale MoS_2-WS_2 vertical heterostructures by single-step penetrative plasma sulfurization. *ACS Nano* **2021**, *15*, 707–718.

[44] Trivedi, D. B.; Turgut, G.; Qin, Y.; Sayyad, M. Y.; Hajra, D.; Howell, M.; Liu, L.; Yang, S. J.; Patoary, N. H.; Li, H. et al. Room-temperature synthesis of 2D janus crystals and their heterostructures. *Adv. Mater.* **2020**, *32*, 2006320.

[45] Guan, Y. W.; Li, X.; Yang, H. M.; Yang, Y. Z.; Du, Z. M.; Hua, Z.; Wang, X. X.; Zeng, D. W. Pore-edge high active sites of 2D WO_3 nanosheets enhancing acetone sensing performance. *Talanta* **2025**, *282*, 127003.

[46] Seo, D. B.; Yoo, S.; Dongquoc, V.; Trung, T. N.; Kim, E. T. Facile synthesis and efficient photoelectrochemical reaction of WO_3/WS_2 core@shell nanorods utilizing $WO_3 \cdot 0.33H_2O$ phase. *J. Alloy. Compd.* **2021**, *888*, 161587.

[47] Kumar, P.; Singh, M.; Reddy, G. B. Core–shell WO_3-WS_2 nanostructured thin films via plasma assisted sublimation and sulfurization. *ACS Appl. Nano Mater.* **2019**, *2*, 1691–1703.

[48] Kim, H. U.; Kanade, V.; Kim, M.; Kim, K. S.; An, B. S.; Seok, H.; Yoo, H.; Chaney, L. E.; Kim, S. I.; Yang, C. W. et al. Wafer-scale and low-temperature growth of 1T-WS_2 film for efficient and stable hydrogen evolution reaction. *Small* **2020**, *16*, 1905000.

[49] Zhang, K. N.; Zhang, T. Y.; You, J. W.; Zheng, X. D.; Zhao, M.; Zhang, L. J.; Kong, J.; Luo, Z. T.; Huang, S. M. Low-temperature vapor-phase growth of 2D metal chalcogenides. *Small* **2024**, *20*, 2307587.

[50] Kim, H. U.; Koyappayil, A.; Seok, H.; Aydin, K.; Kim, C.; Park, K. Y.; Jeon, N.; Kang, W. S.; Lee, M. H.; Kim, T. Concurrent and selective determination of dopamine and serotonin with flexible WS_2/graphene/polyimide electrode using cold plasma. *Small* **2021**, *17*, 2102757.

[51] Bala, A.; Liu, N.; Sen, A.; Cho, Y.; Pujar, P.; So, B.; Kim, S. Low-temperature plasma-assisted growth of large-area MoS_2 for transparent phototransistors. *Adv. Funct. Mater.* **2022**, *32*, 2205106.

[52] Seok, H.; Kim, M.; Cho, J.; Kim, E.; Son, S.; Kim, K. W.; Kim, J. K.; Yoo, P. J.; Kim, M.; Kim, H. U. et al. Tailoring polymorphic heterostructures of MoS_2-WS_2 (1T/1T, 2H/2H) for efficient hydrogen evolution reaction. *ACS Sustain. Chem. Eng.* **2023**, *11*, 568–577.

[53] Liu, M. J.; Lan, W. J.; Huang, C. S.; Chen, C. Z.; Cyu, R. H.; Sino, P. A. L.; Yang, Y. L.; Chiu, P. W.; Chuang, F. C.; Shen, C. H. et al. High-performance monolithic 3D integrated complementary

inverters based on monolayer n-MoS_2 and p-WSe_2. *Small* **2024**, *20*, 2307728.

[54] Pan, Y.; Jian, T.; Gu, P. F.; Song, Y. W.; Wang, Q.; Han, B.; Ran, Y. Q.; Pan, Z. M.; Li, Y. P.; Xu, W. J. et al. Precise p-type and n-type doping of two-dimensional semiconductors for monolithic integrated circuits. *Nat. Commun.* **2024**, *15*, 9631.

[55] Das, M.; Sen, D.; Sakib, N. U.; Ravichandran, H.; Sun, Y. W.; Zhang, Z. Y.; Ghosh, S.; Venkatram, P.; Subbulakshmi Radhakrishnan, S.; Sredenschek, A. et al. High-performance p-type field-effect transistors using substitutional doping and thickness control of two-dimensional materials. *Nat. Electron.* **2025**, *8*, 24–35.

[56] Wang, Y.; Sarkar, S.; Yan, H.; Chhowalla, M. Critical challenges in the development of electronics based on two-dimensional transition metal dichalcogenides. *Nat. Electron.* **2024**, *7*, 638–645.

[57] Song, J.; Lee, S.; Seok, Y.; Ko, Y.; Jang, H.; Watanabe, K.; Taniguchi, T.; Lee, K. Drain-induced multifunctional ambipolar electronics based on junctionless MoS_2. *ACS Nano* **2024**, *18*, 4320–4328.

[58] Fukui, T.; Nishimura, T.; Miyata, Y.; Ueno, K.; Taniguchi, T.; Watanabe, K.; Nagashio, K. Single-gate MoS_2 tunnel FET with a thickness-modulated homojunction. *ACS Appl. Mater. Interfaces* **2024**, *16*, 8993–9001.

[59] He, Q. Y.; Liu, Y.; Tan, C. L.; Zhai, W.; Nam, G. H.; Zhang, H. Quest for p-type two-dimensional semiconductors. *ACS Nano* **2019**, *13*, 12294–12300.

[60] He, H. N.; Zhang, H. H.; Huang, D.; Kuang, W.; Li, X. L.; Hao, J. N.; Guo, Z. P.; Zhang, C. H. Harnessing plasma-assisted doping engineering to stabilize metallic phase $MoSe_2$ for fast and durable sodium-ion storage. *Adv. Mater.* **2022**, *34*, 2200397.

[61] Sun, Y.; Zang, Y. P.; Tian, W. Z.; Yu, X. J.; Qi, J. Z.; Chen, L. W.; Liu, X.; Qiu, H. B. Plasma-induced large-area N, Pt-doping and phase engineering of MoS_2 nanosheets for alkaline hydrogen evolution. *Energy Environ. Sci.* **2022**, *15*, 1201–1210.

[62] Kuang, Y. B.; Qiao, W.; Wang, S. L.; Yang, F. L.; Feng, L. G. Doping and interfacial engineering of $MoSe_2$ nanosheets by NH_3 plasma promoted Pt for methanol electrolysis. *ACS Mater. Lett.* **2024**, *6*, 1722–1731.

[63] Williams, J. S. Ion implantation of semiconductors. *Mater. Sci. Eng.: A* **1998**, *253*, 8–15.

[64] Beaudette, C. A.; Held, J. T.; Mkhoyan, K. A.; Kortshagen, U. R. Nonthermal plasma-enhanced chemical vapor deposition of two-dimensional molybdenum disulfide. *ACS Omega* **2020**, *5*, 21853–21861.

[65] Im, H. H.; Lee, D.; Lee, G.; Kim, H. Y.; Kim, J. Self-aligned contact doping of WSe_2 metal-insulator-semiconductor field-effect transistors using hydrogen silsesquioxane. *ACS Appl. Electron. Mater.* **2023**, *5*, 2394–2400.

[66] Pang, C. S.; Hung, T. Y. T.; Khosravi, A.; Addou, R.; Wang, Q. X.; Kim, M. J.; Wallace, R. M.; Chen, Z. C. Atomically controlled tunable doping in high-performance WSe_2 devices. *Adv. Electron. Mater.* **2020**, *6*, 1901304.

[67] Li, T. X.; Miao, J. S.; Fu, X.; Song, B.; Cai, B.; Ge, X.; Zhou, X. H.; Zhou, P.; Wang, X. R.; Jariwala, D. et al. Reconfigurable, non-volatile neuromorphic photovoltaics. *Nat. Nanotechnol.* **2023**, *18*, 1303–1310.

[68] Tosun, M.; Chan, L.; Amani, M.; Roy, T.; Ahn, G. H.; Taheri, P.; Carraro, C.; Ager, J. W.; Maboudian, R.; Javey, A. Air-stable n-doping of WSe_2 by anion vacancy formation with mild plasma treatment. *ACS Nano* **2016**, *10*, 6853–6860.

[69] Kim, J.; Park, H.; Yoo, S.; Im, Y. H.; Kang, K.; Kim, J. Defect-engineered n-doping of WSe_2 via argon plasma treatment and its application in field-effect transistors. *Adv. Mater. Interfaces* **2021**, *8*, 2100718.

[70] Li, Y. B.; Wang, H. P.; Yang, X. L.; Zhang, W. Lateral homojunctions of WSe_2 through contact surface engineering with SF_6 plasma etching. *J. Mater. Chem. C* **2024**, *12*, 11474–11483.

[71] Kim, D. K.; Hong, S. B.; Jeong, K.; Lee, C.; Kim, H.; Cho, M. H. P-N junction diode using plasma boron-doped black phosphorus for high-performance photovoltaic devices. *ACS Nano* **2019**, *13*, 1683–1693.

[72] Jiang, J. F.; Zhang, Q. H.; Wang, A. Z.; Zhang, Y.; Meng, F. Q.; Zhang, C. C.; Feng, X. J.; Feng, Y. P.; Gu, L.; Liu, H. et al. A facile and effective method for patching sulfur vacancies of WS_2 via nitrogen plasma treatment. *Small* **2019**, *15*, 1901791.

[73] Rai, A. K.; Shah, A. A.; Kumar, J.; Chattaraj, S.; Dar, A. B.; Patbhaje, U.; Shrivastava, M. MoS_2 field-effect transistor performance enhancement by contact doping and defect passivation via fluorine ions and its cyclic field-assisted activation. *ACS Nano* **2024**, *18*, 6215–6228.

[74] Zhu, Y.; Wang, B. Y.; Deng, C. C.; Wang, Y. F.; Wang, X. F. Photothermal-pyroelectric-plasmonic coupling for high performance and tunable band-selective photodetector. *Nano Energy* **2021**, *83*, 105801.

[75] Shanmugam, V.; Mensah, R. A.; Babu, K.; Gawusu, S.; Chanda, A.; Tu, Y.; Neisiany, R. E.; Försth, M.; Sas, G.; Das, O. A review of the synthesis, properties, and applications of 2D materials. *Particle & Particle Systems Characterization* **2022**, *39*, 2200031.

[76] Shin, H.; Taqi, M.; Ali, F.; Lee, S.; Choi, M. S.; Kim, C.; Lee, B. H.; Liu, X. C.; Sun, J.; Oh, B. et al. Self-powered 2D $MoS_2/WO_x/WSe_2$ heterojunction photodetector realized by oxygen plasma treatment. *Adv. Mater. Interfaces* **2022**, *9*, 2201785.

[77] Hoffman, A. N.; Stanford, M. G.; Sales, M. G.; Zhang, C.; Ivanov, I. N.; McDonnell, S. J.; Mandrus, D. G.; Rack, P. D. Tuning the electrical properties of WSe_2 via O_2 plasma oxidation: Towards lateral homojunctions. *2D Mater.* **2019**, *6*, 045024.

[78] Wu, S. X.; Zeng, Y.; Zeng, X. B.; Wang, S. B.; Hu, Y. S.; Wang, W. Z.; Yin, S.; Zhou, G. T.; Jin, W.; Ren, T. T. et al. High-performance p-type MoS_2 field-effect transistor by toroidal-magnetic-field controlled oxygen plasma doping. *2D Mater.* **2019**, *6*, 025007.

[79] Lee, I.; Kang, M. G.; Park, S.; Park, C.; Lee, H.; Bae, S.; Lim, H.; Kim, S.; Hong, W.; Choi, S. Y. Healing donor defect states in CVD-grown MoS_2 field-effect transistors using oxygen plasma with a channel-protecting barrier. *Small* **2024**, *20*, 2305143.

[80] Rai, A. K.; Shah, A. A.; Dar, A. B.; Kumar, J.; Shrivastava, M. Reconfiguration of intrinsic depletion-mode characteristics of MoS_2 field-effect transistors to high-performance enhancement-mode operation using an argon plasma-induced p-type doping technique. *Small Methods* **2025**, *9*, 2401001.

[81] Lu, J.; Zhang, X.; Su, G.; Yang, W.; Han, K.; Yu, X.; Wan, Y.; Wang, X.; Yang, P. Large-area uniform few-layer PtS_2: Synthesis, structure and physical properties. *Mater. Today Phys.* **2021**, *18*, 100376.

[82] Lewis, S. M.; Hunt, M. S.; DeRose, G. A.; Alty, H. R.; Li, J.; Wertheim, A.; De Rose, L.; Timco, G. A.; Scherer, A.; Yeates, S. G. et al. Plasma-etched pattern transfer of sub-10 nm structures using a metal-organic resist and helium ion beam lithography. *Nano Lett.* **2019**, *19*, 6043–6048.

[83] Xiao, D. Z.; Ruan, Q. D.; Bao, D. L.; Luo, Y.; Huang, C.; Tang, S. Y.; Shen, J.; Cheng, C.; Chu, P. K. Effects of ion energy and density on the plasma etching-induced surface area, edge electrical field, and multivacancies in $MoSe_2$ nanosheets for enhancement of the hydrogen evolution reaction. *Small* **2020**, *16*, 2001470.

[84] Yang, R.; Zhang, L. C.; Wang, Y.; Shi, Z. W.; Shi, D. X.; Gao, H. J.; Wang, E. G.; Zhang, G. Y. An anisotropic etching effect in the graphene basal plane. *Adv. Mater.* **2010**, *22*, 4014–4019.

[85] Choi, K. R.; Woo, J. C.; Joo, Y. H.; Chun, Y. S.; Kim, C. I. Dry etching properties of TiO_2 thin films in $O_2/CF_4/Ar$ plasma. *Vacuum* **2013**, *92*, 85–89.

[86] Zhou, J.; Zhang, C. C.; Shi, L.; Chen, X. Q.; Kim, T. S.; Gyeon, M.; Chen, J.; Wang, J. L.; Yu, L. W.; Wang, X. R. et al. Non-invasive digital etching of van der Waals semiconductors. *Nat. Commun.* **2022**, *13*, 1844.

[87] Feng, X. W.; Huang, X.; Chen, L.; Tan, W. C.; Wang, L.; Ang, K. W. High mobility anisotropic black phosphorus nanoribbon field-effect transistor. *Adv. Funct. Mater.* **2018**, *28*, 1801524.
[88] Kim, C.; Kim, M.; Cho, D.; Kanade, C. K.; Seok, H.; Bak, M. S.; Kim, D.; Kang, W. S.; Kim, T.; Kim, H. U. First-principles calculation guided high-purity layer control of 4 in. MoS_2 by plasma RIE. *Chem. Mater.* **2023**, *35*, 1016–1028.
[89] Lee, G.; Lee, J. Y.; Lee, G. H.; Kim, J. Tuning the thickness of black phosphorus via ion bombardment-free plasma etching for device performance improvement. *J. Mater. Chem. C* **2016**, *4*, 6234–6239.
[90] Wei, D. C.; Peng, L.; Li, M. L.; Mao, H. Y.; Niu, T. C.; Han, C.; Chen, W.; Wee, A. T. S. Low temperature critical growth of high quality nitrogen doped graphene on dielectrics by plasma-enhanced chemical vapor deposition. *ACS Nano* **2015**, *9*, 164–171.
[91] Yi, K. Y.; Jin, Z. P.; Bu, S. Y.; Wang, D. G.; Liu, D. H.; Huang, Y. M.; Dong, Y. M.; Yuan, Q. H.; Liu, Y. Q.; Wee, A. T. S. et al. Catalyst-free growth of two-dimensional BC_xN materials on dielectrics by temperature-dependent plasma-enhanced chemical vapor deposition. *ACS Appl. Mater. Interfaces* **2020**, *12*, 33113–33120.
[92] Lin, T. Z.; Kang, B. T.; Jeon, M.; Huffman, C.; Jeon, J.; Lee, S.; Han, W.; Lee, J.; Lee, S.; Yeom, G. et al. Controlled layer-by-layer etching of MoS_2. *ACS Appl. Mater. Interfaces* **2015**, *7*, 15892–15897.
[93] Shuck, C. E.; Xiao, X.; Wang, Z. Y. Challenges and opportunities in 2D materials. *Accounts of Chemical Research* **2024**, *57*, 3079–3080.
[94] Tian, S. J.; Chen, W. H.; Wang, R. X.; Qin, C.; Jiang, Z. J.; Jiang, Z. Q. Ar/NH_3 radio-frequency plasma etching and n-doping to stabilize metallic phase 1T-MoS_2 for fast and durable sodium-ion storage. *Adv. Funct. Mater.* **2024**, *34*, 2408035.
[95] Marinov, D.; de Marneffe, J. F.; Smets, Q.; Arutchelvan, G.; Bal, K. M.; Voronina, E.; Rakhimova, T.; Mankelevich, Y.; El Kazzi, S.; Nalin Mehta, A. et al. Reactive plasma cleaning and restoration of transition metal dichalcogenide monolayers. *npj 2D Mater. Appl.* **2021**, *5*, 17.
[96] Wyndaele, P. J.; de Marneffe, J. F.; Sergeant, S.; de la Rosa, C. J. L.; Brems, S.; Caro, A. M.; De Gendt, S. Enhancing dielectric passivation on monolayer WS_2 via a sacrificial graphene oxide seeding layer. *npj 2D Mater. Appl.* **2024**, *8*, 25.
[97] Sun, H. B.; Dong, J. C.; Liu, F. N.; Ding, F. Etching of two-dimensional materials. *Materials Today* **2021**, *42*, 192–213.
[98] You, Y.; Park, J.; Kim, J. Editors' choice-atomic layer etching of tungsten disulfide using remote plasma-induced oxidation and wet etching. *ECS J. Solid State Sci. Technol.* **2023**, *12*, 075009.
[99] Jia, J. Y.; Jang, S. K.; Lai, S.; Xu, J.; Choi, Y. J.; Park, J. H.; Lee, S. Plasma-treated thickness-controlled two-dimensional black phosphorus and its electronic transport properties. *ACS Nano* **2015**, *9*, 8729–8736.
[100] Wang, Z.; Xia, H.; Wang, P.; Zhou, X. H.; Liu, C. S.; Zhang, Q. H.; Wang, F.; Huang, M. L.; Chen, S. Y.; Wu, P. S. et al. Controllable doping in 2D layered materials. *Adv. Mater.* **2021**, *33*, 2104942.
[101] Zhang, Y. G.; Liu, Q.; Zhang, D. L.; Hong, Y.; Li, Q. Anisotropic etching of 2D layered materials. *ChemPhysMater* **2024**, *3*, 341–356.
[102] Hug, D.; Zihlmann, S.; Rehmann, M. K.; Kalyoncu, Y. B.; Camenzind, T. N.; Marot, L.; Watanabe, K.; Taniguchi, T.; Zumbühl, D. M. Anisotropic etching of graphite and graphene in a remote hydrogen plasma. *npj 2D Mater. Appl.* **2017**, *1*, 21.
[103] Danielsen, D. R.; Lyksborg-Andersen, A.; Nielsen, K. E. S.; Jessen, B. S.; Booth, T. J.; Doan, M.-H.; Zhou, Y.; Bøggild, P.; Gammelgaard, L. Super-resolution nanolithography of two-dimensional materials by anisotropic etching. *ACS Applied Materials & Interfaces* **2021**, *13*, 41886–41894.
[104] Efremov, A.; Lee, J.; Kim, J. On the control of plasma parameters and active species kinetics in $CF_4 + O_2 + Ar$ gas mixture by CF_4/O_2 and O_2/ar mixing ratios. *Plasma Chem. Plasma Process.* **2017**, *37*, 1445–1462.
[105] Liu, H.; Wang, C.; Zuo, Z. G.; Liu, D. M.; Luo, J. B. Direct visualization of exciton transport in defective few-layer WS_2 by ultrafast microscopy. *Adv. Mater.* **2020**, *32*, 1906540.
[106] Tao, Y. J.; Tian, R.; Zhou, J. Y.; Chu, K.; Chen, X. G.; Gao, W. S.; Wang, G. P.; Jiang, Y. X.; Watanabe, K.; Taniguchi, T. et al. Optically active defect engineering via plasma treatment in a MIS-type 2D heterostructure. *Adv. Mater. Interfaces* **2024**, *11*, 2400288.
[107] Huang, Y. S.; Liu, Y. T.; Perng, T. P.; Lu, M. Y.; Chueh, Y. L.; Chen, L. J. Enhancing photocatalytic properties of continuous few-layer MoS_2 thin films for hydrogen production by water splitting through defect engineering with Ar plasma treatment. *Nano Energy* **2023**, *109*, 108295.
[108] Zheng, J. G.; Zhang, H.; Lv, J. B.; Zhang, M.; Wan, J. Y.; Gerrits, N.; Wu, A. J.; Lan, B. R.; Wang, W. T.; Wang, S. Y. et al. Enhanced NH_3 synthesis from air in a plasma tandem-electrocatalysis system using plasma-engraved n-doped defective MoS_2. *JACS Au* **2023**, *3*, 1328–1336.
[109] Zhou, W.; Zou, X. L.; Najmaei, S.; Liu, Z.; Shi, Y. M.; Kong, J.; Lou, J.; Ajayan, P. M.; Yakobson, B. I.; Idrobo, J. C. Intrinsic structural defects in monolayer molybdenum disulfide. *Nano Lett.* **2013**, *13*, 2615–2622.
[110] Jo, J.; Kim, J. H.; Kim, C. H.; Lee, J.; Choe, D.; Oh, I.; Lee, S.; Lee, Z.; Jin, H.; Yoo, J. W. Defect-gradient-induced Rashba effect in van der Waals $PtSe_2$ layers. *Nat. Commun.* **2022**, *13*, 2759.
[111] Liu, Y. S.; Liu, H.; Wang, J. C.; Liu, D. M. Defect-type-dependent carrier lifetimes in monolayer WS_2 films. *J. Phys. Chem. C* **2022**, *126*, 4929–4938.
[112] Lee, J. Y.; Kim, J. H.; Jung, Y.; Shin, J. C.; Lee, Y.; Kim, K.; Kim, N.; van der Zande, A. M.; Son, J.; Lee, G. H. Evolution of defect formation during atomically precise desulfurization of monolayer MoS_2. *Commun. Mater.* **2021**, *2*, 80.
[113] Li, Z.; Liu, L.; Xu, J. P. Largely enhanced mobility of MoS_2 field-effect transistors by optimizing O_2-plasma treatment on MoS_2. *IEEE Trans. Electron Devices* **2021**, *68*, 4614–4617.
[114] An, J. R.; Zhao, X. Y.; Zhang, Y. N.; Liu, M. X.; Yuan, J.; Sun, X. J.; Zhang, Z. Y.; Wang, B.; Li, S. J.; Li, D. B. Perspectives of 2D materials for optoelectronic integration. *Advanced Functional Materials* **2022**, *32*, 2110119.
[115] Islam, M. A.; Serles, P.; Kumral, B.; Demingos, P. G.; Qureshi, T.; Meiyazhagan, A.; Puthirath, A. B.; Abdullah, M. S. B.; Faysal, S. R.; Ajayan, P. M. et al. Exfoliation mechanisms of 2D materials and their applications. *Applied Physics Reviews* **2022**, *9*, 041301.
[116] Ping, X. F.; Liang, D.; Wu, Y. Y.; Yan, X. X.; Zhou, S. X.; Hu, D. K.; Pan, X. Q.; Lu, P. F.; Jiao, L. Y. Activating a two-dimensional $PtSe_2$ basal plane for the hydrogen evolution reaction through the simultaneous generation of atomic vacancies and Pt clusters. *Nano Lett.* **2021**, *21*, 3857–3863.
[117] Park, J.; Cho, I.; Jeon, H.; Lee, Y.; Zhang, J.; Lee, D.; Cho, M. K.; Preston, D. J.; Shong, B.; Kim, I. S. et al. Conversion of layered WS_2 crystals into mixed-domain electrochemical catalysts by plasma-assisted surface reconstruction. *Adv. Mater.* **2024**, *36*, 2314031.
[118] Nguyen, A. D.; Nguyen, T. K.; Le, C. T.; Kim, S.; Ullah, F.; Lee, Y.; Lee, S.; Kim, K.; Lee, D.; Park, S. et al. Nitrogen-plasma-treated continuous monolayer MoS_2 for improving hydrogen evolution reaction. *ACS Omega* **2019**, *4*, 21509–21515.
[119] Li, S.; Zhou, S.; Wang, X. C.; Tang, P.; Pasta, M.; Warner, J. H. Increasing the electrochemical activity of basal plane sites in porous 3D edge rich MoS_2 thin films for the hydrogen evolution reaction. *Mater. Today Energy* **2019**, *13*, 134–144.
[120] Kim, K. H.; Kim, K. S.; Ji, Y. J.; Moon, I.; Heo, K.; Kang, D. H.; Kim, K. N.; Yoo, W. J.; Park, J. H.; Yeom, G. Y. Effect of large work function modulation of MoS_2 by controllable chlorine doping using a remote plasma. *J. Mater. Chem. C* **2020**, *8*, 1846–1851.
[121] Wu, Q. Q.; Li, L.; Wang, C. L.; Wang, Z. H.; Weng, Z. J.; Jiang, Y.

F.; Lin, L. L.; Gu, X. F.; Angel, E. C.; El Sachat, A. et al. 2D WSe_2/MoS_2 p-i-n vertical heterojunction photodetectors by selective plasma doping. *Adv. Opt. Mater.* **2025**, *13*, 2402378.

[122] Abdulrahman, A. F.; Barzinjy, A. A.; Hamad, S. M.; Almessiere, M. A. Impact of radio frequency plasma power on the structure, crystallinity, dislocation density, and the energy band gap of ZnO nanostructure. *ACS Omega* **2021**, *6*, 31605–31614.

[123] Liu, X. Y.; Zhu, J. Q.; Shan, Y. F.; Liu, C. L.; Pan, C. Y.; Zhang, T. N.; Liu, C. X.; Chen, T. Y.; Ling, J. W.; Duan, J. L. et al. An ultrasensitive and broad-spectrum MoS_2 photodetector with extrinsic response using surrounding homojunction. *Adv. Sci.* **2024**, *11*, 2408299.

[124] Shawkat, M. S.; Gil, J.; Han, S. S.; Ko, T. J.; Wang, M. J.; Dev, D.; Kwon, J.; Lee, G. H.; Oh, K. H.; Chung, H. S. et al. Thickness-independent semiconducting-to-metallic conversion in wafer-scale two-dimensional $PtSe_2$ layers by plasma-driven chalcogen defect engineering. *ACS Appl. Mater. Interfaces* **2020**, *12*, 14341–14351.

[125] Ji, E. J.; Yang, K.; Shin, J. C.; Kim, Y.; Park, J. W.; Kim, J.; Lee, G. H. Exciton-dominant photoluminescence of MoS_2 by a functionalized substrate. *Nanoscale* **2022**, *14*, 14106–14112.

[126] Kang, S.; Kim, Y. S.; Jeong, J. H.; Kwon, J.; Kim, J. H.; Jung, Y.; Kim, J. C.; Kim, B.; Bae, S. H.; Huang, P. Y. et al. Enhanced photoluminescence of multiple two-dimensional van der Waals heterostructures fabricated by layer-by-layer oxidation of MoS_2. *ACS Appl. Mater. Interfaces* **2021**, *13*, 1245–1252.

[127] Costa, R. G.; do Nascimento Barbosa, A.; da Costa, M. E. H. M.; Junior, F. L. F. Resonance Raman spectroscopy of MoS_2 monolayers treated with nitrogen plasma. *Vib. Spectrosc.* **2022**, *123*, 103454.

[128] do Nascimento Barbosa, A.; Mendoza, C. A. D.; Lei, Y.; Giarola, M.; Terrones, M.; Mariotto, G.; Junior, F. L. F. Photoluminescence quenching of CVD grown WS_2 monolayers treated with low-power Ar plasma. *Surf. Interfaces* **2022**, *33*, 102220.

[129] Wu, S. Y.; Pan, W.; Zhang, J. L.; Ma, C. L.; Shan, Y.; Liu, L. Z. Defect-engineering-enhanced electrical manipulation of anisotropic excitons in two-dimensional ReS_2. *Surf. Interfaces* **2021**, *27*, 101562.

[130] do Nascimento Barbosa, A.; Mendoza, C. A. D.; Figueroa, N. J. S.; Terrones, M.; Júnior, F. L. F. Luminescence enhancement and Raman characterization of defects in WS_2 monolayers treated with low-power N_2 plasma. *Appl. Surf. Sci.* **2021**, *535*, 147685.

[131] Dhall, R.; Seyler, K.; Li, Z.; Wickramaratne, D.; Neupane, M. R.; Chatzakis, I.; Kosmowska, E.; Lake, R. K.; Xu, X. D.; Cronin, S. B. Strong circularly polarized photoluminescence from multilayer MoS_2 through plasma driven direct-gap transition. *ACS Photonics* **2016**, *3*, 310–314.

[132] Dhall, R.; Neupane, M. R.; Wickramaratne, D.; Mecklenburg, M.; Li, Z.; Moore, C.; Lake, R. K.; Cronin, S. Direct bandgap transition in many-layer MoS_2 by plasma-induced layer decoupling. *Adv. Mater.* **2015**, *27*, 1573–1578.

[133] Chowdhury, T.; Paul, D.; Nechiyil, D.; M A, G.; Watanabe, K.; Taniguchi, T.; Kumar, G. V. P.; Rahman, A. Modulation of trion and exciton formation in monolayer WS_2 by dielectric and substrate engineering. *2D Mater.* **2021**, *8*, 045032.

[134] Qi, R. X.; Ding, Y.; Zhou, L. Y.; Wang, C. L.; Lin, L. L.; Cai, Z. Y.; Xiao, S. Q.; Gu, X. F.; Nan, H. Y. Influence of plasma-induced phase transition on contact resistance in $MoTe_2$ with varying thickness. *Mater. Sci. Semicond. Process.* **2024**, *169*, 107889.

[135] Xie, F.; Yang, M.; Song, Z. Y.; Duan, W. C.; Huang, X. J.; Chen, S. H.; Li, P. H.; Xiao, X. Y.; Liu, W. Q.; Xie, P. H. Highly sensitive electrochemical detection of Hg(II) promoted by oxygen vacancies of plasma-treated ZnO: XPS and DFT calculation analysis. *Electrochimica Acta* **2022**, *426*, 140757.

[136] Liu, X. C.; Qu, D. S.; Wang, L.; Huang, M.; Yuan, Y. H.; Chen, P.; Qu, Y. Y.; Sun, J.; Yoo, W. J. Charge density depinning in defective $MoTe_2$ transistor by oxygen intercalation. *Adv. Funct. Mater.* **2020**, *30*, 2004880.

[137] Pan, Y. C.; Liu, X. C.; Yang, J. Q.; Yoo, W. J.; Sun, J. Controlling carrier transport in vertical $MoTe_2/MoS_2$ van der Waals heterostructures. *ACS Appl. Mater. Interfaces* **2021**, *13*, 54294–54300.

[138] Jung, J. H.; Choi, W. Unusual n-type doping of monolayer WSe_2 by CF_4 plasma treatment. *Mater. Lett.* **2021**, *295*, 129865.

[139] Lin, Y. C.; Bersch, B. M.; Addou, R.; Xu, K.; Wang, Q. X.; Smyth, C. M.; Jariwala, B.; Walker II, R. C.; Fullerton-Shirey, S. K.; Kim, M. J. et al. Modification of the electronic transport in atomically thin WSe_2 by oxidation. *Adv. Mater. Interfaces* **2020**, *7*, 2000422.

[140] Pei, C. J.; Li, X. Y.; Fan, H. C.; Wang, J.; You, H.; Yang, P.; Wei, C.; Wang, S.; Shen, X. G.; Li, H. Morphological and spectroscopic characterizations of monolayer and few-layer MoS_2 and WSe_2 nanosheets under oxygen plasma treatment with different excitation power: Implications for modulating electronic properties. *ACS Appl. Nano Mater.* **2020**, *3*, 4218–4230.

[141] Esfandiari, M.; Kamaei, S.; Rajabali, M.; Mohajerzadeh, S. High-performance large-area WS_2-based transistors by a novel tin-oxide assisted liquid-phase exfoliation: Doping adjustment by plasma treatment. *2D Mater.* **2021**, *8*, 025013.

[142] Nan, H. Y.; Wu, Z. T.; Jiang, J.; Zafar, A.; You, Y. M.; Ni, Z. H. Improving the electrical performance of MoS_2 by mild oxygen plasma treatment. *J. Phys. D: Appl. Phys.* **2017**, *50*, 154001.

[143] Huang, B. J.; Tian, F.; Shen, Y. D.; Zheng, M. R.; Zhao, Y. S.; Wu, J.; Liu, Y.; Pennycook, S. J.; Thong, J. T. L. Selective engineering of chalcogen defects in MoS_2 by low-energy helium plasma. *ACS Appl. Mater. Interfaces* **2019**, *11*, 24404–24411.

[144] Cheng, J. B.; Wang, C. L.; Zou, X. M.; Liao, L. Recent advances in optoelectronic devices based on 2D materials and their heterostructures. *Advanced Optical Materials* **2019**, *7*, 1800441.

[145] Zhao, S. W.; Huang, J. Q.; Crépel, V.; Xiong, Z. R.; Wu, X. G.; Zhang, T. Y.; Wang, H. W.; Han, X. Y.; Li, Z. Y.; Xi, C. Y. et al. Fractional quantum Hall phases in high-mobility n-type molybdenum disulfide transistors. *Nat. Electron.* **2024**, *7*, 1117–1125.

[146] Jang, Y. J.; Paul, K. K.; Park, J. C.; Kim, M.; Tran, M. D.; Song, H. Y.; Yun, S. J.; Lee, H.; Enkhbat, T.; Kim, J. et al. Boosting internal quantum efficiency via ultrafast triplet transfer to 2H-$MoTe_2$ film. *Sci. Adv.* **2023**, *9*, eadg2324.

[147] Jaikissoon, M.; Köroğlu, Ç.; Yang, J. A.; Neilson, K.; Saraswat, K. C.; Pop, E. CMOS-compatible strain engineering for monolayer semiconductor transistors. *Nat. Electron.* **2024**, *7*, 885–891.

[148] Tian, J. P.; Wang, Q. Q.; Huang, X. D.; Tang, J.; Chu, Y. B.; Wang, S. P.; Shen, C.; Zhao, Y. C.; Li, N.; Liu, J. Y. et al. Scaling of MoS_2 transistors and inverters to sub-10 nm channel length with high performance. *Nano Lett.* **2023**, *23*, 2764–2770.

[149] Sousa, F. B.; Ferreira, B. A. L.; Chakraborty, S. K.; Carvalho, L. C.; Cadore, A. R.; Nayak, B.; Ray, P.; Alexandre, S. S.; Sahoo, P. K.; Nunes, R. W. et al. Enhanced light emission in $MoSe_2$-WSe_2 lateral heterostructures in the electron-hole plasma rregime. *The Journal of Physical Chemistry Letters* **2025**, *16*, 8227–8233.

[150] Zhang, Y. W.; Ma, K. K.; Zhao, C.; Hong, W.; Nie, C. J.; Qiu, Z. J.; Wang, S. An ultrafast WSe_2 photodiode based on a lateral p–i–n homojunction. *ACS Nano* **2021**, *15*, 4405–4415.

[151] Kuddus, A.; Yokoyama, K.; Fan, W. B.; Ueno, K.; Shirai, H. Carrier transport properties in few-layer $WS_{0.3}Se_{1.7}/(WO_x)WS_{0.3}Se_{1.7}$ lateral p^+–n junctions using a metal-oxide-semiconductor field-effect transistor (MOSFET) structure. *ACS Appl. Electron. Mater.* **2023**, *5*, 1546–1557.

[152] Jain, A.; Bharadwaj, P.; Heeg, S.; Parzefall, M.; Taniguchi, T.; Watanabe, K.; Novotny, L. Minimizing residues and strain in 2D materials transferred from PDMS. *Nanotechnology* **2018**, *29*, 265203.

[153] Rokni, H.; Lu, W. Direct measurements of interfacial adhesion in 2D materials and van der Waals heterostructures in ambient air. *Nat. Commun.* **2020**, *11*, 5607.

[154] Xia, M. G.; Hu, R. X.; Wang, M.; Liu, S. R.; He, S. D.; Cheng, Z. F. Effect of hydrogen and oxygen plasma on the photoelectronic current

and photo-response time of SnS_2 flakes. *J. Phys. D: Appl. Phys.* **2021**, *54*, 255102.

[155] Kwon, J.; Seol, M.; Yoo, J.; Ryu, H.; Ko, D. S.; Lee, M. H.; Lee, E. K.; Yoo, M. S.; Lee, G. H.; Shin, H. J. et al. 200-mm-wafer-scale integration of polycrystalline molybdenum disulfide transistors. *Nat. Electron.* **2024**, *7*, 356–364.

[156] Lee, H.; Kim, H.; Kim, K.; Jeong, K.; Leem, M.; Park, S.; Kang, J.; Yeom, G.; Kim, H. Three-dimensional surface treatment of MoS_2 using BCl_3 plasma-derived radicals. *ACS Appl. Mater. Interfaces* **2023**, *15*, 46513–46519.

[157] Zhu, J. Q.; Wang, Z. C.; Yu, H.; Li, N.; Zhang, J.; Meng, J. L.; Liao, M. Z.; Zhao, J.; Lu, X. B.; Du, L. J. et al. Argon plasma induced phase transition in monolayer MoS_2. *J. Am. Chem. Soc.* **2017**, *139*, 10216–10219.

[158] Oyedele, A. D.; Yang, S. Z.; Feng, T. L.; Haglund, A. V.; Gu, Y. Y.; Puretzky, A. A.; Briggs, D.; Rouleau, C. M.; Chisholm, M. F.; Unocic, R. R. et al. Defect-mediated phase transformation in anisotropic two-dimensional $PdSe_2$ crystals for seamless electrical contacts. *J. Am. Chem. Soc.* **2019**, *141*, 8928–8936.

[159] Xiao, J. K.; Chen, K. L.; Zhang, X. K.; Liu, X. Z.; Yu, H. H.; Gao, L.; Hong, M. Y.; Gu, L.; Zhang, Z.; Zhang, Y. Approaching ohmic contacts for ideal monolayer MoS_2 transistors through sulfur-vacancy engineering. *Small Methods* **2023**, *7*, 2300611.

[160] Gao, T.; Feng, S.; Wang, X. Z.; Qin, T.; Gao, Y. P.; Liu, C.; Sun, D. M. MoS_2/MoO*x* heterojunction diode enabled via O_2 plasma oxidation for photon-controlled rectification and nonvolatile memory applications. *ACS Applied Electronic Materials* **2025**, *7*, 4999–5007.

[161] Li, Y. L.; Tian, Y. J.; Bao, L. J.; Cheng, H. R.; Cheng, Q. J. High responsivity and stability of MSM structured MoS_2 photodetectors by remote hydrogen plasma treatment and alternating growth of Al_2O_3/HfO_2 passivation layers. *J. Mater. Chem. A* **2024**, *12*, 18487–18497.

[162] Tang, B. S.; Yu, Z. G.; Huang, L.; Chai, J. W.; Wong, S. L.; Deng, J.; Yang, W. F.; Gong, H.; Wang, S. J.; Ang, K. W. et al. Direct n- to p-type channel conversion in monolayer/few-layer WS_2 field-effect transistors by atomic nitrogen treatment. *ACS Nano* **2018**, *12*, 2506–2513.

[163] Ngo, T. D.; Choi, M. S.; Lee, M.; Ali, F.; Hassan, Y.; Ali, N.; Liu, S.; Lee, C.; Hone, J.; Yoo, W. J. Selective electron beam patterning of oxygen-doped WSe_2 for seamless lateral junction transistors. *Adv. Sci.* **2022**, *9*, 2202465.

[164] Sun, J. C.; Lin, Z.; Jia, X. F.; Li, H. T.; Song, C.; Pan, F.; Fang, L.; Zhang, J. Y.; Wang, Y. Y. High-performance 2D WS_2 photodetector enhanced by charge-transfer doping through NH_3 annealing. *Mater. Today Phys.* **2023**, *35*, 101133.

[165] Oberoi, A.; Han, Y.; Stepanoff, S. P.; Pannone, A.; Sun, Y. Y.; Lin, Y. C.; Chen, C.; Shallenberger, J. R.; Zhou, D.; Terrones, M. et al. Toward high-performance p-type two-dimensional field effect transistors: Contact engineering, scaling, and doping. *ACS Nano* **2023**, *17*, 19709–19723.

[166] Chen, H. Y.; Wan, T. Q.; Zhou, Y.; Yan, J. M.; Chen, C. S.; Xu, Z. H.; Zhang, S. G.; Zhu, Y.; Yu, H. Y.; Chai, Y. Highly nonlinear memory selectors with ultrathin MoS_2/WSe_2/MoS_2 heterojunction. *Adv. Funct. Mater.* **2024**, *34*, 2304242.

[167] Jeong, U.; Rho, H. Y.; Oh, J. o.; Daw, D.; Lee, Y.; Chung, K.-B.; Sen, A.; Kim, S. Plasma-engineered high-performance tellurium field-effect phototransistors. *Advanced Functional Materials* **2025**, *35*, 2421140.

[168] Ghasemi, F.; Abdollahi, A.; Mohajerzadeh, S. Controlled plasma thinning of bulk MoS_2 flakes for photodetector fabrication. *ACS Omega* **2019**, *4*, 19693–19704.

[169] Nipane, A.; Choi, M. S.; Sebastian, P. J.; Yao, K. Y.; Borah, A.; Deshmukh, P.; Jung, Y.; Kim, B.; Rajendran, A.; Kwock, K. W. C. et al. Damage-free atomic layer etch of WSe_2: A platform for fabricating clean two-dimensional devices. *ACS Appl. Mater. Interfaces* **2021**, *13*, 1930–1942.

[170] Chen, B. W.; Yao, J. P.; Xia, J.; Yang, R.; Miao, X. S. A strain-sensitive flexible $MoTe_2$-based memristor for gesture recognition. *IEEE Electron Device Lett.* **2023**, *44*, 622–625.

[171] Yang, S.; Jiang, C.; Wei, S.-h. Gas sensing in 2D materials. *Applied Physics Reviews* **2017**, *4*, 021304.

[172] Choi, J.-H.; Ha, M.-J.; Kim, D. G.; Lee, J.-M.; Ahn, J.-H. Low-temperature growth of 2D-MoS_2 thin films by plasma-enhanced atomic layer deposition using a new molybdenum precursor and applicability to gas sensors. *ACS Applied Nano Materials* **2023**, *6*, 12132–12139.

[173] Mirzaei, A.; Kim, J.-Y.; Kim, H. W.; Kim, S. S. Resistive gas sensors based on 2D TMDs and MXenes. *Accounts of Chemical Research* **2024**, *57*, 2395–2413.

[174] Kumar, R.; Goel, N.; Jarwal, D. K.; Hu, Y.; Zhang, J.; Kumar, M. Strategic review on chemical vapor deposition technology-derived 2D material nanostructures for room-temperature gas sensors. *Journal of Materials Chemistry C* **2023**, *11*, 774–801.

[175] Chhowalla, M.; Shin, H. S.; Eda, G.; Li, L. J.; Loh, K. P.; Zhang, H. The chemistry of two-dimensional layered transition metal dichalcogenide nanosheets. *Nat. Chem.* **2013**, *5*, 263–275.

[176] Zhang, Y. J.; Jiang, Y. D.; Duan, Z. H.; Wu, Y. W.; Zhao, Q. N.; Liu, B. H.; Huang, Q.; Yuan, Z.; Li, X.; Tai, H. L. Edge-enriched MoS_2 nanosheets modified porous nanosheet-assembled hierarchical In_2O_3 microflowers for room temperature detection of NO_2 with ultrahigh sensitivity and selectivity. *J. Hazard. Mater.* **2022**, *434*, 128836.

[177] Zheng, W.; Liu, X. H.; Xie, J. Y.; Lu, G. C.; Zhang, J. Emerging van der Waals junctions based on TMDs materials for advanced gas sensors. *Coord. Chem. Rev.* **2021**, *447*, 214151.

[178] Wehling, T. O.; Novoselov, K. S.; Morozov, S. V.; Vdovin, E. E.; Katsnelson, M. I.; Geim, A. K.; Lichtenstein, A. I. Molecular doping of graphene. *Nano Lett.* **2008**, *8*, 173–177.

[179] Zhang, B.; Liu, Y. D.; Liang, T. T.; Sakthivel, T.; Yu, L. M.; Dai, Z. F. Activating the basal plane of defective SnS_2 nanosheets for NH_3 gas sensing. *ACS Appl. Nano Mater.* **2020**, *3*, 4642–4653.

[180] Wang, J. B.; Huang, J. J.; Huang, S. P.; Notohara, H.; Urita, K.; Moriguchi, I.; Wei, M. D. Rational design of hierarchical SnS_2 microspheres with S vacancy for enhanced sodium storage performance. *ACS Sustain. Chem. Eng.* **2020**, *8*, 9519–9525.

[181] Kumar, A.; Gutal, A. P.; Sharma, N.; Kumar, D.; Zhang, G.; Kim, H.; Kumar, P.; Paranjothy, M.; Kumar, M.; Strano, M. S. Investigations of vacancy-assisted selective detection of NO_2 molecules in vertically aligned SnS_2. *ACS Sens.* **2023**, *8*, 1357–1367.

[182] Sokolikova, M. S.; Mattevi, C. Direct synthesis of metastable phases of 2D transition metal dichalcogenides. *Chem. Soc. Rev.* **2020**, *49*, 3952–3980.

[183] Duan, Y.; Zhang, S.; Yu, Y. Y.; Qiu, J. J.; Feng, S. L. Facile microwave plasma driven 3D–WSe_2 2H–1T phase modulation for improving NO_2 gas sensing performance. *Sens. Actuators B: Chem.* **2023**, *387*, 133822.

[184] Park, C. H.; Koo, W. T.; Lee, Y. J.; Kim, Y. H.; Lee, J.; Jang, J. S.; Yun, H.; Kim, I. D.; Kim, B. J. Hydrogen sensors based on MoS_2 hollow architectures assembled by pickering emulsion. *ACS Nano* **2020**, *14*, 9652–9661.

[185] Lee, S.; Kang, Y.; Lee, J.; Kim, J.; Shin, J. W.; Sim, S.; Go, D.; Jo, E.; Kye, S.; Kim, J. et al. Atomic layer deposited Pt nanoparticles on functionalized MoS_2 as highly sensitive H_2 sensor. *Appl. Surf. Sci.* **2022**, *571*, 151256.

[186] Choi, S. Y.; Kim, Y.; Chung, H. S.; Kim, A. R.; Kwon, J. D.; Park, J.; Kim, Y. L.; Kwon, S. H.; Hahm, M. G.; Cho, B. Effect of Nb doping on chemical sensing performance of two-dimensional layered $MoSe_2$. *ACS Appl. Mater. Interfaces* **2017**, *9*, 3817–3823.

[187] Chee, S. S.; Lee, W. J.; Jo, Y. R.; Cho, M. K.; Chun, D.; Baik, H.; Kim, B. J.; Yoon, M. H.; Lee, K.; Ham, M. H. Atomic vacancy control and elemental substitution in a monolayer molybdenum

disulfide for high performance optoelectronic device arrays. *Adv. Funct. Mater.* **2020**, *30*, 1908147.

[188] Kuriakose, S.; Ahmed, T.; Balendhran, S.; Collis, G. E.; Bansal, V.; Aharonovich, I.; Sriram, S.; Bhaskaran, M.; Walia, S. Effects of plasma-treatment on the electrical and optoelectronic properties of layered black phosphorus. *Appl. Mater. Today* **2018**, *12*, 244–249.

[189] Yue, D. W.; Ju, X.; Hu, T.; Rong, X. M.; Liu, X. K.; Liu, X.; Ng, H. K.; Chi, D. Z.; Wang, X. Z.; Wu, J. Homogeneous in-plane WSe_2 P–N junctions for advanced optoelectronic devices. *Nanoscale* **2023**, *15*, 4940–4950.

[190] Peng, L. S.; Zheng, T.; Wu, Z. T.; Zheng, L.; Zhang, Y. High-performance ultrafast broadband photodetector based on van der Waals heterojunction through oxygen defect engineering. *J. Alloy. Compd.* **2025**, *1011*, 178338.

[191] Mitta, S. B.; Ali, F.; Yang, Z.; Moon, I.; Ahmed, F.; Yoo, T. J.; Lee, B. H.; Yoo, W. J. Gate-modulated ultrasensitive visible and near-infrared photodetection of oxygen plasma-treated WSe_2 lateral pn-homojunctions. *ACS Appl. Mater. Interfaces* **2020**, *12*, 23261–23271.

[192] Quan, S. F.; Li, L. Y.; Guo, S.; Zhao, X. Y.; Weller, D.; Wang, X. F.; Fu, S. Y.; Liu, R. B.; Hao, Y. F. SnS_2/MoS_2 van der Waals heterostructure photodetector with ultrahigh responsivity realized by a photogating effect. *ACS Appl. Mater. Interfaces* **2023**, *15*, 59592–59599.

[193] Zhang, J. W.; Liu, G. J.; Yuan, J. R.; Liao, X. X.; Zhou, Y. B. Enhanced photoresponse in $PdSe_2$ via local plasma treatment: Implication for advanced optoelectronic devices. *ACS Appl. Nano Mater.* **2025**, *8*, 3511–3518.

[194] Czerniak-Łosiewicz, K.; Świniarski, M.; Gertych, A. P.; Giza, M.; Maj, Z.; Rogala, M.; Kowalczyk, P. J.; Zdrojek, M. Unraveling the mechanism of the 150-fold photocurrent enhancement in plasma-treated 2D TMDs. *ACS Appl. Mater. Interfaces* **2022**, *14*, 33984–33992.

[195] Rho, H. Y.; Bala, A.; Sen, A.; Jeong, U.; Shim, J.; Oh, J. O.; Ju, Y.; Naqi, M.; Kim, S. Plasma-engineered amorphous metal oxide nanostructure-based low-power highly responsive phototransistor array for next-generation optoelectronics. *ACS Appl. Nano Mater.* **2023**, *6*, 15990–15999.

[196] Huang, Y. X.; Zhou, X. Y.; Luo, L. Z.; Zou, J. H.; Liu, H. Z.; Li, X.; Ren, A. B.; Shen, K.; Wu, J. High-performance broadband visible-near infrared photodetector enabled by atomic capping layer. *Adv. Opt. Mater.* **2022**, *10*, 2200539.

[197] Chen, S. C.; Mahmoodi, M. R.; Shi, Y. Y.; Mahata, C.; Yuan, B.; Liang, X. H.; Wen, C.; Hui, F.; Akinwande, D.; Strukov, D. B. et al. Wafer-scale integration of two-dimensional materials in high-density memristive crossbar arrays for artificial neural networks. *Nat. Electron.* **2020**, *3*, 638–645.

[198] Pan, C. B.; Ji, Y. F.; Xiao, N.; Hui, F.; Tang, K. C.; Guo, Y. Z.; Xie, X. M.; Puglisi, F. M.; Larcher, L.; Miranda, E. et al. Coexistence of grain-boundaries-assisted bipolar and threshold resistive switching in multilayer hexagonal boron nitride. *Adv. Funct. Mater.* **2017**, *27*, 1604811.

[199] Bala, A.; Sen, A.; Kim, Y. H.; Kim, Y. M.; Gandla, S.; Park, H.; Kim, S. Large-area MoS_2 nanosheets with triangular nanopore arrays as active and robust electrocatalysts for hydrogen evolution. *J. Phys. Chem. C* **2022**, *126*, 9696–9703.

[200] Liu, L.; Li, Y.; Huang, X. D.; Chen, J.; Yang, Z.; Xue, K. H.; Xu, M.; Chen, H. W.; Zhou, P.; Miao, X. S. Low-power memristive logic device enabled by controllable oxidation of 2D $HfSe_2$ for in-memory computing. *Adv. Sci.* **2021**, *8*, 2005038.

[201] Yin, S. Q.; Luo, Z. C.; Li, Q.; Xiong, C. Y.; Liu, Y. L.; Singh, R.; Zeng, F.; Zhong, Y.; Zhang, X. Z. Emulation of learning and memory behaviors by memristor based on Ag migration on 2D MoS_2 surface. *Phys. Status Solidi (a)* **2019**, *216*, 1900104.

[202] Wang, M.; Cai, S. H.; Pan, C.; Wang, C. Y.; Lian, X. J.; Zhuo, Y.; Xu, K.; Cao, T. J.; Pan, X. Q.; Wang, B. G. et al. Robust memristors based on layered two-dimensional materials. *Nat. Electron.* **2018**, *1*, 130–136.

[203] Varshney, K.; Shukla, P.; Prakash, B.; Das, D. M.; Rawat, B. Improved resistive switching and synaptic characteristics on 2–D graphene/MoS2/graphene memristor using O_2 plasma irradiation. In *Proceedings of 2024 8th IEEE Electron Devices Technology & Manufacturing Conference*, Bangalore, India, 2024, pp 1–3.

[204] Petzold, S.; Zintler, A.; Eilhardt, R.; Piros, E.; Kaiser, N.; Sharath, S. U.; Vogel, T.; Major, M.; McKenna, K. P.; Molina-Luna, L. et al. Forming-free grain boundary engineered hafnium oxide resistive random access memory devices. *Adv. Electron. Mater.* **2019**, *5*, 1900484.

[205] Wang, X. W.; Wang, B. L.; Zhang, Q. H.; Sun, Y. F.; Wang, E. Z.; Luo, H.; Wu, Y. H.; Gu, L.; Li, H. L.; Liu, K. Grain-boundary engineering of monolayer MoS_2 for energy-efficient lateral synaptic devices. *Adv. Mater.* **2021**, *33*, 2102435.

[206] Yadav, R.; Poudyal, S.; Rajarapu, R.; Biswal, B.; Barman, P. K.; Kasiviswanathan, S.; Novoselov, K. S.; Misra, A. Low power volatile and nonvolatile memristive devices from 1D MoO_2-MoS_2 core–shell heterostructures for future bio-inspired computing. *Small* **2024**, *20*, 2309163.

[207] Rajput, M.; Mallik, S. K.; Chatterjee, S.; Shukla, A.; Hwang, S.; Sahoo, S.; Kumar, G. V. P.; Rahman, A. Defect-engineered monolayer MoS_2 with enhanced memristive and synaptic functionality for neuromorphic computing. *Commun. Mater.* **2024**, *5*, 190.

[208] Peng, B.; Yu, G. N.; Zhao, Y. W.; Xu, Q.; Xing, G. C.; Liu, X. F.; Fu, D. Y.; Liu, B.; Tan, J. R. S.; Tang, W. et al. Achieving ultrafast hole transfer at the monolayer MoS_2 and $CH_3NH_3PbI_3$ perovskite interface by defect engineering. *ACS Nano* **2016**, *10*, 6383–6391.

[209] Le, K.; Zhang, X.; Zhao, Q.; Liu, Y. Z.; Yi, P.; Xu, S. S.; Liu, W. M. Controllably doping nitrogen into 1T/2H MoS_2 heterostructure nanosheets for enhanced supercapacitive and electrocatalytic performance by low-power N_2 plasma. *ACS Appl. Mater. Interfaces* **2021**, *13*, 44427–44439.

[210] Ngo, T. D.; Choi, M. S.; Lee, M.; Ali, F.; Yoo, W. J. Anomalously persistent p-type behavior of WSe_2 field-effect transistors by oxidized edge-induced Fermi-level pinning. *J. Mater. Chem. C* **2022**, *10*, 846–853.

[211] Pudasaini, P. R.; Oyedele, A.; Zhang, C.; Stanford, M. G.; Cross, N.; Wong, A. T.; Hoffman, A. N.; Xiao, K.; Duscher, G.; Mandrus, D. G. et al. High-performance multilayer WSe_2 field-effect transistors with carrier type control. *Nano Res.* **2018**, *11*, 722–730.

[212] Li, Z.; Yang, S. S.; Dhall, R.; Kosmowska, E.; Shi, H. T.; Chatzakis, I.; Cronin, S. B. Layer control of WSe_2 via selective surface layer oxidation. *ACS Nano* **2016**, *10*, 6836–6842.

[213] Liu, X. C.; Qu, D. S.; Yuan, Y. H.; Sun, J.; Yoo, W. J. Self-terminated surface monolayer oxidation induced robust degenerate doping in $MoTe_2$ for low contact resistance. *ACS Appl. Mater. Interfaces* **2020**, *12*, 26586–26592.

[214] Jadwiszczak, J.; O'Callaghan, C.; Zhou, Y. B.; Fox, D. S.; Weitz, E.; Keane, D.; Cullen, C. P.; O'Reilly, I.; Downing, C.; Shmeliov, A. et al. Oxide-mediated recovery of field-effect mobility in plasma-treated MoS_2. *Sci. Adv.* **2018**, *4*, eaao5031.

[215] Nipane, A.; Karmakar, D.; Kaushik, N.; Karande, S.; Lodha, S. Few-layer MoS_2 p-type devices enabled by selective doping using low energy phosphorus implantation. *ACS Nano* **2016**, *10*, 2128–2137.

This is an open access article under the terms of the Creative Commons Attribution 4.0 International License (CC BY 4.0, https://creativecommons.org/licenses/by/4.0/).

© The Author(s) 2025. Published by Tsinghua University Press.